ON THE CONTROL METHEDOLOGIES OF A NOVEL ACTIVE VIBRATION ISOLATOR

By

Gianmarc Coppola

A THESIS SUBMITTED IN PARTIAL FULFILLMENT OF THE REQUIREMENTS

FOR THE DEGREE OF

MASTER OF SCIENCE

IN

CONTROL ENGINEERING

FACULTY OF ENGINEERING

LAKEHEAD UNIVERSITY

THUNDER BAY, ONTARIO, CANADA, 2010

Your file Votre référence
ISBN: 978-0-494-71910-7
Our file Notre référence
ISBN: 978-0-494-71910-7

ABSTRACT

The work presented in this thesis is motivated by the need for new and effective methods to isolate vibrations in the rapidly growing technological sector, with particular interest in the control methodologies for active vibration isolation of a proposed isolator.

The thesis consists of four major parts. The first part (chapter 2) focuses on the development of dynamic mathematical models for the isolator. The nonlinear force and stiffness models are linearized and a dynamic experimental characterization is conducted to properly identify the system parameters. The characterization also serves as a model validation process.

The second part (chapter 3) investigates the ability of the active vibration isolator to perform with a phase compensation technique. This technique is realized by minimizing the 2^{nd} norm of the displacement transmissibility. An automatic on/off tuning algorithm is devised to take full advantage of both active and passive modes. Real-time experiments demonstrate the efficacy of the technique. The experimental results also show that with the proposed control scheme, the isolator is able to effectively suppress base excitations taking advantage of both active and passive modes.

The third part of the thesis involves investigating the notion of a delayed feedback control. A direct negative position feedback (NPF) and positive position feedback (PPF) stability analysis is conducted highlighting the effect of the inherent time lag in the system. Then a time delayed stability analysis is conducted to outline the bifurcations in the gain-delay plane. Subsequently, a design procedure is proposed to take advantage of the active damping for base isolation. The controllers developed are then tested in experiment comparing the performance of each. A notable finding for base isolation is that some degree of an inherent time delay present in hardware is beneficial when a relative direct positive position feedback is used.

The fourth part involves investigating the performance of a proposed adaptive nonlinear controller to function with the active isolator. The controller is tested in real time against a related controller which neglects the actuator physics. Several results are obtained and discussed in regard to the performance and parameter estimations. A performance increase and estimation accuracy increase is observed when using the proposed scheme.

Finally, it should be mentioned that though the study is based on a particular isolator, the findings are applicable to similar systems.

ACKNOWLEDGMENT

This thesis describes the majority of my research under the supervision of Dr. Kefu Liu, in the Department of Mechanical Engineering at Lakehead University, during 2008-2010.

Firstly, I would like to thank my supervisor Dr. Kefu Liu, to whom I own much gratitude and thanks for the superb guidance in the areas of both research and professional development. I am glad I will get the chance to continue research with him beyond this thesis.

Secondly, I would also like to thank Dr. Xiaoping Liu, my co-supervisor, for his kind and knowledgeable support, especially in the area of adaptive nonlinear control.

Thirdly, I would like to thank Mr. Kailash Bhatia for his great machining expertise. He was always the right person to go to when constructing the experimental systems. He is the kind of person that goes out of the way to assist others.

Fourthly, I would like to extend my thanks to Dr. A. Tayebi and Dr. M. Liu for their suggestions, particularly, Dr. M. Liu for her very thorough attention to detail. Their thoughts have helped me gain different perspectives onto my research.

Fifthly, I would like to thank my parents and brother for their support in my professional development over the years. They provide a backbone for my growth.

Lastly, I would like to thank Ofelia who deserves a special mention for having stood by me and for her professional support.

TABLE OF CONTENTS

LIST OF FIGURES

LIST OF TABLES

LIST OF ABBREVIATIONS, ACRONYMS AND MAIN SYMBOLS

EM	Electromagnet
PM	Permanent Magnet
RMS	Root-Mean-Square
SDOF	Single Degree of Freedom
TR	Displacement Transmissibility
ω_n	Natural Frequency
T	Natural period of vibration
ζ	Damping Ratio
c	Damping coefficient
D	Gap distance between the two steel cores
F_{pc}	Interaction force between the PM and the steel cores
F_{pf}	Interaction force between the PM and the flux generated by an energized EM
k	Linear stiffness
m	Mass
emf	Electromotive Force
L	EM Inductance
R	EM Resistance
k_v	Back emf proportional constant
i	Current in one EM loop
i_a	Total current in the actuator
e_c	Voltage applied to the actuator

x	Absolute displacement of the mass
z	Relative displacement of the mass
y	Base displacement
γ	Force proportional constant
FFT	Fast-Fourier-Transform
APF	Absolute Position Feedback
RPF	Relative position Feedback
NPF	Negative Position Feedback
PPF	Positive Position Feedback
LHP	Left-Half-Plane
RHP	Right-Half-Plane
K_P	Proportional gain
$\hat{K}_P$	Crossing gain
τ	Time delay
T_a	Time constant of the actuator
T_n	Normalized time constant of the actuator
ISR	Integral of the Squared Response
ISCC	Integral of the Squared Control Current
R_R	Unknown residual term
$\hat{\Theta}$	Parameter estimate vector

CHAPTER 1 - INTRODUCTION

Vibration is a physical phenomenon that occurs in nature. It is also referred to as a subset of dynamics that deals with repetitive motion [1]. In some cases vibration is a wanted occurrence as it is in music, vibration conveyors or ultrasonic vibrations. However, in the majority of cases it is detrimental and undesirable. It can cause uncomfortable environments or failure of equipment. There exist many examples of the catastrophic effects of unwanted or unaccounted for vibration. One example is the collapse of the Tacoma Narrows bridge in 1940 due to wind induced vibrations. Such potential failures provide sufficient motive in finding ways to alleviate the unwanted effects.

Researchers have been investigating various methods to eliminate or reduce structural vibrations for many decades. These structural vibrations occur in many different physical systems in a wide range of industries. Vibration isolation is the process of isolating an object from a source of vibration. In general, there are two broad classes in which isolation of vibration is necessary [2]. The first class deals with isolating vibrations that propagate from the main structure onto the supporting structure (Figure 1.1 (a)). The second class is concerned with the isolation of a structure from a vibrating base (Figure 1.1 (b)). This second case is referred to as base isolation and is the focus of this thesis. Needs for base isolation cover a wide spectrum ranging from earthquake engineering structures to precision instruments.

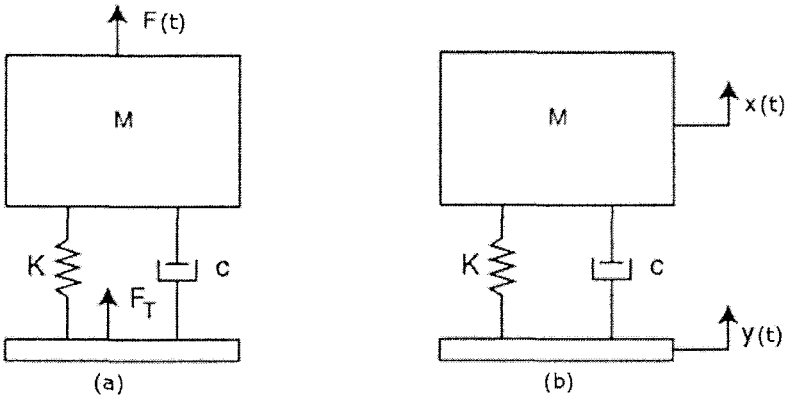

$F(t) = F_0 \sin\omega t$	$y(t) = Y\sin\omega_b t$
$\frac{F_T}{F_0} = \left[\frac{1+(2\zeta r)^2}{(1-r^2)^2+(2\zeta r)^2}\right]^{1/2}$	$\frac{X}{Y} = \left[\frac{1+(2\zeta r)^2}{(1-r^2)^2+(2\zeta r)^2}\right]^{1/2}$

Figure 1.1. Single Degree of Freedom (SDOF) Vibration Isolation Model

Figure 1.1 shows the most fundamental models for vibration isolation. The base and the main mass, M, are assumed rigid. The isolator, which consists of a viscous damper with damping coefficient, c, and a spring with stiffness, k, is assumed massless. The frequency ratio, r, is defined as the ratio of excitation frequency, ω_b, to the systems natural frequency, ω_n, and the damping ratio, ζ, is defined as $\zeta = c/(2m\omega_n)$. If the isolator is subjected to steady-state sinusoidal vibrations, its performance is usually measured in terms of the transmissibility ratio. If the vibration isolation problem is of the first class, the transmissibility ratio is the force transmissibility ratio defined as the ratio of the magnitude of exciting force to the magnitude of the force transmitted through the spring and dashpot to the fixed base ($TR = F_T / F_0$). On the other hand, if the vibration isolation problem is of the second class, namely base isolation, then this transmissibility ratio is the displacement transmissibility ratio defined as the ratio of the maximum response magnitude to the input displacement magnitude ($TR = X / Y$). These two magnitude ratios are equivalent if the system is linear and uniaxial [3].

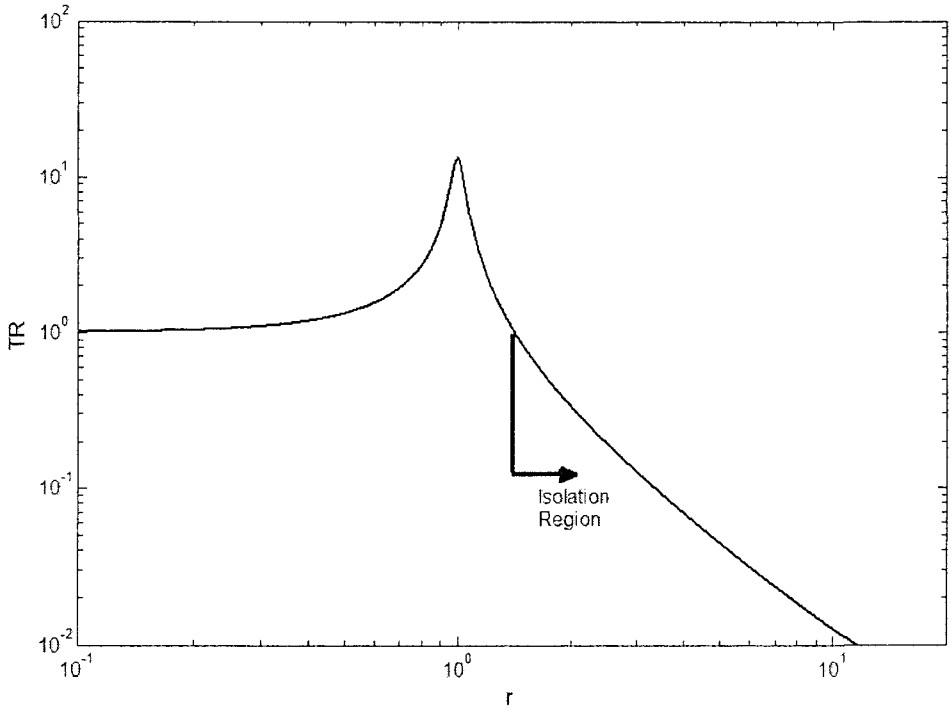

Figure 1.2. Transmissibility of the SDOF isolator

The means to isolate vibration mainly includes passive, semi-active or active control. Even though the passive SDOF model is relatively simple, a wealth of fundamental information about vibration isolation can be obtained from it. Passive isolators are essentially composed of stiffness and damping (as in Figure 1.1 (a) and (b)) which can be designed to achieve a certain performance. The stiffness of the system is usually used to determine the natural frequency, ω_n, which is where the system will exhibit the largest transmissibility ratio. The region where the isolator starts isolating vibrations is defined as the isolation region as observed in Figure 1.2. This occurs at an excitation frequency of $\sqrt{2}\omega_n$ and greater. Both stiffness and damping affect this region.

In practice, passive methodologies that are used to isolate of any vibration-sensitive equipment from base excitation are usually achieved using resilient mounts. However, conventional passive mounts suffer from an inherent trade-off between poor high-frequency isolation and amplification of vibration at the resonance frequency. An ideal passive mount should incorporate a high static stiffness to better support a larger load, and a low dynamic stiffness to provide better isolation. This is known as a high-static-low-dynamic stiffness (HSLDS) isolator, which is capable of supporting a large load while possessing a low natural frequency [4-7]. A semi-active isolator can alter its stiffness or damping or both through a closed-loop system in order to adapt to varying conditions [8-12]. Finally, active vibration isolators act by equipping the system with an actuator and a feedback control system to impose a controlled force on the structure. With proper design and control strategy, an active vibration isolator can deliver superior performance [13-20]. Due to the known inherent downfalls of traditional isolation methods, and the fact that active control methods can be applied to vibration isolation devices to improve the performance of the isolation system, the focus in this thesis is active vibration isolation. With the ever growing fast paced new technological market such as nanotechnology, the need for effective vibration isolation has never been greater and it will continue to become greater. As a consequence, scientists and engineers must continuously improve vibration isolation methods of the sensitive equipment used in these applications. The primary method of improvement of these technologies involves investigating new active isolation methods and their characteristics.

1.1. Objectives

The principal objective of the research in this thesis is to investigate different active vibration isolation methods with validation studies on a proposed active isolator. More specifically, the objectives of this thesis can be itemized as follows.

(1) To determine the dynamic characteristics of the proposed active isolator and develop a mathematical model through theory and experiment.
(2) To investigate the performance of the active isolator to with a phase compensation technique.
(3) To investigate the effect of inherent time delays within the isolator to various feedbacks.
(4) To explore purposefully injected time delays into the active control algorithm and determine the performance character over a wide frequency band. Also, determine stability perturbations due to this time delay.
(5) To examine the effect of uncertain parameters and/or parameter variations of the nonlinear model. Furthermore, the effect of the inclusion of actuator physics on the performance is explored.

1.2. Brief Outline of the Thesis

This thesis is structured in the following manner.

In chapter 2 the modeling and system identification is conducted in order to characterize the proposed isolator dynamically.

In chapter 3 the phase compensation technique is investigated. The optimal transmissibility is sought out and in experiment an automatic on/off switching technique is implemented experimentally.

Chapter 4 deals with the delayed feedback control technique. Stability perturbations due to purposefully injected delays are investigated and performance characteristics due to inherent delays are also determined.

In chapter 5 an adaptive nonlinear control scheme based on the backstepping technique is proposed for the active vibration isolator and its performance character is investigated in real time experiments.

Chapter 6 presents the conclusions of the thesis. Future work is also discussed.

CHAPTER 2 - MODELING AND SYSTEM CHARACTERIZATION

This chapter deals with the modeling and system characterization of a proposed active vibration isolator. The isolator is first presented with its dynamic modeling in section 2.1. The characterization by means of experiments is given in section 2.2.

2.1. Active Vibration Isolator and Dynamic Models

Figure 2.1 shows a schematic of the proposed active vibration isolator. A steel beam (1) is used to support a permanent magnet (PM) (2). The permanent magnet acts as an isolated mass and is referred to as mass m. The PM block is formed by two neodymium magnets enclosed in an aluminum casing. The block dimension is $l \times w \times h = 25.4 \times 25.4 \times 29.0$ mm. Its magnetization is 786.23 kAm^{-1}. The mass-beam assembly is placed between a pair of electromagnets (EMs) (3). The tension of the beam can be adjusted by screws (4). The beam supports and the EM supports are fastened to a base which rides on two linear guide carts sliding along a precision rail rack (6). The rail rack is fastened to a heavy rigid stand (7). A shaker (5) is used to excite the base through a stinger.

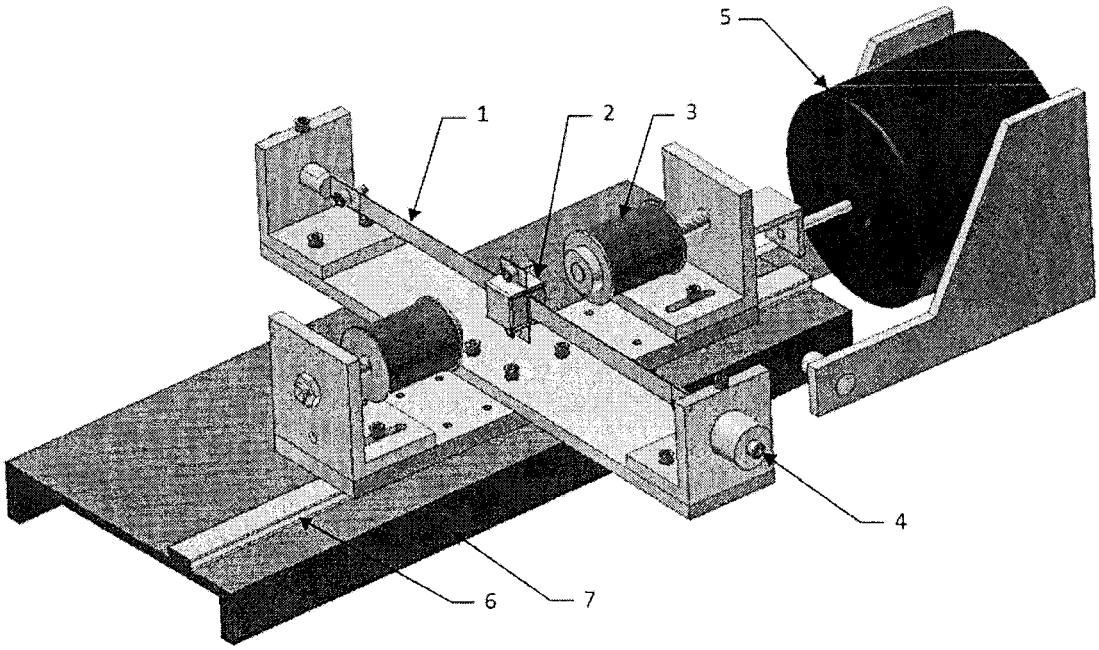

Figure 2.1. Schematic of the active vibration isolator.

Figure 2.2 illustrates a simplified model for the system and indicates the polarities of the PM and the EMs. Note that the polarities of the EMs vary according to the direction of the coil current. Any movement of the rigid stand is assumed negligible in modeling. Figure 2.2

also defines some key variables used to describe the model. The base motion is denoted by y while the motion of the mass is denoted by x. The stiffness of the beam is represented by k_b while the stiffness of the magnetic spring due to the interaction between the PM and the EM cores is represented by k_{pc}.

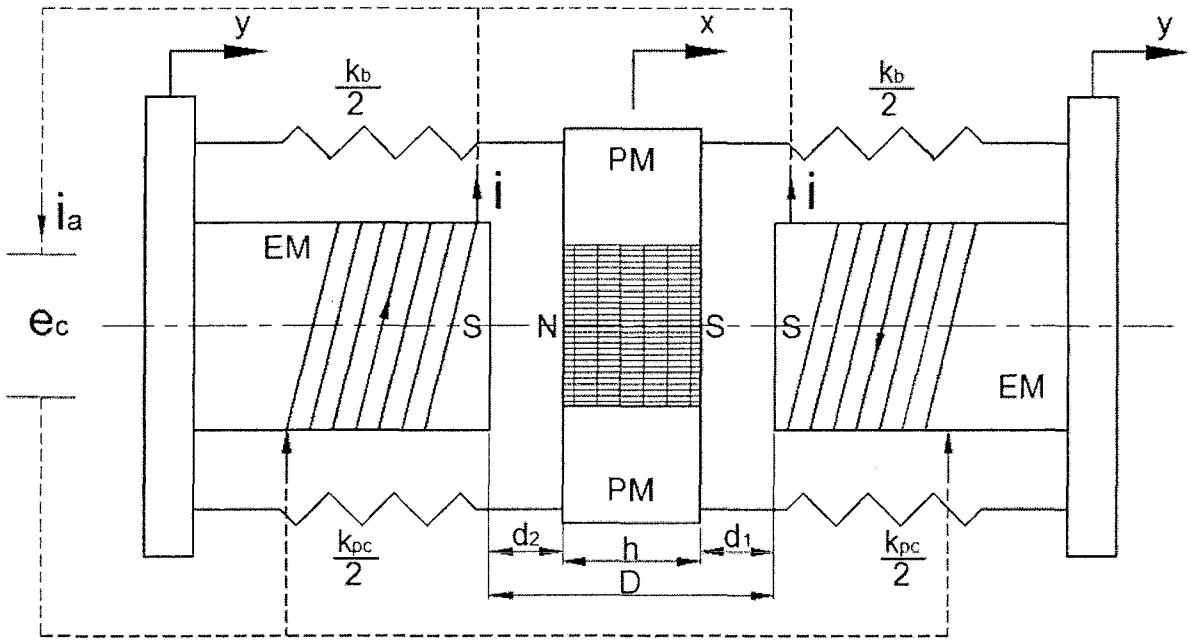

Figure 2.2. Illustrative model

The equation governing the motion of the mass is given by

$$m\ddot{z} + c\dot{z} + f_b + f_{pc} = -m\ddot{y} + F_c \tag{2.1}$$

where $z = x - y$ represents the relative displacement of the mass, f_b is the restoring force of the beam and f_{pc} is the attracting force of the magnetic spring, and F_c is the actuating force due to the interaction between the PM and the energized EMs. The study conducted in [21] has found that the restoring force f_b can be approximated by a cubic function,

$$f_b = k_1 z + k_3 z^3 . \tag{2.2}$$

In Appendix A, it is shown that the force due to the magnetic spring f_{pc} is given as

$$f_{pc} = -e^{-a_3|i|}\frac{8a_1q_1z(q_1^2+z^2)}{(q_1^2-z^2)^4} \tag{2.3}$$

and the actuating force is given as

$$F_c = sign(i)(1-e^{-b_3|i|})b_1\frac{2(q_2^4+6q_2^2z^2+z^4)}{(q_2^2-z^2)^4}. \tag{2.4}$$

If the relative displacement z and the current i are small in magnitude, equations (2.3) and (2.4) can be linearized such that

$$m\ddot{z} + c\dot{z} + (k_1 - k_{pc})z = -m\ddot{y} + \gamma i_a \tag{2.5}$$

where $k_{pc} = 8a_1/q_1^5$, $\gamma = b_1b_3/q_2^4$, and $i_a = 2i$ is the total current applied to the actuator.

As shown in Figure 2.2, the actuator is formed by connecting two identical EMs in parallel. Therefore, the dynamics of the actuator is defined by

$$\frac{L}{2}\dot{i}_a + \frac{R}{2}i_a + k_v\dot{z} = e_c \tag{2.6}$$

where L and R are the inductance and resistance of one EM, e_c is the voltage applied to the actuator, and the term $k_v\dot{z}$ represents the effect of back electromotive force (emf) induced by the motion of the mass with k_v as a proportional constant.

2.2. System Characterization

In order to control the system effectively, a thorough system characterization is needed. The characterization study serves a twofold purpose. While the primary purpose is to identify unknown dynamics/parameters and to verify modeling, the study intends to gain further insight to the limitations of the actual system and to identify any characteristics that are not included in the governing equations. In this study, an experimental approach was taken. The study employs two sets of electromagnetic actuators custom-made in lab. All the electromagnets were constructed by winding 22 Gauge copper wire around a low-carbon steel bolt with a diameter of 13.0 mm. For

the first set, the outer diameter and length of the coil are 46.6 mm and 88.0 mm, respectively, which results in about 3565 turns. For the second set, the outer diameter and length of the coil were both 55 mm, resulting in about 1213 turns. Hereinafter, the setup with the first set of the EMs will be referred to as Set one while the setup with the second set of the EMs will be referred to as Set two.

2.2.1 Actuator Inductance

As shown in Eq. (2.6), the actuator dynamics involves the resistance R, the inductance L, and the constant k_v. Among them, the resistance is the easiest to determine. Using a multimeter, it was found that the resistance for Set one is $R = 13\ \Omega$ and that for Set two is $R = 8.2\ \Omega$. For the determination of L and k_v, it is noted that there are many factors that can affect the inductance of a coil. These include temperature, current frequency and magnitude, etc. [22, 23]. Consequently, the correct inductance of an electromagnet should be determined in the domain of its use. Two methods were used for this purpose.

Step response method. Figure 2.3 is a depiction of a circuit that was used to determine the inductance of an electromagnet where L and R are the inductance and resistance of the coil, respectively and $R_s = 1\ \Omega$ is a resistor used to measure the current.

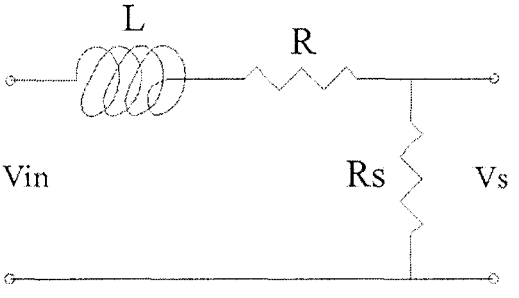

Figure 2.3. Circuit used to measure the EM inductance

When a voltage v_{in} is applied to the circuit, the governing equation of the circuit is of the form:

$$L\dot{i} + (R + R_s)i = v_{in}(t). \tag{2.7}$$

If a constant voltage V is suddenly applied, the current can be found to be

$$i(t) = \frac{V}{R + R_s}(1 - e^{-\frac{R+Rs}{L}t}). \tag{2.8}$$

With the knowledge of the resistance of the coil this equation can be used to estimate the inductance. An experiment was implemented as follows. The circuit was setup and a step voltage was applied to the amplifier (Quanser, UPM-2405) through the interface between dSpace ControlDesk and Matlab Simulink. The corresponding current draw was measured. Subsequently, equation (2.8) is used to estimate the inductance parameter. First, defining the time it takes for the current to reach exactly half of its final value starting at its initial value as $t_{1/2}$. Next, half of the final value of the current is given by $i_{1/2} = \frac{V}{2(R + R_s)}$. Using $t_{1/2}$ for t and $i_{1/2}$ for $i(t)$, equation (2.8) can be solved for the inductance L:

$$L = \frac{-(R + R_s)t_{1/2}}{\ln(1/2)}. \tag{2.9}$$

It is noted that, $t_{1/2}$ was measured from the collected data. An illustration of one of the step responses can be seen in Figure 2.4. The experiments were repeated three times for each setup. The average inductance values were found to be $L = 0.65$ H for Set one and $L = 0.16$ H for Set two.

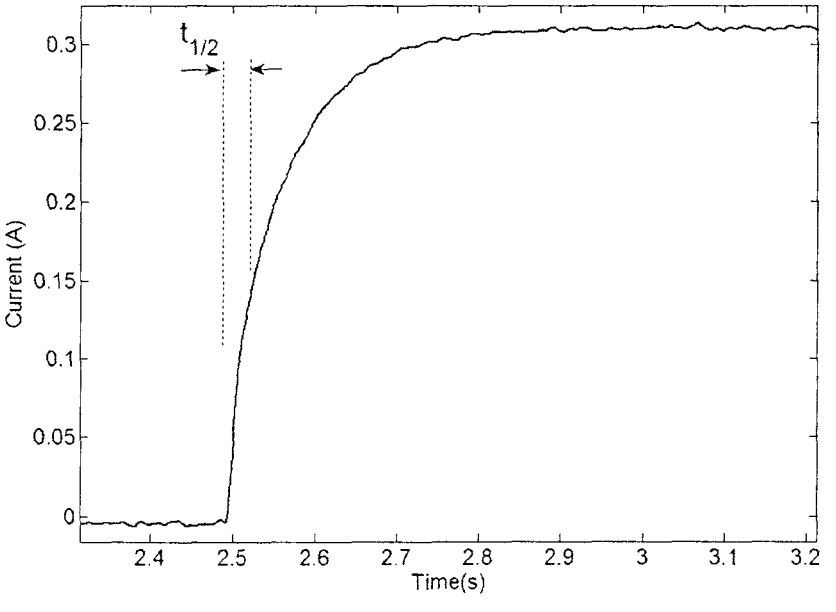

Figure 2.4. Step response of one EM for Set one

RLC Resonance. The second method involves the resonance of an RLC circuit where the inductance is unknown. The governing differential equation for an RLC circuit is given by

$$L\ddot{i} + R\dot{i} + \frac{1}{C}i = \dot{v}(t) \tag{2.10}$$

where C is capacitance. The natural frequency of the system is the frequency at which the system experiences resonance. This is given by

$$\omega_n = \sqrt{\frac{1}{LC}}\,. \tag{2.11}$$

Accordingly, experiments can be devised to locate the natural frequency of the circuit by subjecting it to sinusoidal voltages with varying frequencies. By measuring the magnitudes of the resulting currents, the relationship between the current magnitude and exciting frequency can be established. One example of such a relationship is given in Fig. 2.5 where the frequency corresponding to the peak value is taken as the natural frequency of the circuit. Once this frequency is determined equation, (2.11) is used to find the inductance given the value of capacitance used in the experiment. This method was condicted for two different sets of capacitors. The first had a capacitance value of 470 μF and the second 1000 μF. The experiments were repeated three times for each capacitance. The average inductance values were found to be $L = 0.610$ H for Set one and $L = 0.163$ H for Set two. These values are close to the results from the step response method. The results from method 1 are utilized in the study.

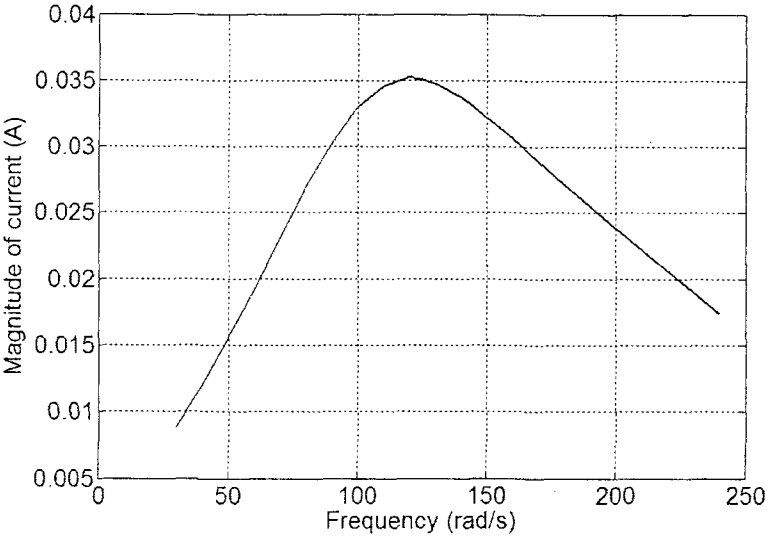

Figure 2.5. Frequency response of the RLC circuit consisting of the EM of Set two

2.2.2. Damping Coefficient and Proportional Constant for the Back emf Term

The system characterization also involved the identification of c and k_v. This is because, when the PM moves between the EMs, eddy currents are induced in the EMs. These eddy currents create magnetic fields in the EMs that oppose the original magnetic field, causing a repulsive force onto the PM, altering the damping coefficient c in equation (2.5). In the meantime, the PM motion also induces the back emf term $k_v\dot{z}$ in equation (2.6). The free response method was used to identify the damping coefficient c. For this purpose, the system was setup as shown in Fig. 2.1, an impact was applied to the PM and the free response was recorded. The recorded displacement, truncated at its first peak, can be considered a response induced by an initial displacement $z(0)$ given by

$$z(t) = \frac{z(0)}{\sqrt{1-\zeta^2}} e^{-\zeta\omega_n t} \sin\left(\omega_n\sqrt{1-\zeta^2}\,t + \tan\left(\frac{\sqrt{1-\zeta^2}}{\zeta}\right)\right) \tag{2.12}$$

where $\omega_n = \sqrt{k/m}$ is the undamped natural frequency and $\zeta = c/(2m\omega_n)$ is the damping ratio. Figure 2.6 shows typical responses of the PM, where the EMs are of Set two, and D the gap distance. By using $z(0)$ from the measured response and assigning trial values for ω_n and ζ, a response can be computed from equation (2.12). The root-mean-squared (RMS) error between

the experimental response and the computed response is found. A nonlinear optimization process was implemented to estimate the optimum values for ω_n and ζ such that the RMS error is minimized. The Sequential Simplex method was utilized for this process. Table 2.1 lists the best estimated values for the damping coefficients. It is noted that with a decrease in the gap distance, the added damping increases. Physically this makes sense as with a decrease in gap distance the magnetic flux density from the PM in larger creating more eddy currents.

Table 2.1. Estimated damping coefficients

D (mm)	c (kg/s), Set one	c (kg/s), Set two
100	0.28	0.31
90	0.62	0.48
80	0.77	0.63

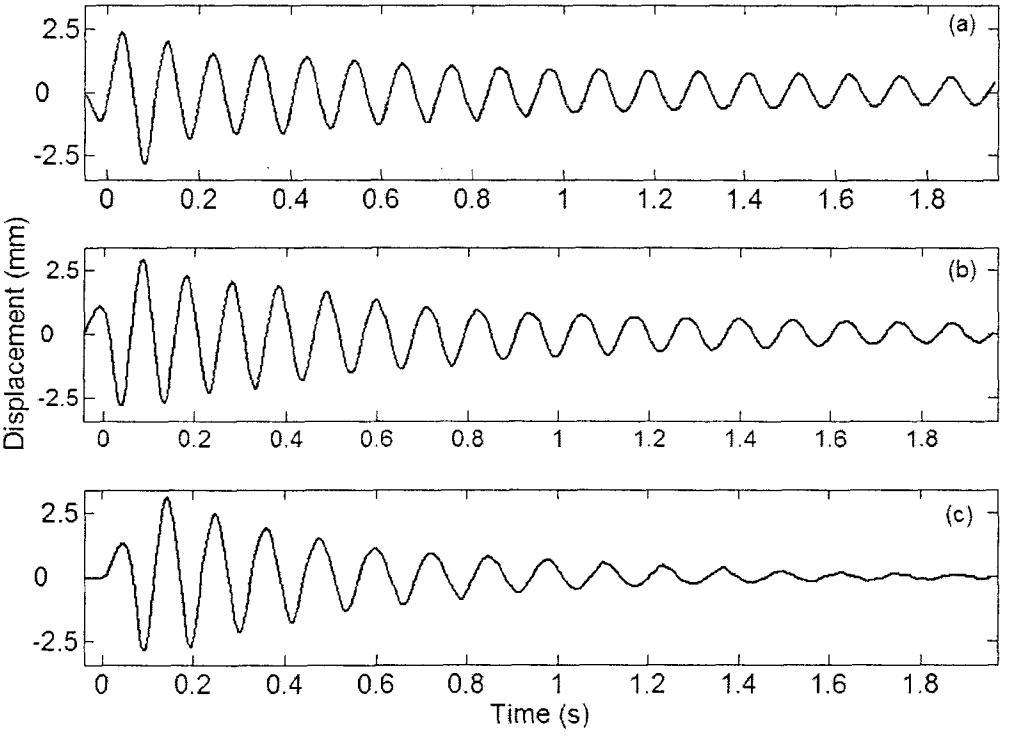

Figure 2.6. Typical responses of the PM, Set two, (a) D = 100 mm, (b) D = 90 mm, (c) D = 80 mm

Subsequently, the back emf proportional constant k_v was determined experimentally. The apparatus was setup as in Fig. 2.1 and the actuator circuit loop was closed. A sinusoidal excitation was generated to force the base of the apparatus into sinusoidal motion. The PM motion induced a current in the closed circuit. The current was measured directly. Figure 2.7 shows typical induced currents. From equation (2.6), the voltage due to back emf was found by

$$v_{emf} = 2k_v\dot{z} = -L\dot{i}_a - Ri_a. \tag{2.13}$$

With the measured amplitude Z of the PM displacement and the known frequency ω, the proportional constant k_v can be found by

$$k_v = \frac{v_{emf}}{2\omega Z}. \tag{2.14}$$

Table 2.2 lists the estimated values for k_v for both Set one and Set two with three different gap distances. It is noted that with a decrease in the gap distance, the back emf effect increases. This again is attributed to an increase in magnetic flux density with a decrease in gap distance.

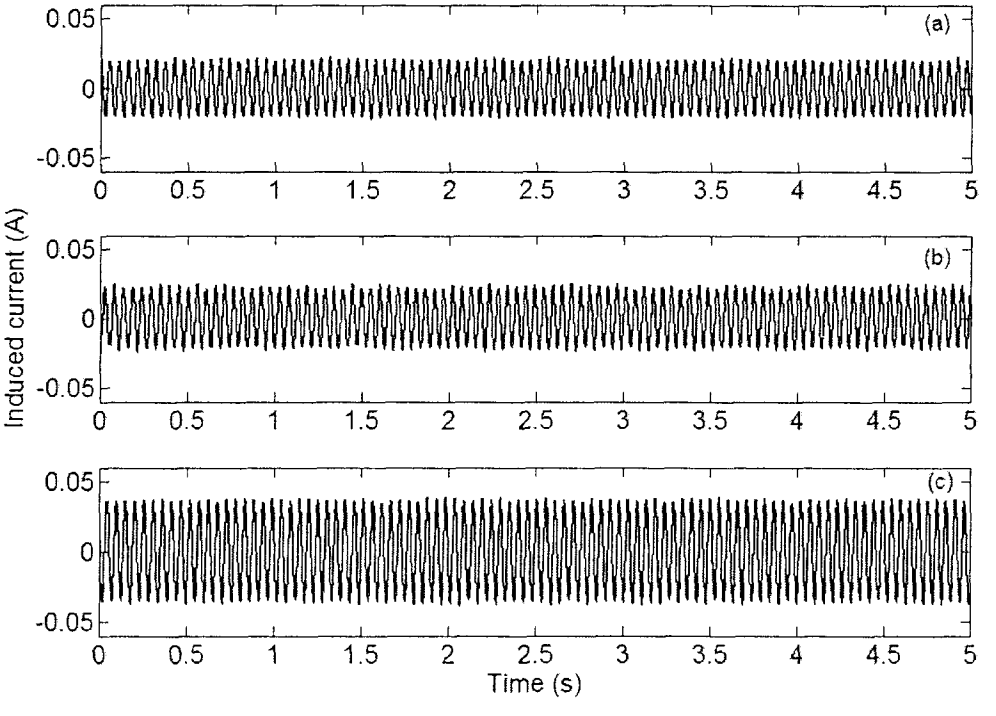

Figure 2.7. Induced currents, ω = 120 rad/s, Set two: (a) D = 100 mm, (b) D = 90 mm, (c) D = 80 mm

Table 2.2. Estimated constants for the back emf term

D (mm)	k_v (vs/m) (Set one)	k_v (vs/m) (Set two)
100	0.85	0.53
90	1.28	0.69
80	1.77	1.09

2.2.3 Dynamic Force Identification

The actuating force model derived in Appendix A was based on the interacting force between a PM and an EM from static experiments for which constant currents were used [21, 24]. It is expected that this model may not accurately represent an actuating force induced by alternating currents [25]. In order to gain a better understanding of the actuating force, a dynamic force identification was conducted. One method to obtain the dynamic force is via state measurement directly from experiment. Subsequently, the force produced can be estimated by directly using the states in the dynamic model. To reduce the nonlinearity effect, the nonlinear beam was replaced by a cantilever beam which remained mostly linear within the experimental setup. The governing equation of this setup is given by

$$m_b\ddot{z} + c_b\dot{z} + k_b z = F(t) \tag{2.15}$$

where $m_b = 0.14$ kg, $c_b = 0.572$ kg/s, and $k_b = 2800$ N/m are the mass, damping coefficient and stiffness respectively. With the apparatus base firmly fixed, a sinusoidal current $i(t) = I_0 \sin(\omega t)$ was applied to the actuator and the steady-state displacement of the mass was measured. Assuming that $F(t) = F_0 \sin(\omega t)$, the steady-state response of the mass is given by

$$\left(-\omega^2 m_b + j\omega c_b + k_b\right) Z(j\omega) = F(j\omega) \tag{2.16}$$

or

$$F_0 = \left|Z(j\omega)\right| m_b \sqrt{\left(\omega_n^2 - \omega^2\right)^2 + \left(2\omega\omega_n\zeta\right)^2} \tag{2.17}$$

where $\omega_n = \sqrt{k_b/m_b}$, $\zeta = c_b/(2m_b\omega_n)$ and $|Z(j\omega)|$ is the steady state displacement. From equation (2.17), the amplitude of the dynamic force , F_0 ,can be evaluated. Various experiments were conducted for which currents with various amplitudes and frequencies were applied and the steady-state responses of the mass were measured for each of the actuator sets.

Figures 2.8 and 2.9 show the dynamic force amplitudes generated by actuator Set one and actuator Set two, respectively. Three observations can be made. First, the proportionality of the force amplitude vs. the current amplitude exists only when the current amplitude is small. Second, the force amplitude is a function of the exciting frequency; the higher the exciting frequency, the smaller the force amplitude. And finally, for the same current amplitude, actuator Set one can generate greater force amplitude than actuator Set two.

According to the simplified force model, the actuating force is proportional to the current with the proportional constant given by $\gamma = b_1 b_3/q_2^4$ where $q_2 = (D-h)/2 + b_2$. The effect of the gap distance on the dynamic force amplitude was investigated as well. Figure 2.10 compares the dynamic force amplitudes for actuator Set one with three different gap distances. The results indicate that the greater the gap distance, the smaller the dynamic force amplitude. A similar trend was also observed using Set two.

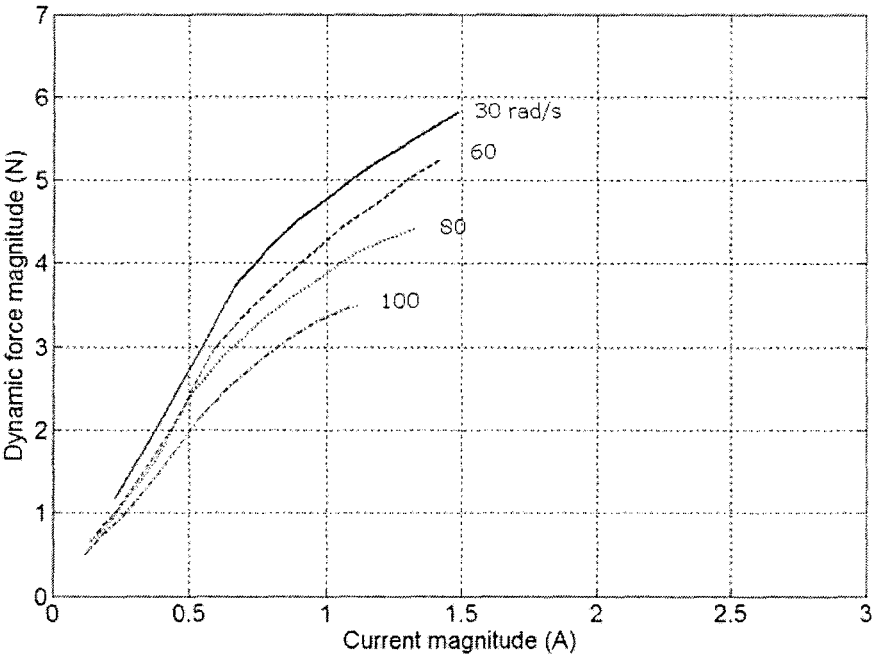

Figure 2.8. Dynamic force amplitudes for Set one for various frequencies, D = 100 mm, $\omega = 30$ rad/s (solid line), $\omega = 60$ rad/s (dashed line), $\omega = 80$ rad/s (dotted line), $\omega = 100$ rad/s (dash-dot line).

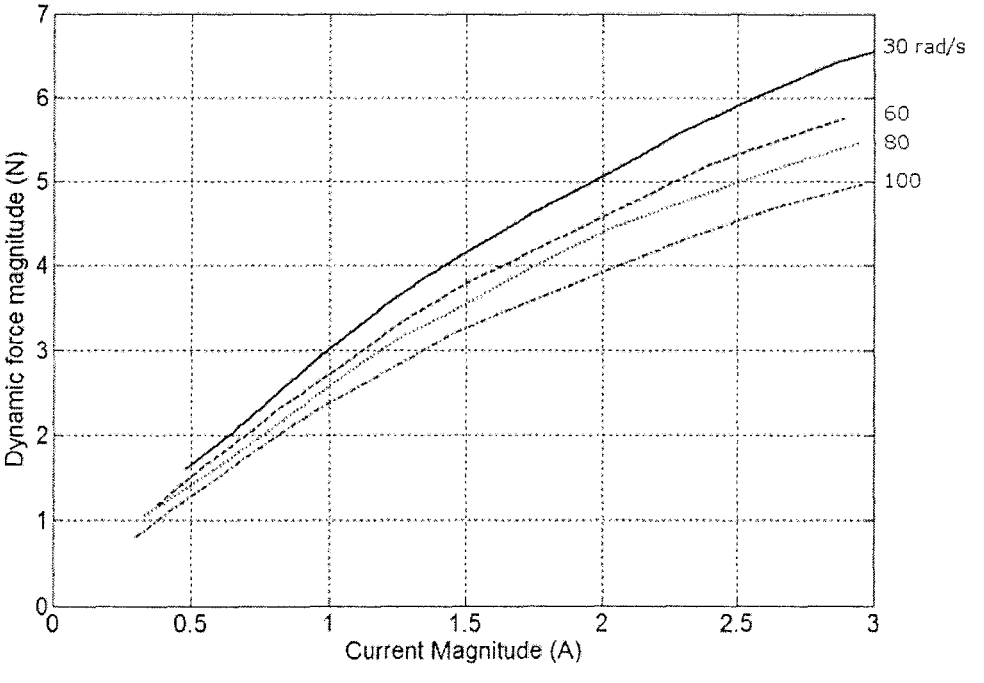

Figure 2.9. Dynamic force for Set two for various frequencies, D = 100 mm, $\omega = 30$ rad/s (solid line), $\omega = 60$ rad/s (dashed line), $\omega = 80$ rad/s (dotted line), $\omega = 100$ rad/s (dash-dot line).

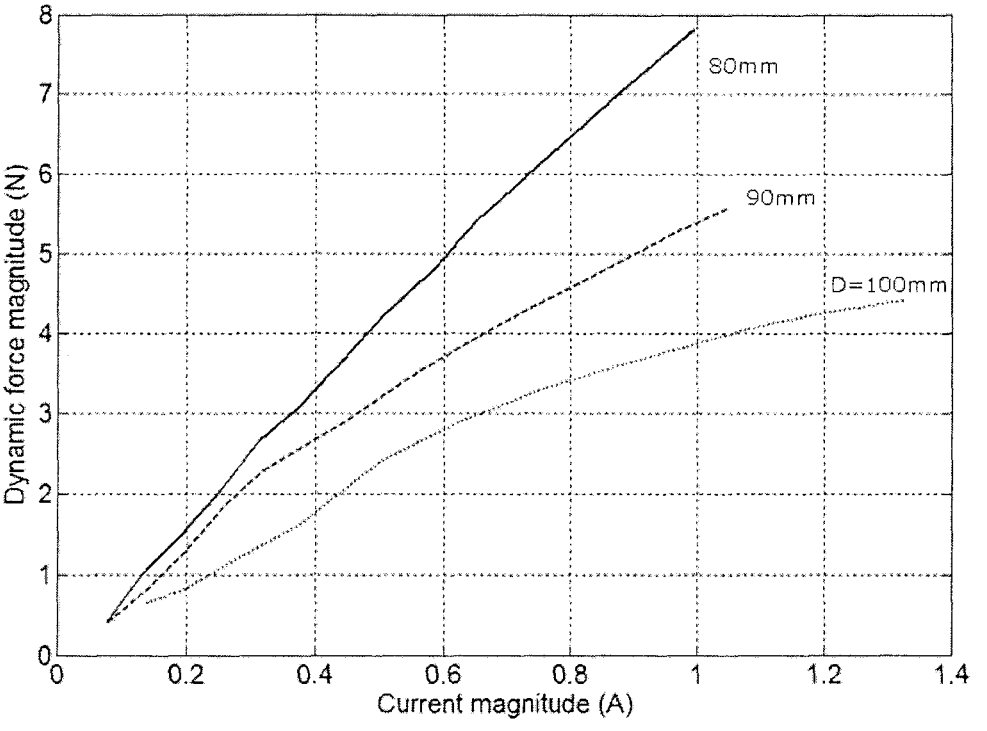

Figure 2.10. Dynamic force amplitudes, $\omega = 80$ rad/s, Set one: D = 100 mm (dotted line), D = 90 mm (dashed line), D = 80 mm (solid line).

CHAPTER 3 - PHASE COMPENSATION TECHNIQUE WITH AUTOMATIC ON/OFF SWITCHING

Now that the proposed active vibration isolator has been modeled and characterized, its performance with a phase compensation technique is investigated. Section 3.1 provides a review of related research. Section 3.2 outlines the stability and control design of the active vibration isolator with the phase compensation technique. Section 3.3 presents a real-time implementation of the controllers developed and discusses attained results. Subsequently, the conclusions for this chapter are drawn in section 3.4.

3.1. Introduction

The isolator modeled in chapter 2 was used for semi-active isolation in [21]. This chapter will further develop the system and demonstrates one possible method in which it can be realized as an active isolator [26, 27]. Toward this end, a stability study is conducted to show that a simple negative proportional feedback control is not acceptable. This is thought to be mainly due to the problem of inherent delays caused by the dynamics of the electromagnetic actuator. Three controller parameters are identified. An optimization problem is formulated to determine the optimum controller parameters by minimizing the 2^{nd} norm of the displacement transmissibility. Both a absolute position feedback and a relative position feedback are studied. In real time implementation, the best displacement transmissibility of the isolator is measured. An automatic on/off switching strategy is devised to take full advantage of both the active isolator and passive isolator. The experimental results show that with the proposed control scheme, the isolator is able to effectively suppress base excitations. It is noted that, compensating inherent lags have been the focus of much research. A few notable studies are [28-31]. A phase-lead compensation technique is utilized to improve the stability of the closed-loop system [32-35].

3.2. Stability Analysis and Control Design

The notion for the stability analysis arises from the knowledge that the system under consideration possesses some unique attributes that make active control challenging. Moreover, the main idea behind a linear stability analysis of such a system is that the dynamics of the nonlinear system near a hyperbolic equilibrium point can be determined from a linearization about that equilibrium point. For the stability analysis equations (2.5) and (2.6) are represented as

$$\begin{aligned} m\ddot{z} + c\dot{z} + kz &= \gamma\, i_a \\ L\dot{i}_a + Ri_a + 2k_v\dot{z} &= 2e_c \end{aligned} \tag{3.1}$$

with $k = k_1 - k_{pc}$.

It is important to note that all of the system parameters utilized in this model have come from the systematic characterization at D = 100 mm. Table 3.1 lists the parametric values used in the stability analysis which resulted from the previous sections characterization. It should be noted that a value of 1 ohm is to be added to the resistance values shown in Table 3.1. The 1 ohm resistance comes from the resistor connected in series with the actuator in order to collect current data.

Table 3.1. The parameter values used in the stability analysis

Mechanical system		
$m = 0.17$ **kg**	$k = 754$ **N/m**	$c = 0.283$ **kg/s**
Actuators		
	Set one	Set two
γ * **(N/A)**	4.23	2.46
L **(H)**	0.65	0.16
R **(Ω)**	13	8.2
k_v **(vs/m)**	0.85	0.53

* Values linearly interpolated to $\omega = \omega_n = 10.6$ Hz

A proportional feedback is considered. In practice, there are two permissible ways to introduce a proportional feedback: absolute position feedback (APF) and relative position feedback (RPF) [36]. Although the latter is not as common as the former, it can be used in conjunction with another control sequence [37]. For the APF, the control voltage applied to the actuator is given by $e_c = -K_p x$ whereas for the RPF, $e_c = -K_p z$ where K_p is the feedback gain. For both the APF and the RPF, the characteristic equation of the closed-loop system is given by

$$s^3 + \left(\frac{R}{L} + \frac{c}{m}\right)s^2 + \left(\frac{Rc}{mL} + \frac{k}{m} + \frac{2\gamma k_v}{mL}\right)s + \frac{kR}{mL} + \frac{2\gamma K_p}{mL} = 0 \tag{3.2}$$

where s is a complex number.

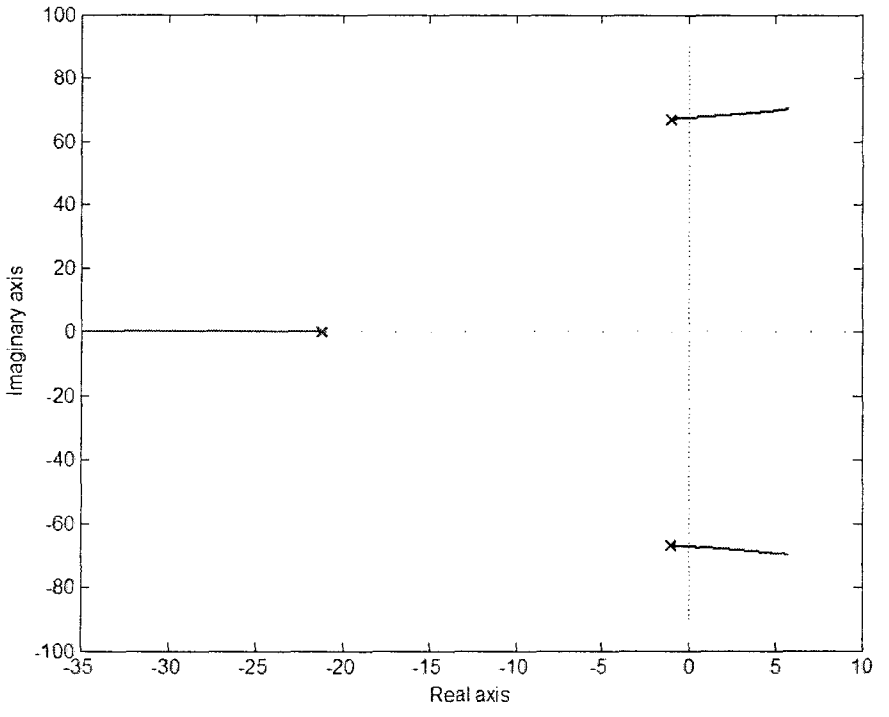

Figure 3.1. Root loci of the closed-loop system with the proportional control and actuator Set one

The root loci of equation (3.2), in conjunction with the values of Table 3.1 (Set one) can be seen in Figure 3.1. It is evident that the system starts out marginally stable for a low gain, and then the system quickly becomes unstable as the gain increases. The characteristics of the root loci are very similar for both actuator sets; the only noticeable differences are the crossing gains. The crossing gain is the proportional gain at which the root loci cross the imaginary axis from the left-hand plane to the right-hand plane. The actuator of Set one possesses a slightly larger crossing gain than the actuator of Set two. From this analysis the simple proportional control is deemed unsatisfactory.

3.2.1 Phase Compensation Technique - Absolute Position Feedback (APF)

It is thought that the inherent instability of the closed-loop system observed above is mainly due to the phase lag caused by the dynamics of the actuator. One of the common solutions to the problem is to incorporate a phase compensator [32, 34]. This approach is investigated in this section. The objective is to design a phase-lead compensator so that the stability of the overall closed-loop system is improved. A phase-lead compensation network is shown in Figure 3.2. The transfer function of the network is given by

$$G_c(s) = \frac{s + 1/T}{s + 1/(\alpha T)} \tag{3.3}$$

where $\alpha = R_2 / (R_1 + R_2)$ and $T = R_1 C_1$. Figure 3.3 shows the block diagram for the closed-loop system that incorporates the phase compensator with an absolute position feedback.

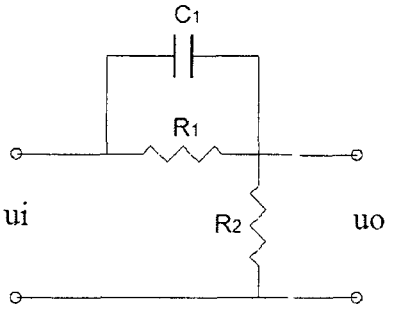

Figure 3.2. The analogue equivalent phase-lead compensation network

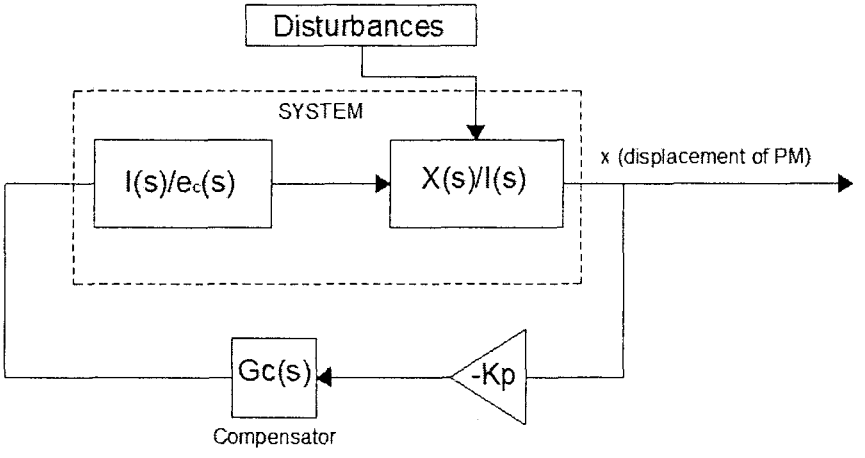

Figure 3.3. Block diagram of the APF with the phase compensation

The displacement transmissibilty is given by

$$TR(\omega) = \left|\frac{X(\omega)}{Y(\omega)}\right| = \left|\frac{cLs^2 + (cR + kL + 2\gamma k_v)s + kR}{mLs^3 + (mR + cL)s^2 + (cR + kL + 2\gamma k_v)s + kR + 2\gamma K_p G_c(s)}\right|_{s=j\omega} \tag{3.4}$$

where $X(\omega)$ is the amplitude of the steady-state response of the mass and $Y(\omega)$ is the amplitude of the harmornic base excitation. There are three parameters to be determined: T, α, and K_p. An optimization problem is therefore formulated in order to find the best parameter values. The optimum parameter values are chosen so as to minimize the following objective function:

$$f = \|TR(\omega)\|_2 \text{ in the frequency range } 0 \le \omega \le \omega_u$$

where $\|\bullet\|_2$ denotes the second norm and ω_u is a prescribed upper bound for the frequency of interest. The optimization is subjected to the following constraints:

1. the poles of the characteristic equation of the closed-loop system must lie on the left-hand side of the complex plane or the closed-loop system must be stable.

2. $T_l \le T \le T_u$, $\alpha_l \le \alpha \le \alpha_u$, $K_{pl} \le K_p \le K_{pu}$

where T_l, α_l, K_{pl} and T_u, α_u, K_{pu} are the lower bounds and the upper bounds of the parameters, respectively. The sequential simplex algorithm was used in the numerical solution.

The frequency upper bound was prescibed to be $\omega_u = 200$ rad/s and the parameter bounds were $T_l = 0.025, \alpha_l = 5\times10^{-5}$, $K_{pl} = 7000$ and $T_u = 10$, $\alpha_u = 5\times10^{-3}$. For the upper bound of the feedback gain, three values were perscribed and they are given in Table 3.2. Numerous computations were conducted. Table 3.2 lists the parameters of the three optimum controllers for both of the actuator sets. Figures 3.4 and 3.5 compare the *TRs* obtained by the optimum controllers with the *TR* obtained by the passive isolator. Several observations can be drawn:

1. The active control greatly improves *TR* in the lower frequency region and suppresses *TR* at the resonance frequency of the original system.

2. Around the resonance freuquency of the closed-loop system, *TR* with control is greater than that without control, which means that, in such a frequency range, the passive isolator outperforms the active one.

3. The optimum feedback gain K_p always converges to the prescribed upper bound, which indicates that the higher the feedback gain, the smaller the resulting objective function.

4. With a significantly larger upper bound for the gain, the *TRs* for actuator Set one are less favourable than those obatined with actuator Set two. Around the resonant frequency of the closed-loop system, the *TRs* with actuator Set one are much greater than those with actuator Set two.

Table 3.2. The parameters of the optimum controllers with the APF

Actuator Set one	K_{pu}	K_p^*	T^*	α^*
Controller One	50000	4.9998×10^{4}	6.5589	1.6688×10^{-4}
Controller two	150000	1.4886×10^{5}	6.2335	1.1450×10^{-4}
Controller three	300000	2.9869×10^{5}	6.0172	8.7744×10^{-5}
Actuator Set two				
Controller One	50000	4.9962×10^{4}	3.8356	3.8412×10^{-4}
Controller two	100000	9.9998×10^{4}	2.3963	4.5600×10^{-4}
Controller three	150000	1.4999×10^{5}	1.9772	4.6512×10^{-4}

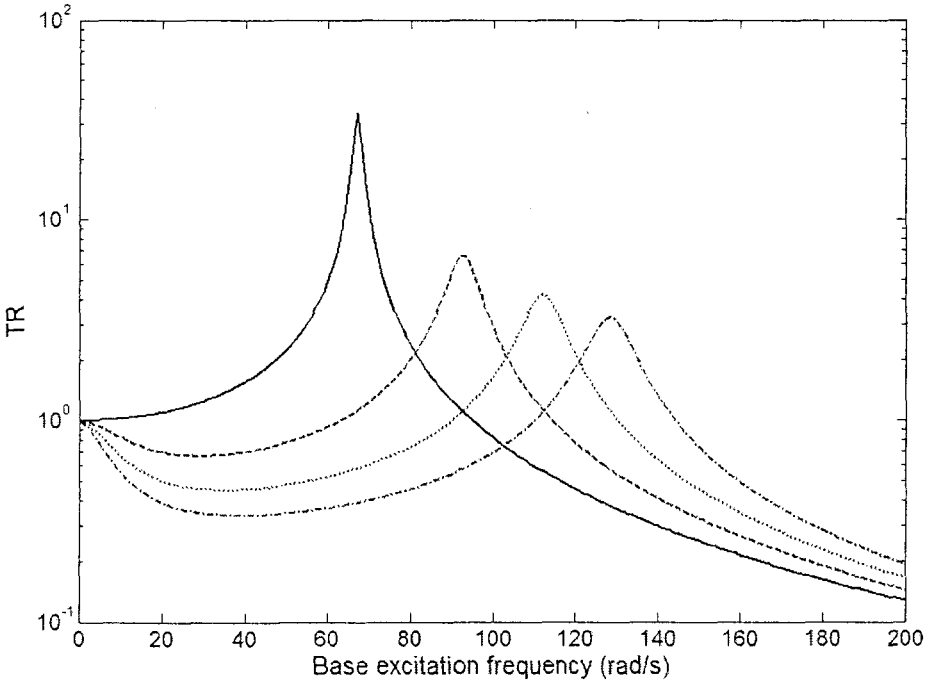

Figure 3.4. Comparison of the *TRs* (actuator Set one, APF): the passive isolator (solid); controller one (dashed), controller two (dotted), controller three (dash-dotted).

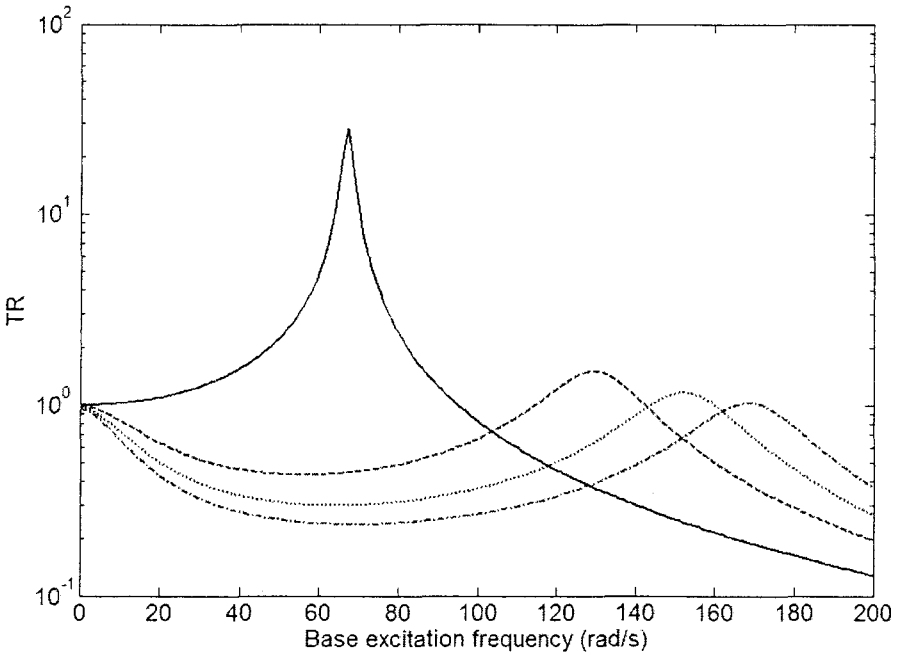

Figure 3.5. Comparison of the *TRs*, (actuator Set two, APF): the passive isolator (solid); controller one (dashed), controller two (dotted), controller three (dash-dotted).

Figures 3.6 and 3.7 illustrate the root loci of the closed-loop systems with the optimum controllers and actuator Set one and Set two, respectively. In the figures the asterisks designate the points that correspond to the optimal gains. It is seen that each case is asymptotically stable for the optimum gains. The effect of the increased upper bound on K_p can also be observed. As the upper bound on K_p increases, the effect that the compensator has on the systems character is more drastic, effectively pulling the roots further away from the imaginary axis.

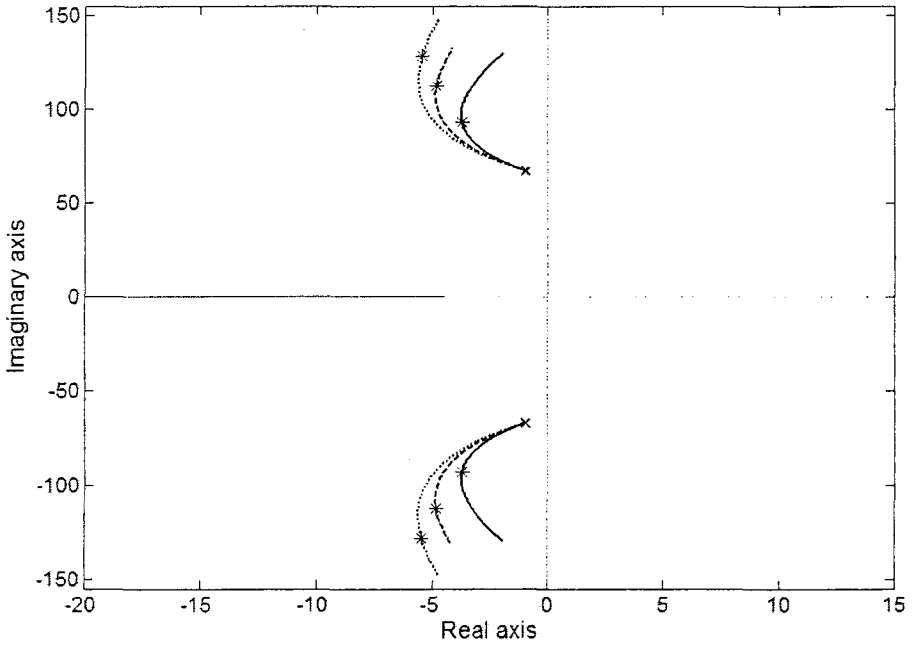

Figure 3.6. Root loci of the closed-loop systems (actuator Set one, APF): with controller one (solid), with controller two (dashed), with controller three (dotted).

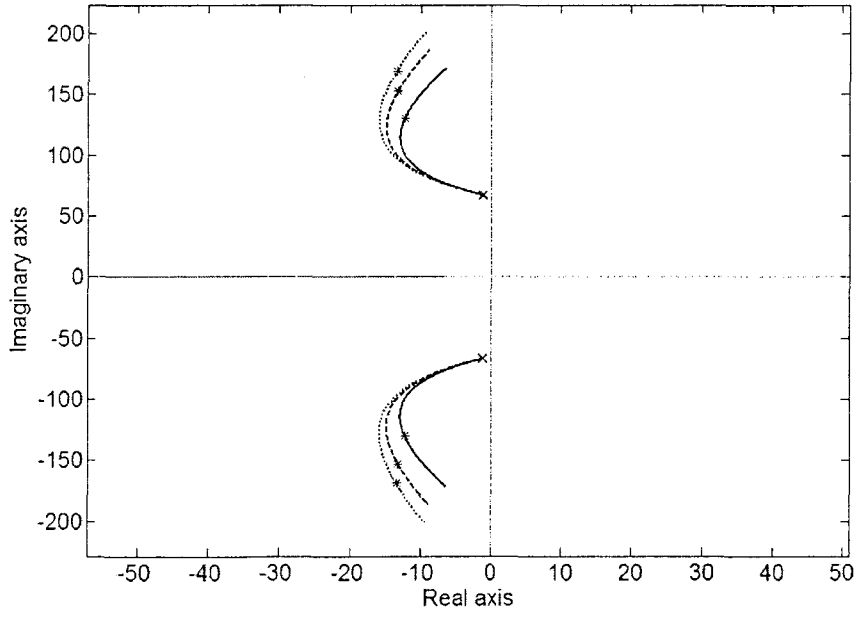

Figure 3.7. Root loci of the closed-loop systems (actuator Set two, APF): with controller one (solid), with controller two (dashed), with controller three (dotted).

3.2.2 Phase Compensation Technique - Relative Position Feedback (RPF)

For the RPF, the displacement transmissibility is given by

$$TR(\omega)=\left|\frac{X(\omega)}{Y(\omega)}\right|=\left|\frac{cLs^2+(cR+kL+2\gamma k_v)s+kR+2\gamma K_p G_c(s)}{mLs^3+(mR+cL)s^2+(cR+kL+2\gamma k_v)s+kR+2\gamma K_p G_c(s)}\right|_{s=j\omega} \tag{3.5}$$

In the same manner as Section 3.2.1 the controller parameters were obtained by optimizing the 2^{nd} norm of the transmissibility in the base excitation frequency region from 0 to 200 rad/s.

Numerical studies were conducted. It was found that increasing the upper bound on the gain did not have a significant effect on the results. Only when the upper bound was increased drastically did the results see a noticeable change. Thus, the upper bound for the gain was set at a constant value of 5×10^4 for both of the actuator sets. Table 3.3 lists the parameters of the optimum controllers for actuator Set one and Set two, respectively. Figure 3.8 shows two typical results. Notable differences between the APF and the RPF can be observed. Firstly, in a general sense the APF performs better than the RPF. Both the APF and the RPF are able to isolate vibration at frequencies close to the natural frequency of the open-loop system, but the APF results in $TR < 1$ for the low to middle frequency range, whereas the RPF does not provide such results. Secondly, the natural frequency of the closed-loop system with the RPF is lower than that with the APF. Finally, for both the APF and the RPF, actuator Set two outperformed actuator Set one.

Table 3.3. The parameters of the optimum controllers with the RPF

Actuator Set one	K_{pu}	K_p^*	T^*	α^*
Controller One	50000	4.9997×10^4	9.0527	6.1227×10^{-5}
Actuator Set two				
Controller One	50000	4.9994×10^4	5.4497	8.8062×10^{-5}

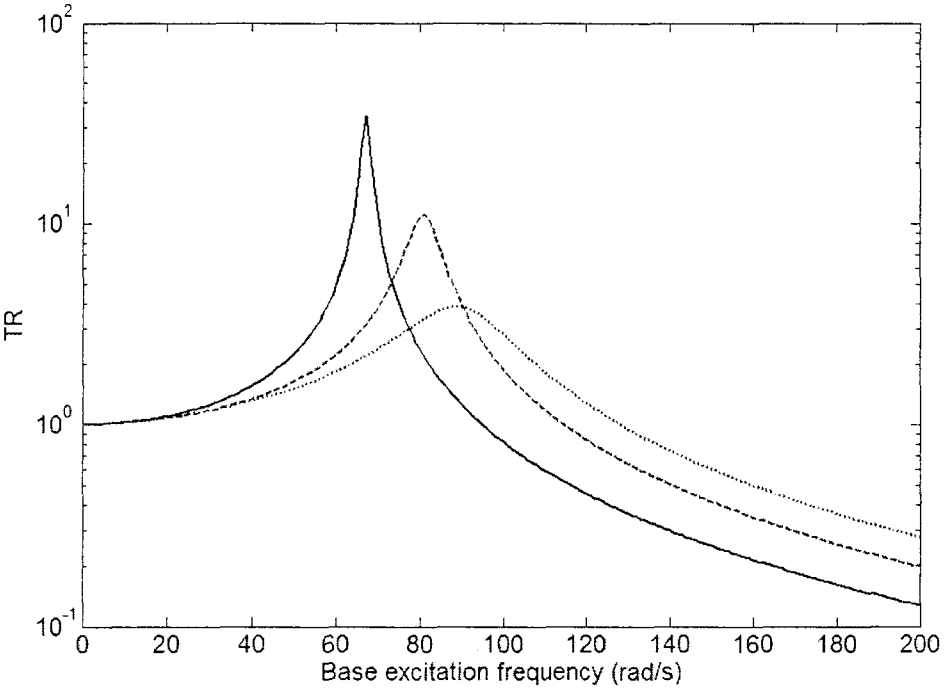

Figure 3.8. Comparison of the *TRs* with the RPF: passive isolator (solid); actuator Set one (dashed); actuator Set two (dotted).

3.3. Real Time Implementation

An experimental study was conducted in order to examine the effectiveness of the proposed control strategy for the active vibration isolator. Both actuator sets were tested with a gap distance of D = 100 mm. The experiments included two parts. The first involved finding the best displacement transmissibility for each of the actuator sets. This was done by subjecting the base to a sinusoidal excitation and measuring the steady-state responses of both the mass and base. The second part was to develop an automatic on/off control such that the control system is capable of deciding whether the active control is needed. A personal computer equipped with a data acquisition (DAQ) board (dSpace 1104) was used to collect signals and to generate control inputs. Simulink was used in conjunction with dSpace Control Desk software in order to implement the control. A sampling frequency of 1000 Hz was used in the real time implementation. Only the results using the APF are presented.

Figure 3.9 shows a Simulink model used in the first part of the experimental study. A laser position sensor (Wenglor, CP24MHT80) was used to measure the absolute displacement of

the mass through ADC_C5 (analog-to-digital conversion). The signal was subtracted from a set point which was the equilibrium position of the mass. The position difference was fed into the phase compensator. The output of the phase compensator was multiplied by the gain before being sent to DAC_C5 (digital-to-analog conversion), with DAC_C5 being the channel connected directly to the power amplifier (Quanser, UPM-2405) that drives the actuator. A manual switch was used to control whether to activate the active control. Two accelerometers (Brüel & Kjær, 4393V), one placed on the mass and one on the base were used to measure the acceleration signals. The acceleration of the base was acquired through ADC_C8 while the acceleration of the mass through ADC_C7. Both signals were fed to a low-pass filter with a cut-off frequency of 23.87 Hz or 150 rad/s. An S-function "buffer" was used to collect a group of 2048 samples. Next, an S-function "RMS" was used to compute the RMS value of the 2048 samples. The displacement transmissibility was computed by dividing the RMS value of the mass acceleration signals by the RMS value of the base acceleration signals. This could be computed online or offline. Finally, a sinusoidal signal generated by a sin function generator was fed to DAC_C1. The output signal from DAC_C1 was fed into a power amplifier (Brüel & Kjær, 2706) to drive a shaker (Brüel & Kjær, 4809) that was used to excite the base.

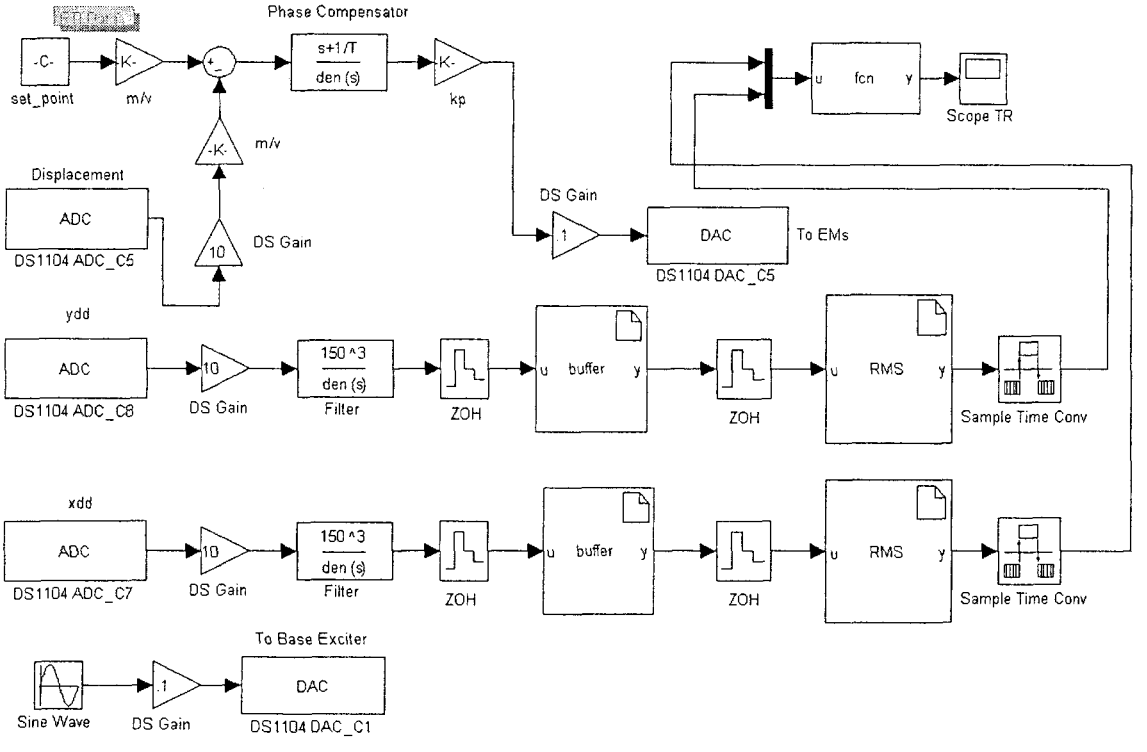

Figure 3.9. Simulink real time model for measuring TR.

Figures 3.10 and 3.11 show the results with actuator Set one while Figures. 3.12 and 3.13 give the results with actuator Set two. On the other hand, Figures 3.10 and 3.12 compare the responses without control and with control, and Figures 3.11 and 3.13 compare three *TRs* under different conditions. In the figures, the experimental *TR* was the best performance achieved by the isolator either in the active mode or in the passive mode. The frequency corresponding to the peak in the experimental *TR* is referred to as the switching frequency in this study. When the exciting frequency was below the switching frequency, the isolator was in its active mode; otherwise the isolator was in its passive mode. The results show that the active control was able to significantly suppress the base excitation, and actuator Set two outperforms actuator Set one.

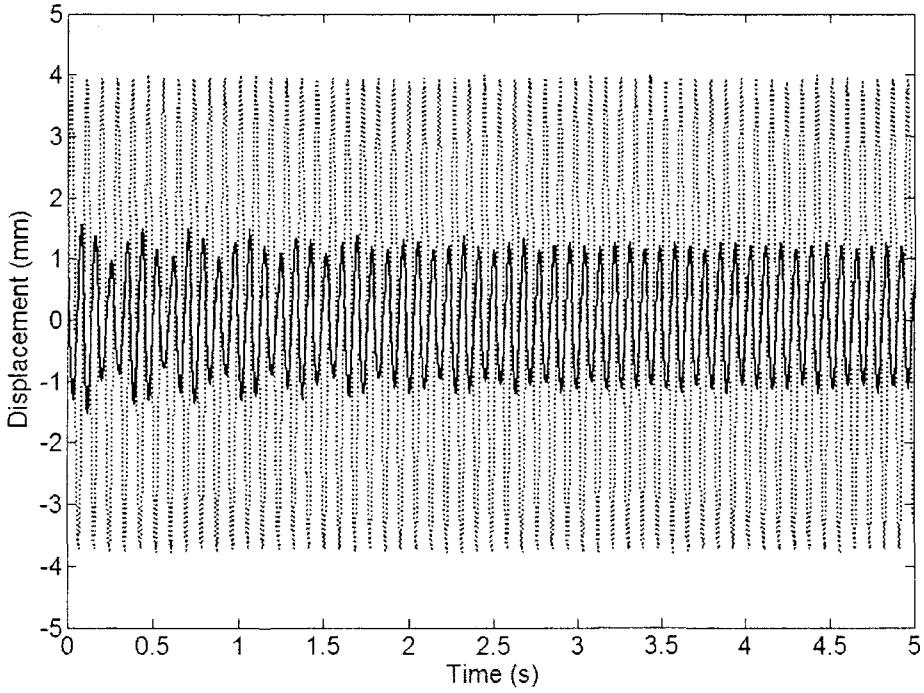

Figure 3.10. Response of the mass to a sinusoidal base excitation ($\omega = 75$ rad/s): without control (dotted); with control by actuator Set one (solid).

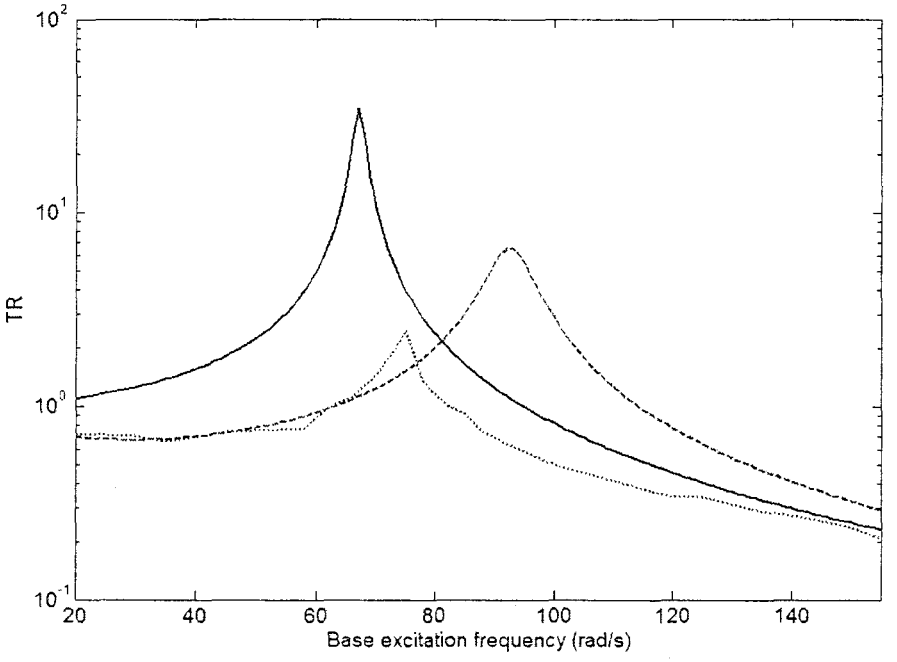

Figure 3.11. Comparison of *TRs*: analytical TR for the passive isolator (solid); analytical *TR* with control (dashed); best experimental *TR* (dotted).

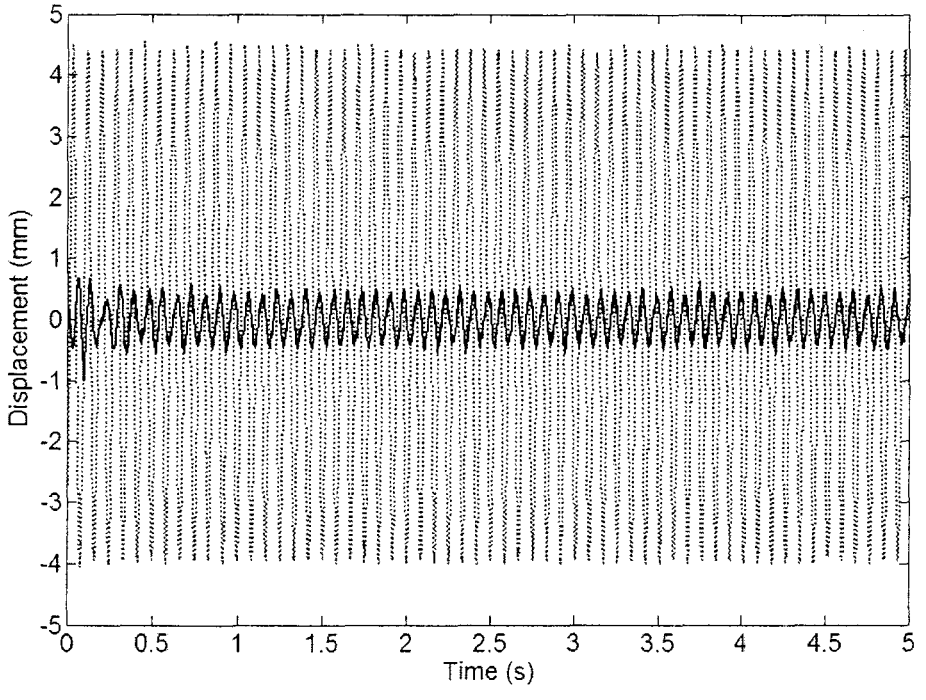

Figure 3.12. Response of the mass to a sinusoidal base excitation ($\omega = 75$ rad/s): without control (dotted); with control by actuator Set two (solid).

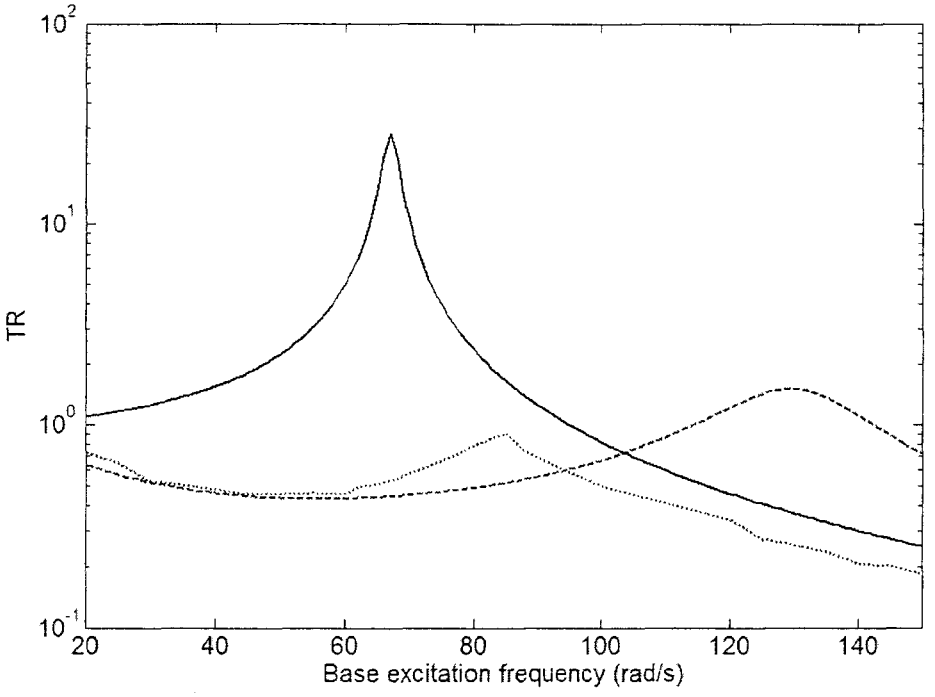

Figure 3.13. Comparison of *TRs*: analytical *TR* for the passive isolator (solid); analytical *TR* with control (dashed); best experimental *TR* (dotted).

The need for an automatic switch control arises from the fact that the active isolator performs better than the passive isolator only in a low to mid-frequency range. This requires that the control system be able to activate the active control only when it is needed. Figure 3.14 shows a Simulink model that implements an automatic on/off control.

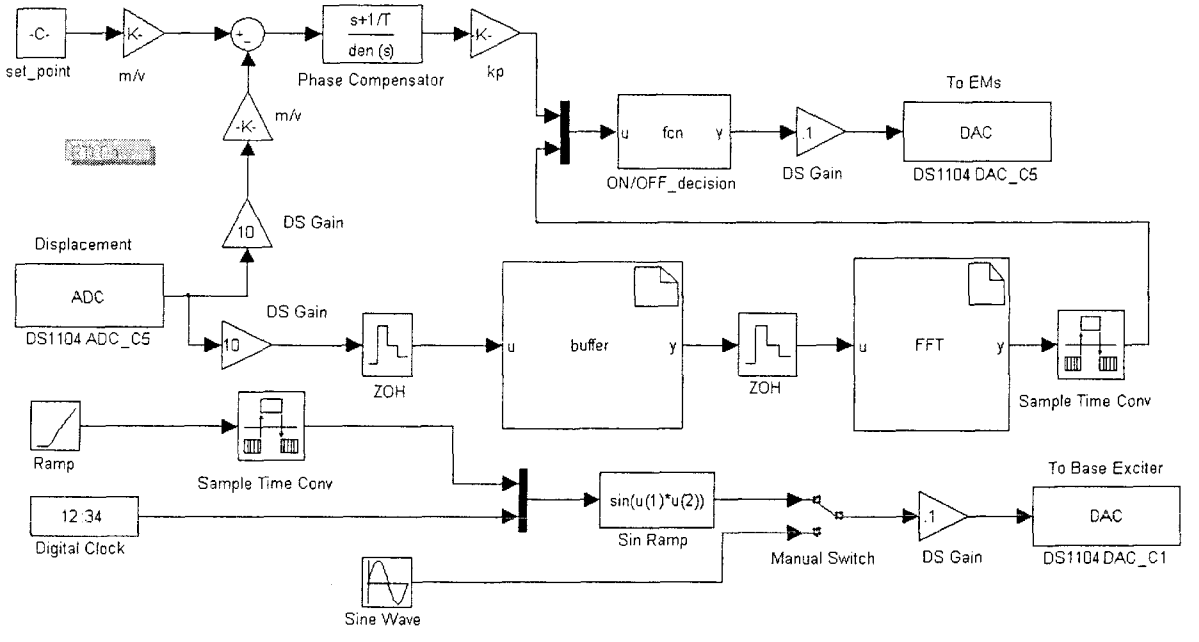

Figure 3.14. Simulink real time model for automatic on/off control

For the implementation of the automatic on/off control, the displacement signal from ADC_C5 was utilized both to generate a control effort and to determine whether to activate the control effort. The fast Fourier transform (FFT) was used to determine the dominant frequencies in the displacement response from a collected 2048 samples. To do so, a group of 2048 samples was collected with an S-function named "buffer", and they were then sent to an S-function named "FFT". The output of this S-function was the two frequencies corresponding to the first two highest peaks in the FFT spectrum, the primary and secondary frequencies. These two frequencies were then sent to an embedded function named "ON/OFF_decision" where a decision was made in regard to which of the dominant frequencies was the excitation frequency. In most cases, the primary dominant frequency corresponded to the excitation frequency. However, there is a case in which the secondary dominant frequency is the actual excitation frequency. This happens when the response is dominated by a transient. A transient occurs

whenever the operating condition alters. For instance, a transient response is induced when the exciting frequency varies or when the system switches between the active mode and the passive modes. It was observed that only when the frequency of the transient was very close to the natural frequency of the passive isolator, the transient became dominant. Therefore, in "ON/OFF_decsion", the primary and secondary frequencies were compared to the predetermined natural frequency. In general, if the difference between the primary frequency and the natural frequency of the passive isolator was within the prescribed bound, the secondary frequency was taken as the exciting frequency. Once the excitation frequency was determined, the following rules were applied. If the excitation frequency was less than or equal to the switching frequency, the active control strategy was activated, or kept on if it was already on. If the excitation frequency was greater than the switching frequency, the active control strategy was switched off, or kept off if it was already off. In this manner, the excitation frequency was updated and compared with the switching frequency about every 2 seconds. In the following, only the results with actuator Set two and the APF were presented. The switching frequency is 82 rad/s as can be seen in Fig. 3.13.

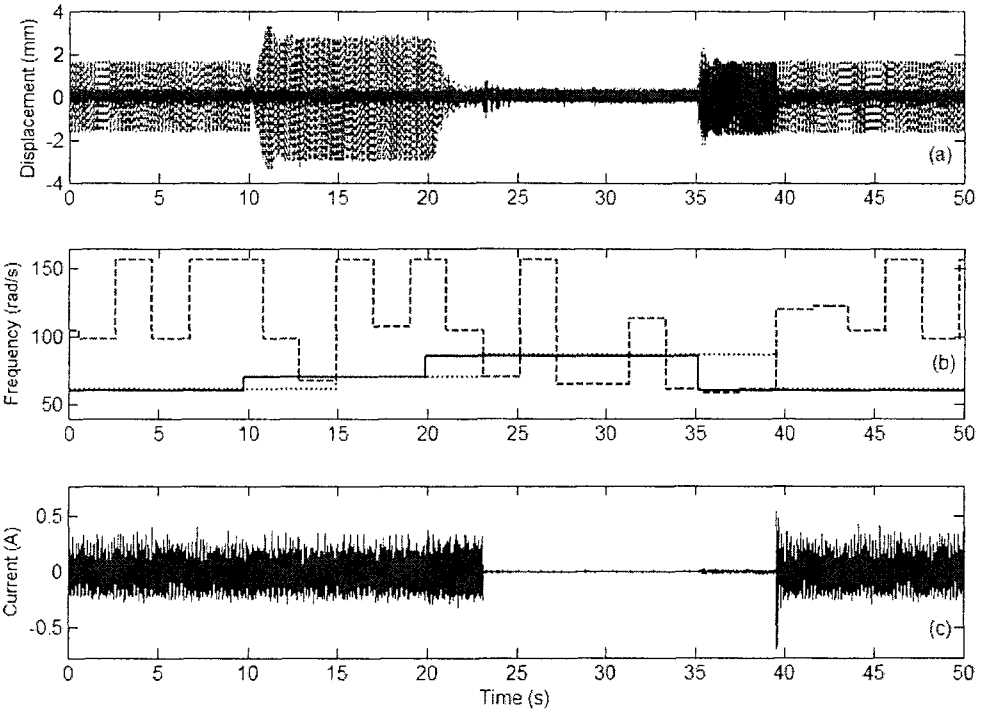

Figure 3.15. Experimental results, multi-step change: (a) response of the mass without control (dashed line), with control (solid line); (b) base excitation frequency (solid line), measured primary frequency (dotted line), measured secondary frequency (dashed line); (c) current of the actuator.

In order to illustrate the effectiveness of the on/off switching control in dealing with variable exciting frequencies, two testing scenarios were devised. The first scenario consisted of a multi-step change in the excitation frequency, and the second involved of a linear ramped up change in the excitation frequency. The experimental results for the first scenario can be seen in Figure 3.15. The step changes were as follows. For $0 \leq t < 10$ seconds the excitation frequency was 60 rad/s. At $t = 10$ seconds, the excitation frequency was changed to 70 rads/s. Then at $t = 20$ seconds the excitation frequency was changed to 85 rad/s which was followed by a final change at $t = 35$ seconds to a frequency of 60 rad/s. Without control, the response of the mass increased with time and reached maximum amplitude when the excitation frequency was close to the resonant frequency. After the exciting frequency surpassed the resonant frequency, the response started to decrease. With control, the response of the mass was kept at a low magnitude. Also, at about 23 seconds the automatic switch recognized the need to switch off the active control effort,

resulting in a response similar to that of the passive isolator. It also recognized the need to switch the active controller back on just before 40 seconds.

For the linear ramp up scenario, the excitation frequency was linearly varied from 20 rad/s to 120 rad/s between 0 and 50 seconds. The results for this scenario are given in Figure 3.16. It is seen that, without control the system response increased drastically through resonance and then dropped subsequent to resonance. With the proposed control action the system responded with minimal vibration through the entire frequency range. The automatic on/off switch control was successful in switching off the control when the frequency of excitation reached the switching frequency. It was also successful in recognizing the transient that the system exhibited when the control was switched off. This can be observed at around 35 seconds in Figure 3.16 where the secondary frequency was correctly chosen as the excitation frequency.

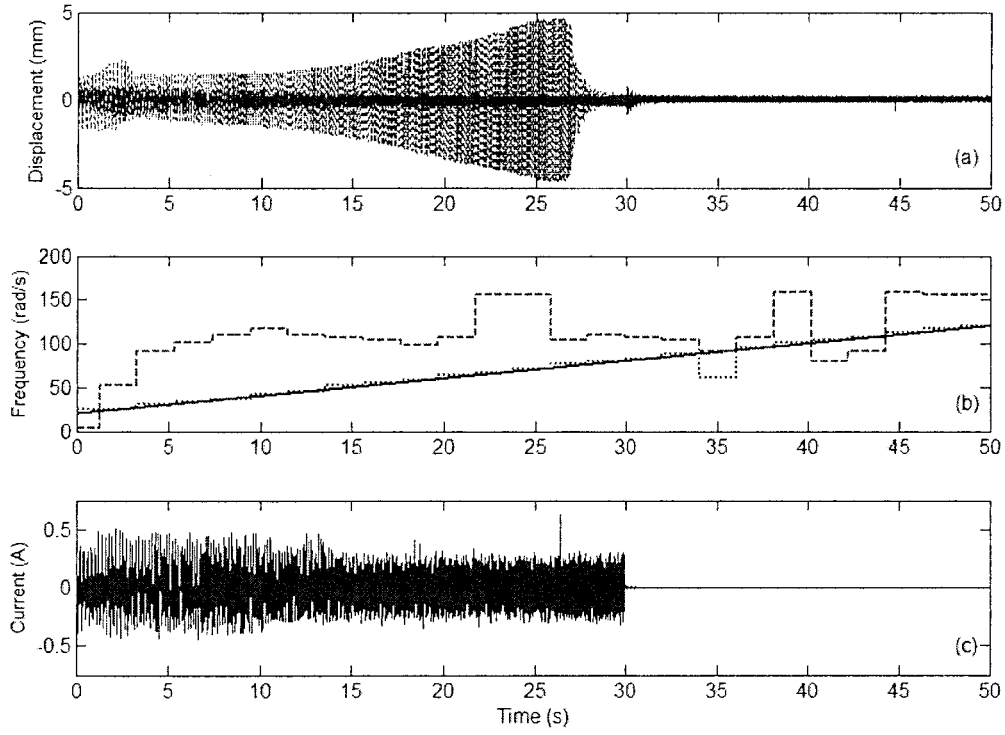

Figure 3.16. Experimental results, linear ramp change: (a) response of the mass without control (dashed line), with control (solid line); (b) base excitation frequency (solid line), measured primary frequency (dotted line), measured secondary frequency (dashed line); (c) current of the actuator.

3.4. Conclusions

In this chapter, a phase compensation technique for the proposed active vibration isolator has been developed. The linearized dynamic models for both the mechanical system and the actuator have been utilized along with the system characterization from chapter 2. The stability study has shown that the proportional feedback has a narrow stability margin due to the inherent dynamics of the actuators. A phase-lead compensator has been employed to improve the stability of the closed-loop system. An optimization problem has been formulated to determine the optimum parameters for the controllers by minimizing the second norm of the displacement transmissibility. Both the absolute position feedback and relative position feedback have been considered. The optimization results have shown that with the optimum controller and the absolute position feedback, the active vibration absorber can effectively isolate base excitation in a low to middle frequency range. An experimental study has been conducted. The best displacement transmissibility of the isolator has been determined experimentally. An on/off switch control strategy has been devised to take full advantage of both the passive isolator and active isolator. The testing results have demonstrated the effectiveness of the on/off switching control.

CHAPTER 4 - TIME DELAYED POSITION FEEDBACK CONTROL

This chapter investigates another technique to effectively utilize the proposed active vibration isolator, namely, the notion of a delayed feedback controller for active vibration isolation. Section 4.1 provides a review of related research. It also outlines some main findings. In section 4.2 a direct position feedback for both negative and positive gains are investigated. Section 4.3 deals with the idea of purposefully injected delays and analyzes perturbations in stability and variations in system character. Subsequently, section 4.4 investigates the design of a delayed feedback strictly for active isolation. Finally, the experimental implementation and performance character of the controllers developed are discussed, and the conclusions drawn.

4.1. Introduction

Time delays in active control systems are caused by a number of factors. For example, the sensing and computing methodologies which involve filtering data, calculating control signals, and applying these control signals through actuators, all of which take time to complete. The causes of time delays can be grouped into two categories, hardware and software sources [32]. This time delay, also referred to as a phase lag, historically was regarded as detrimental and thought to have only a negative effect on the control system. Methods for compensating this time delay have been investigated by many researchers [38-39]. In general, they attempt to compensate for the delays by incorporating a phase lag compensator or by including the actuator dynamics in control design. In fact, chapter 3 examined a phase compensation scheme. In such methods, that intend to alleviate the delay, the time delay is considered relatively small compared to the fundamental period of vibration. However, in complex systems, or simply those that have a relatively high natural vibration frequency, the time delays can encompass a significant portion of the period of natural vibration. In this regime, a compensation method may not always suffice.

It has been known for some time that an intentional introduction of time delays into the feedback loop of the control algorithm can in fact enhance stability and performance. Some notable studies in this area and related areas can be found in [40-48]. More particularly relevant to this study are the recent studies conducted in [45-48] where delayed feedback signals were used for the active suppression of vibrations in structures. In a slightly different context, time delays have been used to design active vibration absorbers, namely the delayed resonator [49,50]. Also, in [51] it is shown that the delayed resonator is equivalent to a PD controller. Most of these studies focused on negative delayed feedback control. In [47], time delayed positive velocity

feedback was proposed to control vibration of a single degree-of-freedom (DOF) system. The study showed that the introduction of a suitable time delay not only made the system stable, but also improved the performance compared to time delayed negative velocity feedback. In [48], time delayed positive position feedback was applied to active base isolation. Using a SDOF system as an example, the study demonstrated that the proposed control was superior to direct negative proportional feedback terms of stability, structural response, and control effort.

Chapter 4 therefore explores how to employ time delayed proportional feedback control for the proposed active isolator [52]. Absolute position feedback as well as a relative position feedback are considered for both a direct feedback and a delayed feedback. In the meantime, direct feedback (negative and positive), and delayed feedbacks are investigated. The research in this chapter differs from previously published research in three aspects. First, the system under current investigation possesses a coupled dynamics arising from a mechanical system and an actuator system. Thus different from [47, 48] effects of the inherent time delay caused by the actuator is dealt with. An interesting finding is that for base isolation, some degree of time delay inherent in hardware is beneficial when a direct positive position feedback is used. Second the present study proposed an optimum design procedure for delayed feedback controllers. Various optimum controllers were found and their performances were compared. Finally, analytical and numerical results are validated experimentally.

4.2. Direct Position Feedback Control

First the direct position feedback stability issue is revisited. A direct negative stability analysis was first conducted in Section 3.2 of this thesis. These results are now amalgamated with this section and a more detailed analysis is presented. Both negative position feedback (NPF) and positive position feedback (PPF) are now considered. The characteristic equation (3.2) governs the stability of the system. Figure 4.1 shows the root loci for both the NPF and the PPF. In the case of the NPF, an increase in K_p causes a pair of complex conjugate poles to move from the left-hand plane (LHP) to the right-hand plane (RHP), whereas in the case of the PPF, an

increase in K_p causes the real pole to move from the LHP towards the RHP eventually crossing the imaginary axis.

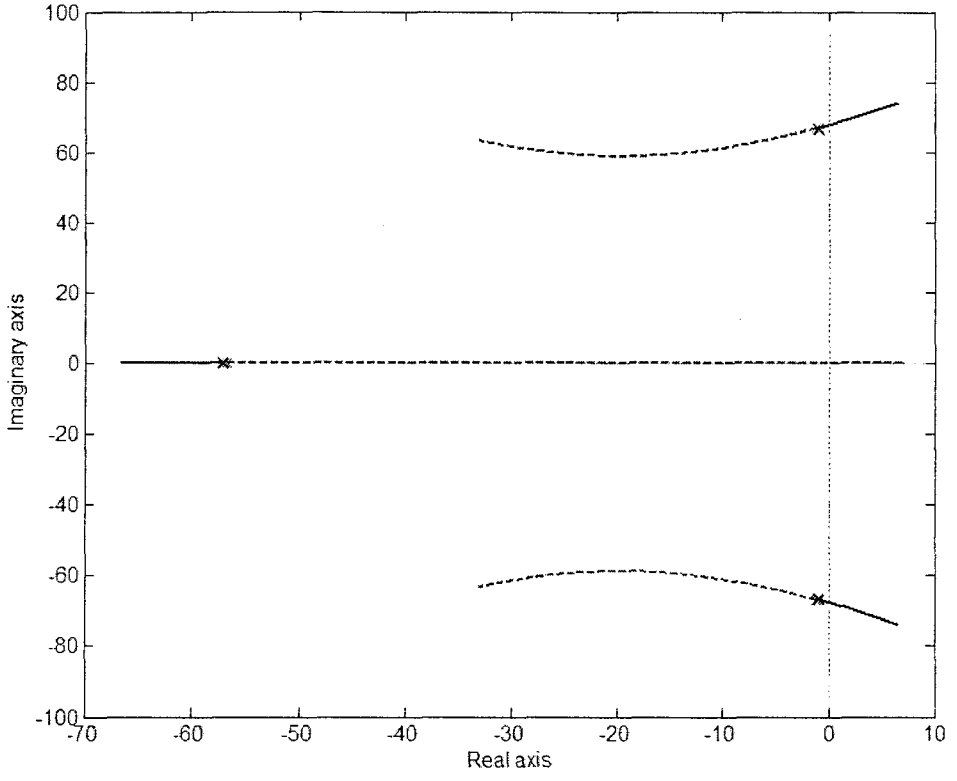

Figure 4.1. Root loci of the closed-loop system, Set two: NPF (solid line); PPF (dashed line).

In this study, the minimum gain at which the root locus or loci cross the imaginary axis is referred to as the crossing gain. For a realistic system, the roots of equation (3.2) consists of one real number denoted as r_1 and a pair of complex conjugates denoted as r which can be expressed as

$$r = -\sigma \pm j\omega_d = -\omega_n\zeta \pm j\omega_n\sqrt{1-\zeta^2} \tag{4.1}$$

where ω_n and ζ are referred to as the equivalent natural frequency and damping ratio, respectively. In Appendix B, it is shown that the crossing gains for the NPF and the PPF are given by

$$\hat{K}_P = \frac{1}{2\gamma}\left(\left(\frac{Rc}{mL}+\frac{k}{m}+\frac{2\gamma k_v}{mL}\right)\left(\frac{R}{L}+\frac{c}{m}\right)mL - kR\right) \tag{4.2}$$

and

$$\hat{K}_P = -\frac{kR}{2\gamma} \tag{4.3}$$

respectively. For example, using the system parameters for Set one, it is found that for the NPF, $\hat{K}_P = 127.06$ and for the PPF, $\hat{K}_P = -1247.90$. For Set two, the two crossing gains are $\hat{K}_P = 103.21$ (NPF), and $\hat{K}_P = -1410.08$ (PPF). It is noted that the gain magnitude for the PPF is much higher than that for the NPF. This indicates that the NPF is not acceptable as its permissible gain is low, which results in an insufficient control effort.

Next the transmissibility ratio (TR) is considered. The TR for the APF is given by

$$TR(\omega) = \left|\frac{X(\omega)}{Y(\omega)}\right| = \left|\frac{cLs^2 + (cR + kL + 2\gamma k_v)s + kR}{mLs^3 + (mR + cL)s^2 + (cR + kL + 2\gamma k_v)s + kR + 2\gamma K_P}\right|_{s=j\omega} \tag{4.4}$$

whereas the TR for the RPF is given by

$$TR(\omega) = \left|\frac{X(\omega)}{Y(\omega)}\right| = \left|\frac{cLs^2 + (cR + kL + 2\gamma k_v)s + kR + 2\gamma K_P}{mLs^3 + (mR + cL)s^2 + (cR + kL + 2\gamma k_v)s + kR + 2\gamma K_P}\right|_{s=j\omega}. \tag{4.5}$$

where $X(\omega)$ is the amplitude of the steady-state response of the mass and $Y(\omega)$ is the amplitude of a harmonic base excitation. Figures 4.2 and 4.3 compare the TR of the open-loop system and the TRs with the APF and with the RPF, respectively. For brevity, only the transmissibility ratios associated with Set two are shown. The TRs with control were generated using $K_P = 16.0$ for the NPF and $K_P = -1384.8$ for the PPF. These gains were determined such that the poles are located in the LHP and away from the imaginary axis at a stability margin of 1.0. In this study, the stability margin is defined as the minimum distance between the poles and the imaginary axis. Figure 4.2 shows that in the case of the APF, the NPF degrades the TR while the PPF produces a satisfactory TR in the resonance region and a poor TR in the lower frequency range. Figure 4.3 shows that in the case of the RPF, the PPF yields a highly desirable TR while the NPF worsens the TR. The distinguishable feature between the NPF and the PPF can be explained by the effect of the feedback on the equivalent natural frequency and damping ratio. As shown in Figure 4.1,

in the PPF case, an increase of K_P decreases the equivalent natural frequency and increases the equivalent damping ratio, which lowers the TR overall. On the other hand, in the NPF case, an increase of K_P produces the opposite effect, which causes an increase of the TR around resonance.

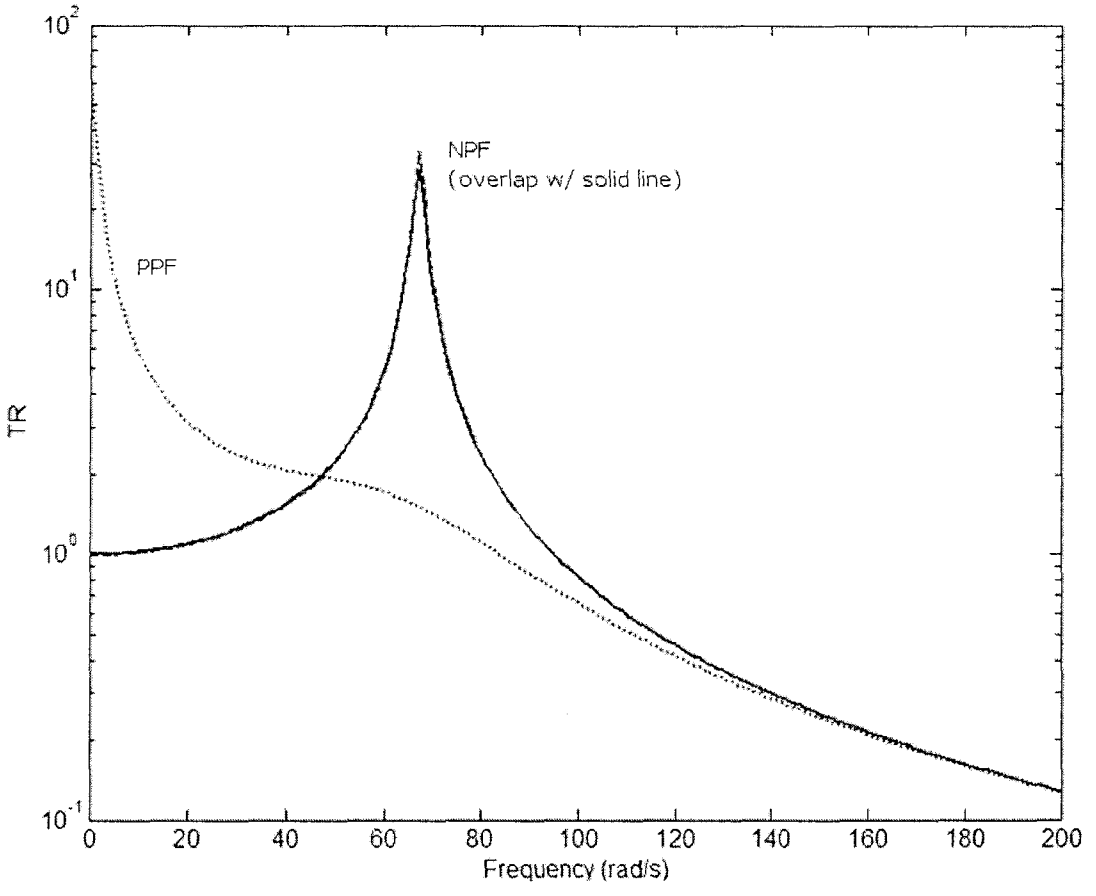

Figure 4.2. Comparison of the TRs: open-loop (solid line); negative APF (dashed line); positive APF (dotted line).

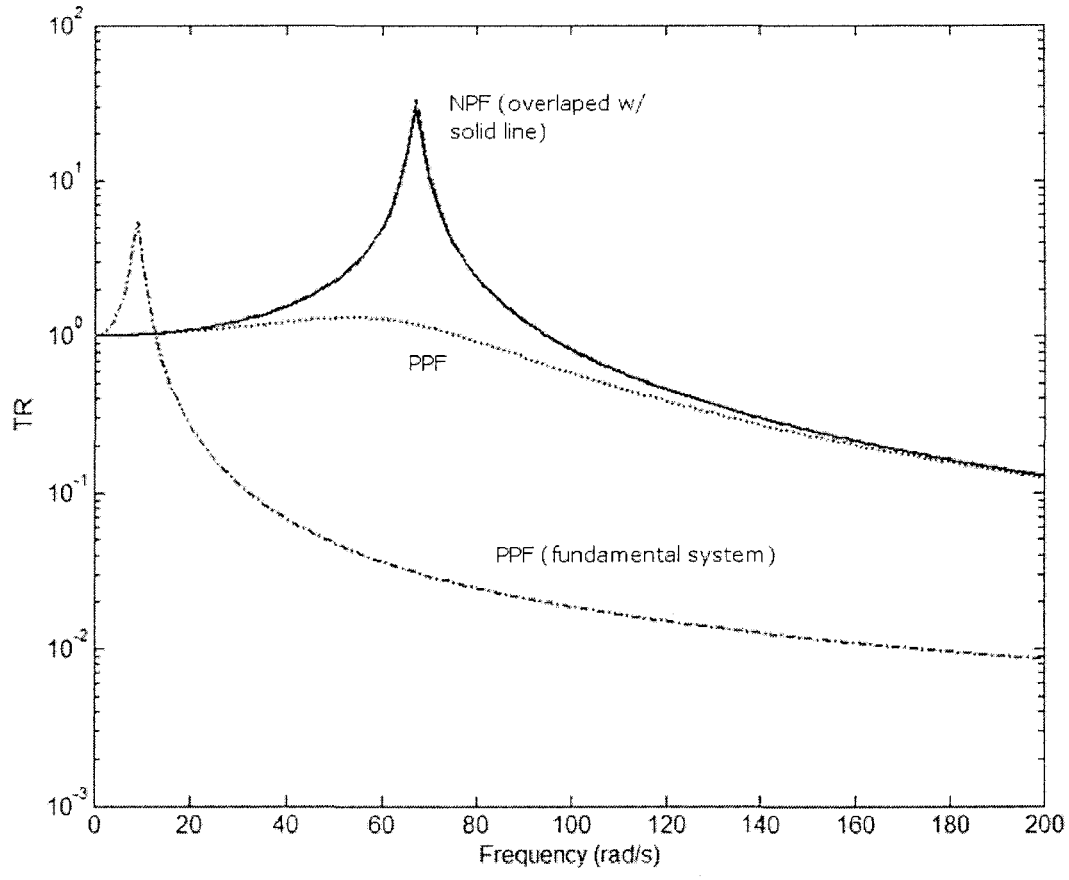

Figure 4.3. Comparison of the TRs: open-loop (solid line); negative RPF (dashed line); positive RPF (dotted line); positive RPF by neglecting the actuator dynamics (dash-dotted line).

Figure 4.3 also shows the TR of the closed-loop system without considering the actuator dynamics. Such a system is referred to as the fundamental system defined by

$$m\ddot{z} + c\dot{z} + kz = \frac{2\gamma}{R}\, e_c - m\ddot{y} \tag{4.6}$$

It can be seen that when the positive RPF is applied to the fundamental system, the TR at the low frequency region is amplified greatly, which is deemed unsatisfactory. The different performance between the fundamental system and the actual system deserves a further investigation. The dynamics of the actuator is mainly characterized by the time constant defined as $T_a = L/R$. Note that $T_a = 0.0174$ seconds for the given actuator Set two. The time constant is normalized by

$$T_n = T_a / T \tag{4.7}$$

where $T = 2\pi/\sqrt{k/m}$ is the natural period of the fundamental system. To examine the effect of the time constant on the PPF, the time constant was varied by keeping the resistance constant and changing the inductance. Figure 4.4 shows the root loci of the closed-loop system for four different normalized time constants. It can be seen that the magnitude of the time constant influences the progression of the complex conjugate poles. In general, as the time constant increases, the complex conjugate poles tend to move farther away from the real axis while the real pole shifts more towards the imaginary axis. When the time constant is zero or the system is fundamental, the feedback gain has no effect on the real part of the complex poles, or the poles move downward only. This indicates that when a PPF is employed, some degree of time delay caused by the actuator dynamics is beneficial as it assists to an enhancement of the damping level of the closed-loop system.

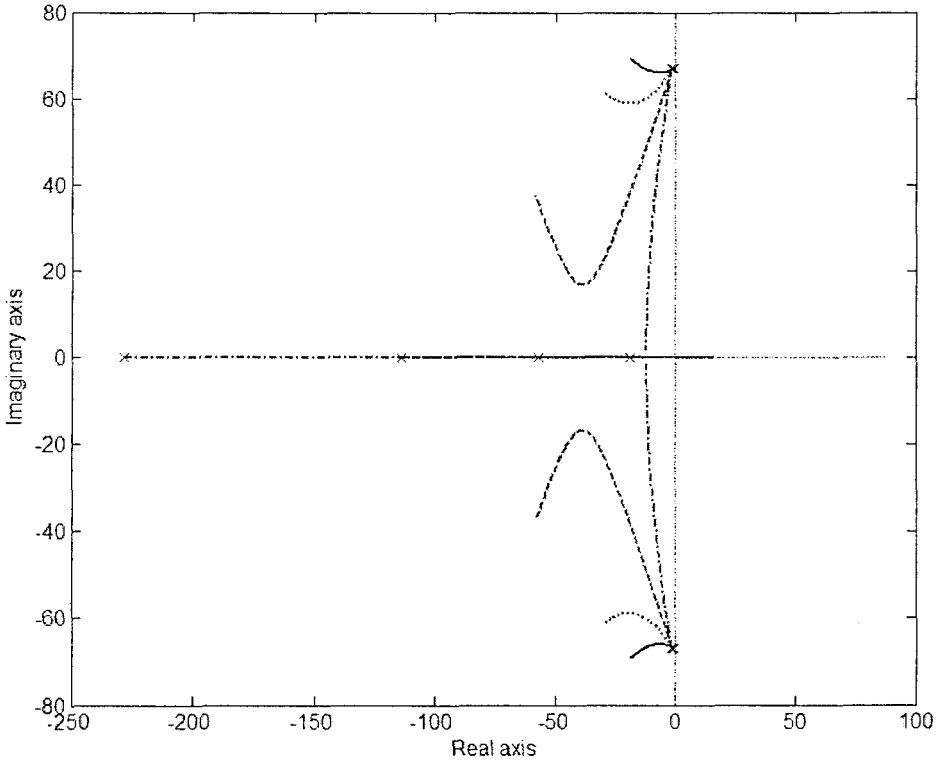

Figure 4.4. Root loci of the PPF closed-loop systems with different time constants: $T_n = 0.05$ (dash-dotted line), $T_n = 0.1$ (dashed line), $T_n = 0.2$ (dotted line), $T_n = 0.5$ (solid line).

4.3. Delayed Position Feedback Control

The previous section has shown that the negative direct position feedback is unsatisfactory while a positive direct position feedback can produce a very desirable result if the relative position signal is used, but an unacceptable result if the absolute position signal is used. In this section a time delayed position feedback is considered. The main purpose of the study is to determine the degree of performance improvement a delayed position feedback can achieve and what limitations it has when used in conjunction with the proposed system. Figure 4.5 shows a block diagram of the control loop. Consequently, the control efforts are represented by $e_c = -K_p x(t-\tau)$ and $e_c = -K_p z(t-\tau)$ for the APF and the RPF, respectively. The characteristic equation of the closed-loop system for both the APF and RPF is now

$$mLs^3 + (mR + cL)s^2 + (cR + kL + 2\gamma k_v)s + kR + 2\gamma K_p e^{-\tau s} = 0 \tag{4.8}$$

which is transcendental, complicating its analysis.

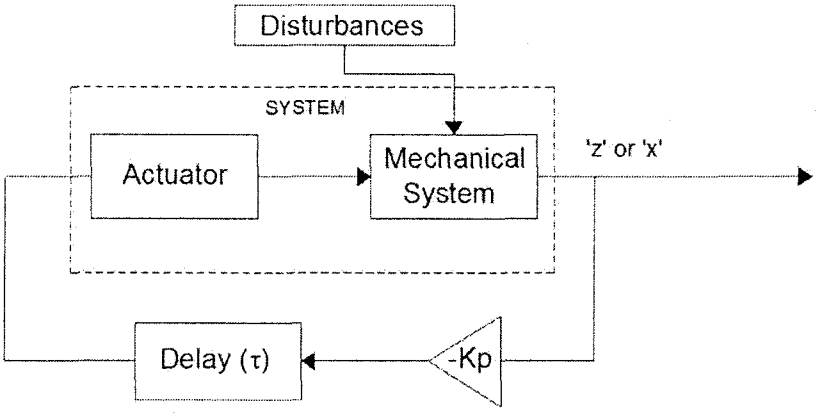

Figure 4.5. Block diagram of DFC control

A concern for a delayed feedback is the stability of the closed-loop system. The stability boundaries can be determined by the condition for which a root crosses the imaginary axis, indicative of movement from stability to instability, or from instability to stability. A bifurcation point is the critical value of a parameter that triggers a sudden or 'catastrophic' change in the response [5]. The gain and delay corresponding to a bifurcation point can be determined by substituting $s = j\omega$ in equation (4.8) or

$$-mL\omega^3 j-(mR+cL)\omega^2+(cR+kL+2\gamma k_v)j\omega+kR+2\gamma\hat{K}_P e^{-\hat{\tau}j\omega}=0 \tag{4.9}$$

where $\hat{K}_P$ and $\hat{\tau}$ are the crossing gain and delay respectively. Using Euler's identity and separating the imaginary and real parts of equation (4.9) yields

$$-(mR+cL)\omega^2+kR+2\gamma\hat{K}_P\cos(\hat{\tau}\omega)=0 \tag{4.10}$$

$$-mL\omega^3+(cR+kL+2\gamma k_v)\omega-2\gamma\hat{K}_P\sin(\hat{\tau}\omega)=0 \tag{4.11}$$

Solving equations (4.10) and (4.11) result in

$$\hat{K}_P=\pm\sqrt{\left(\frac{(mR+cL)\omega^2-kR}{2\gamma}\right)^2+\left(\frac{-mL\omega^3+(cR+kL+2\gamma k_v)\omega}{2\gamma}\right)^2} \tag{4.12}$$

$$\hat{\tau}=\frac{1}{\omega}\left(\tan^{-1}\left[\frac{-mL\omega^3+(cR+kL+2\gamma k_v)\omega}{(mR+cL)\omega^2-kR}\right]+n\pi\right) \text{ for } n=1,2,3,\cdots \tag{4.13}$$

Equations (4.12) and (4.13) represent all the possible gain-delay combinations that define the bifurcation lines except for the case when $\omega=0$. For this case equation (4.10) yields the solution given by

$$\hat{K}_P=\frac{-kR}{2\gamma} \quad \forall\tau \tag{4.14}$$

Using equations (4.10), (4.11) and (4.12), the gain-delay stability chart can be obtained as shown in Figure 4.6 for Set one and Figure 4.7 for Set two. The shaded regions represent the gain-delay combinations that lead to asymptotically stable solutions, while the unshaded region represents the gain-delay combinations that lead to unstable solutions. The system is seen to undergo successive bifurcations as the gain and/or the delay are varied. Furthermore, as can be observed from the stability charts, generally, the larger the delay time the smaller the stability region becomes for either Set.

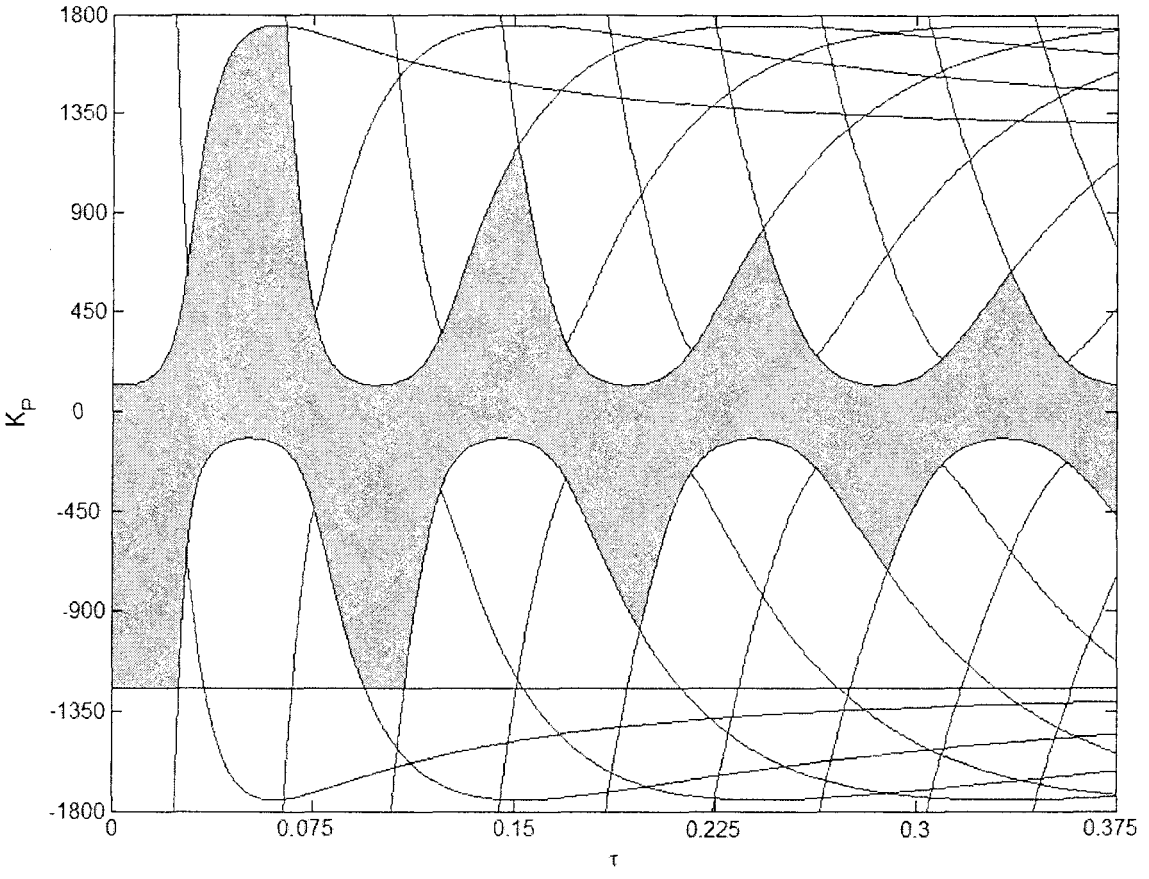

Figure 4.6. Gain-delay stability region, Set one

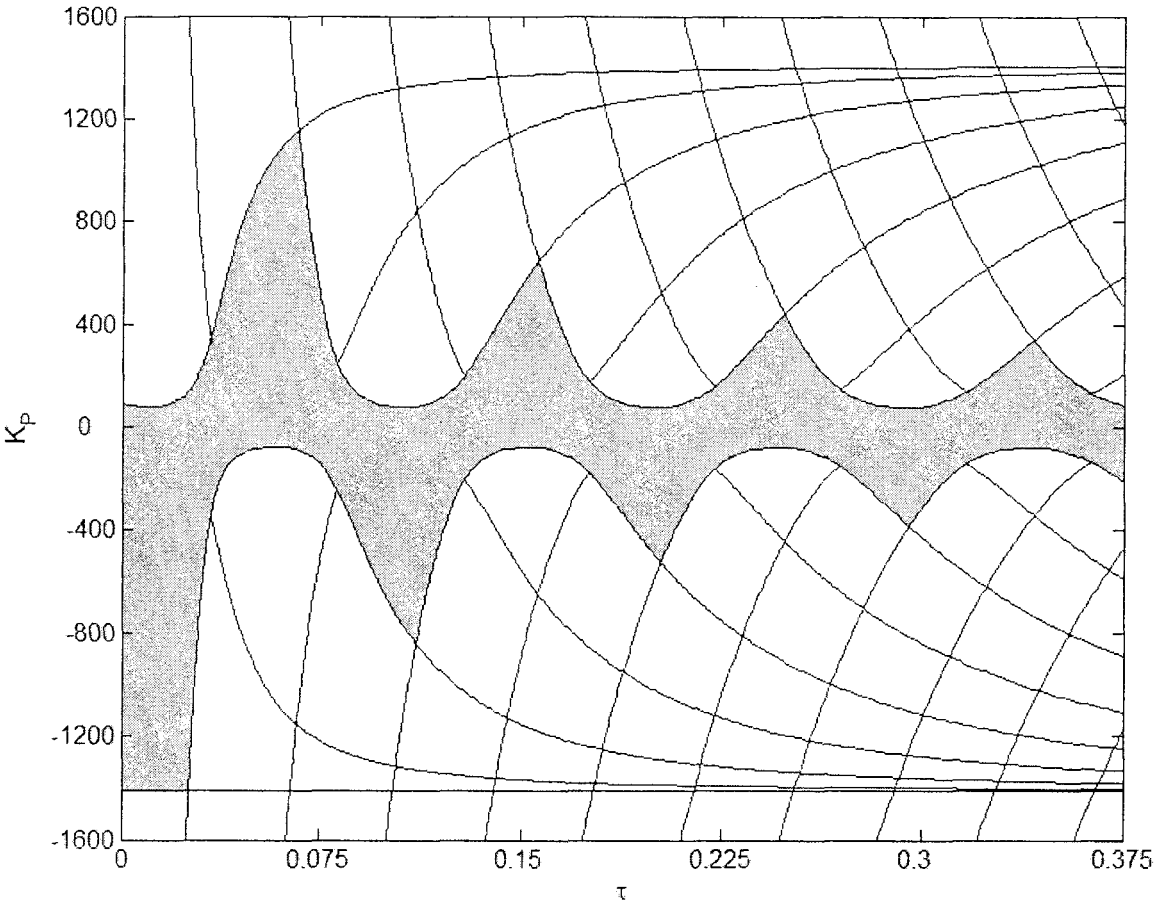

Figure 4.7. Gain-delay stability region, Set two

It is desired to understand how the gain and delay affect the poles of the closed-loop system. Due to the fact that the characteristic equation is transcendental, it is not possible to determine the roots analytically. For this reason, a numerical approach is utilized. As employed in [51], for a given time delay, τ, the exponential function in equation (4.8) can be approximated by a rational function using the Pade approximation. Consequently, the characteristic equation can be expressed in a polynomial form and its roots can be found with a root finding algorithm. The roots were computed by slowly varying the gain and delay and solving the characteristic equation, at each consecutive increment. In the Pade approximation an 8^{th} order polynomial was employed, thus adding eight additional roots to the characteristic equation to total eleven.

Figure 4.8 shows the root loci of the closed-loop system with the NPF for 3 different values of the proportional gain while varying the delay, τ, for Set one. Likewise, Figure 4.9 shows the same root loci progression for Set two. Illustrated in both figures are the four roots that

are closest to the imaginary axis, two of which are system poles and two of which are non-system poles. A system pole is defined as the pole whose root locus originates from a pole of the open-loop system [53]. In general, for any given constant gain the root loci progress to the right when the delay is increased. More importantly, as the gain is increased the root loci tend more towards the right at a faster pace, and can cross over to the RHP at a lesser value of time delay. The cases for the PPF are shown in Figures 4.10 and 4.11. Only the system poles are shown due to the fact that for the PPF case the non-system poles lie much further to the left or much further up the imaginary axis for both Sets. It is noted that the gain magnitude affects mainly the horizontal location of the poles when the delay is zero. The greater the gain magnitude, the further left the complex system poles are located and the further right the real system pole is. With an increase of the delay, the system poles moves towards the RHP. Comparing Set one with Set two, one can observe that for the NPF and PPF cases the root progression for the two Sets exhibited similar patterns. The only notable difference between the Sets was the fact that for Set two the magnitudes of the real part of the complex conjugate poles for the PPF case were larger than that of Set one.

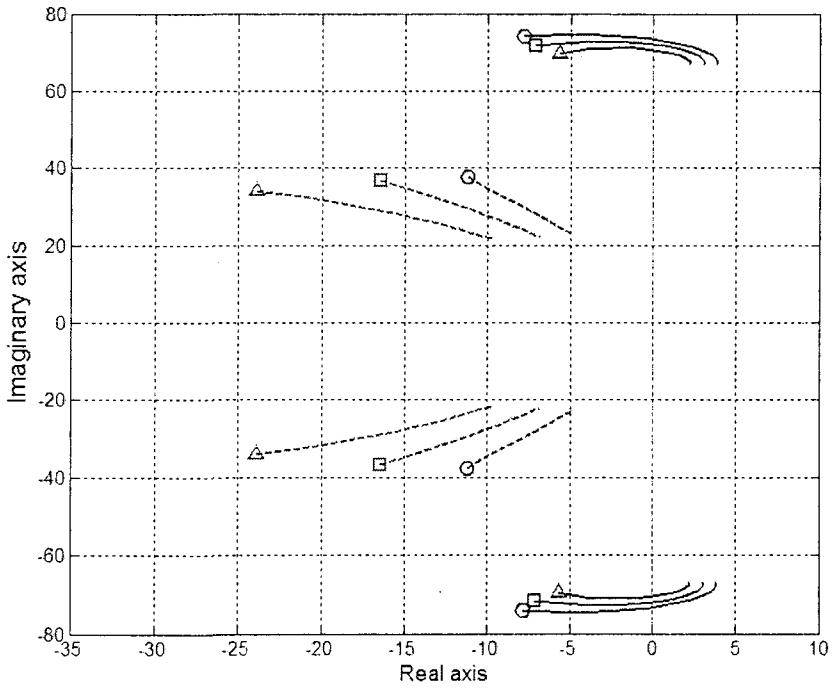

Figure 4.8. Root loci of the closed loop system with NPF (Set one, varying τ between 0.05 and 0.1 second), $K_P = 500$ (triangle), $K_P = 700$ (square), $K_P = 900$ (circle), system poles (solid), non-system poles (dashed)

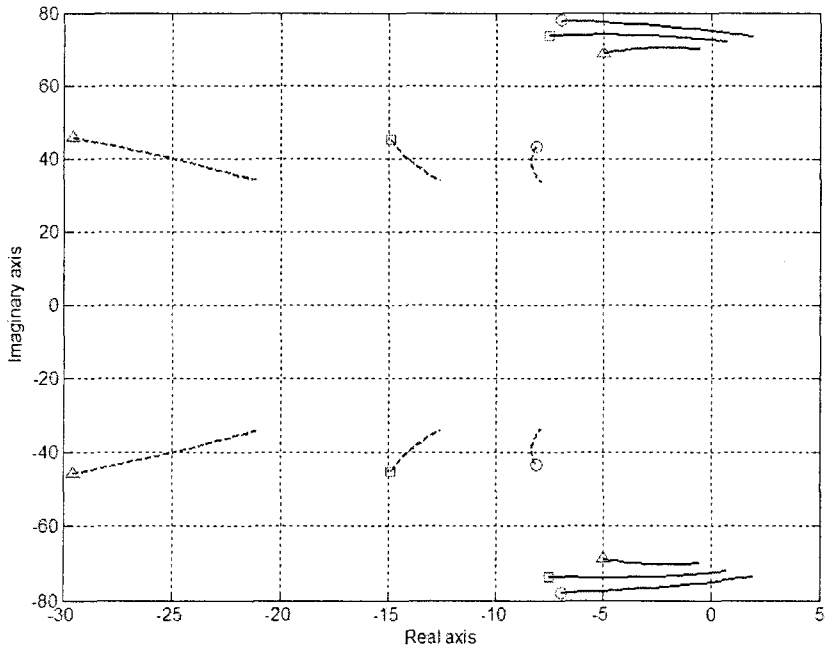

Figure 4.9. Root loci of the closed-loop system with the NPF (Set two, when τ is increased from 0.06 to 0.08 second) $K_P = 200$ (triangle); $K_P = 400$ (square); $K_P = 600$ (circle); system poles (solid line), non-system poles (dashed line).

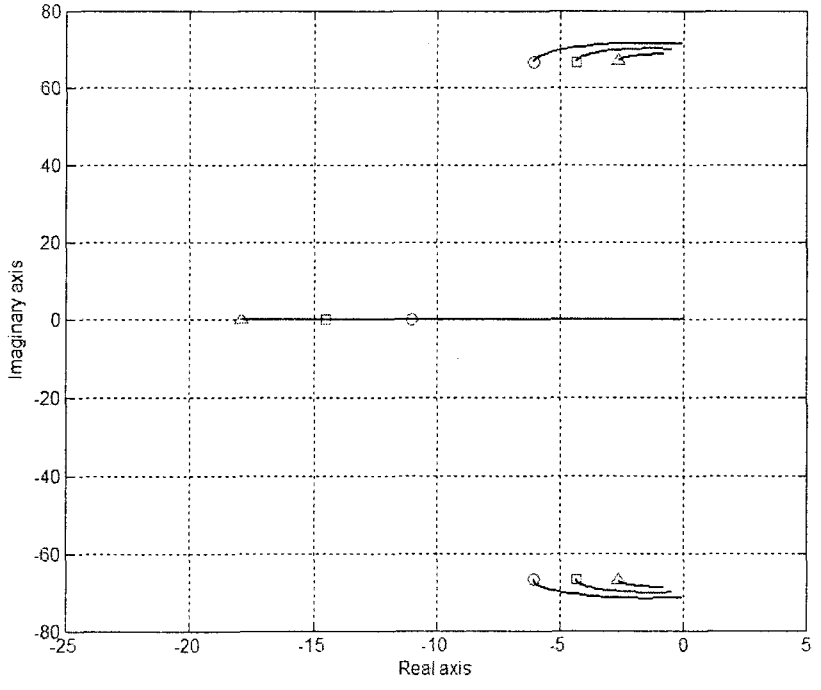

Figure 4.10. Root loci (system poles) of the closed-loop system with the PPF (Set one, when τ is increased from 0 to 0.03 second) $K_P = -200$ (triangle); $K_P = -400$ (square); $K_P = -600$ (circle)

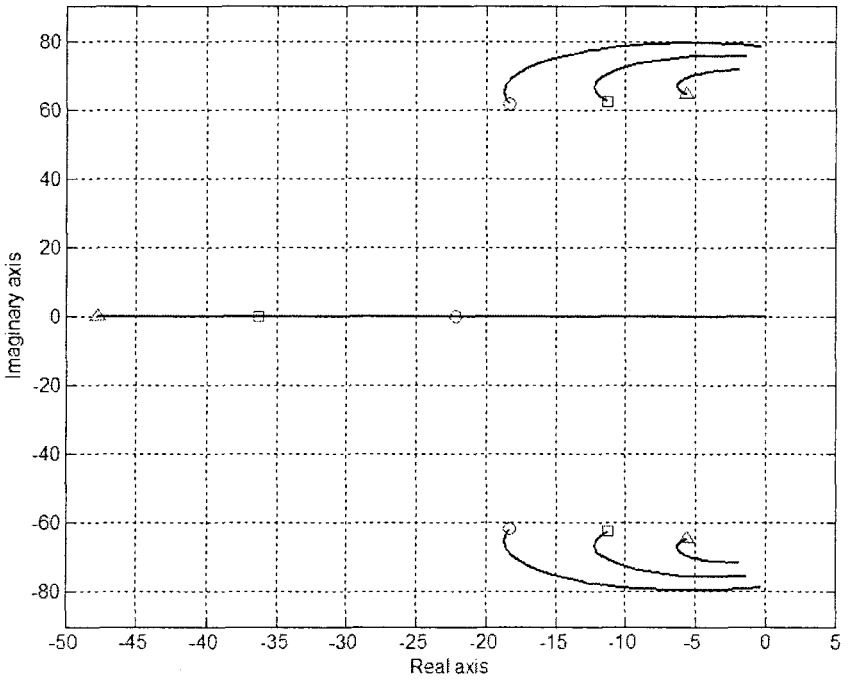

Figure 4.11. Root loci of the closed-loop system with the PPF (Set two when τ is increased from 0 to 0.03 second) $K_P = -300$ (triangle); $K_P = -600$ (square); $K_P = -900$ (circle).

The system poles consist of a pair of complex conjugates and a real number. Similar to the case of the direct position feedback, the equivalent natural frequency and damping ratio are defined based on the complex conjugate poles. It is informative to observe how the gain-delay combinations affect the variation of the equivalent natural frequency and damping ratio. For this purpose only results of Set two will be shown, although similar patterns exist for Set one. This can be observed for the NPF in Figure 4.12 where the equivalent natural frequencies as a function of the gain for four time delays are shown. It can be seen that, with an increase in the gain the equivalent natural frequencies increase when $\tau = 0.06$ and $\tau = 0.07$ second but decrease when $\tau = 0.04$ and $\tau = 0.05$ second. Figure 4.13 shows the cases for the PPF case. For a very small delay time, the equivalent natural frequency decreases first and increases after the gain magnitude reaches a certain value. When the delay is sufficiently large, the equivalent natural frequency increases with an increase in the gain magnitude.

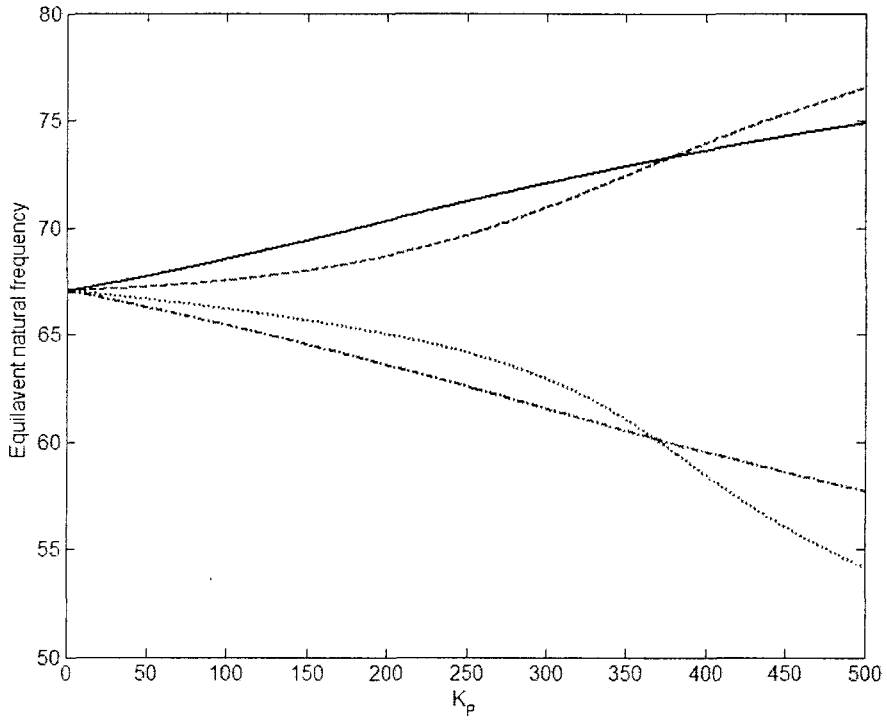

Figure 4.12. Equivalent natural frequencies of the NPF closed-loop system, (Set two) $\tau = 0.04$ (dashed-dotted line); $\tau = 0.05$ (dotted line); $\tau = 0.06$ (dashed); $\tau = 0.07$ (solid line).

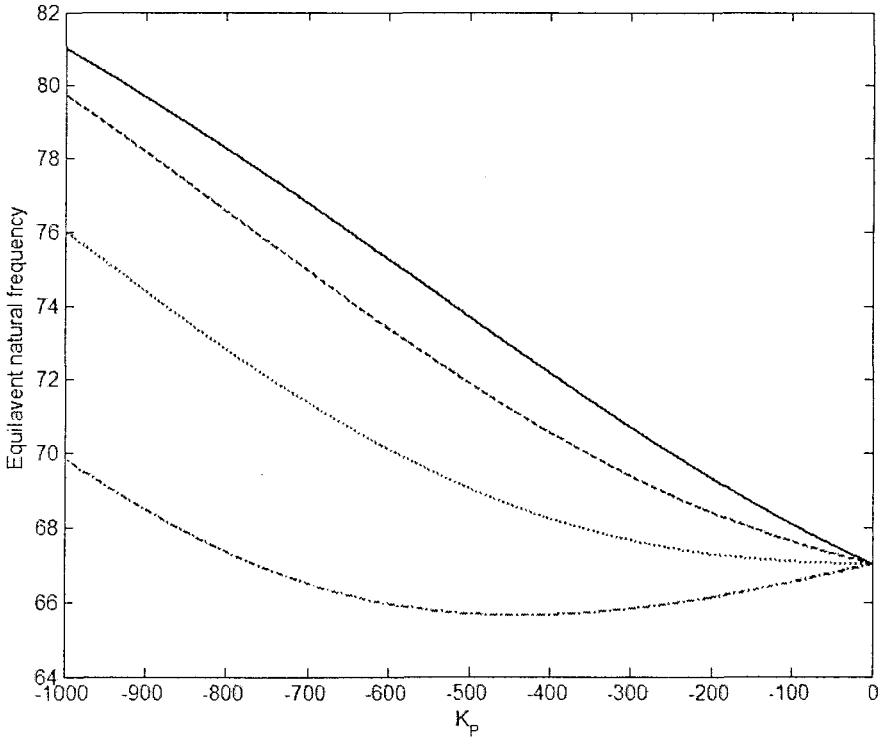

Figure 4.13. Equivalent natural frequencies of the PPF closed-loop system, (Set two) $\tau = 0.005$ (dashed-dotted line); $\tau = 0.01$ (dotted line); $\tau = 0.015$ (dashed line); $\tau = 0.02$ (solid line).

The equivalent damping ratio can be used to measure the active damping introduced by the delayed feedback control. How the gain-delay combinations affect the active damping can be illustrated by superimposing the damping contours on the stability chart. This can be observed in Figures 4.14 and 4.15 for Set one and in Figures 4.16 and 4.17 for to Set two . Each of the contour levels within the stable region represents the gain-delay combinations that result in the same level of the equivalent damping ratio. The darkness of the shaded regions is used to indicate the level of the active damping: the darker the shaded region, the higher the active damping. Interestingly, for the NPF, there exists a preferred time delay that yields the largest damping ratio, indicated by the darker vertical region in Figures 4.14 and 4.16. This preferred time delays are about $\tau = 0.044$ seconds for Set one, and $\tau = 0.053$ seconds for Set two. These time delays are close to half of the natural period of the system $T = 0.094$ seconds. A close observation of pole progression indicates that when the time delay reaches this value, there is a sudden change in the direction under which the complex system poles progress. An example of this occurring can be seen in Figure 4.18. The non-system poles in the figure progress from left to right. The root progressions are shown for three different time delays while varying the gain from 0 to 500. The sudden flip in direction seen between the system poles and non-system poles occur at the preferred time delay. This can be observed in analyzing the progression of the roots for $\tau = 0.0525$ and for $\tau = 0.053$ in Figure 4.18. This phenomenon does not exist in the case of the PPF. As shown in Figures 4.15 and 4.17, for the PPF case the greater the gain magnitude and the smaller the time delay, the higher the active damping. In regards to the active damping tendencies, Sets one and two behave in a similar fashion for both NPF and PPF.

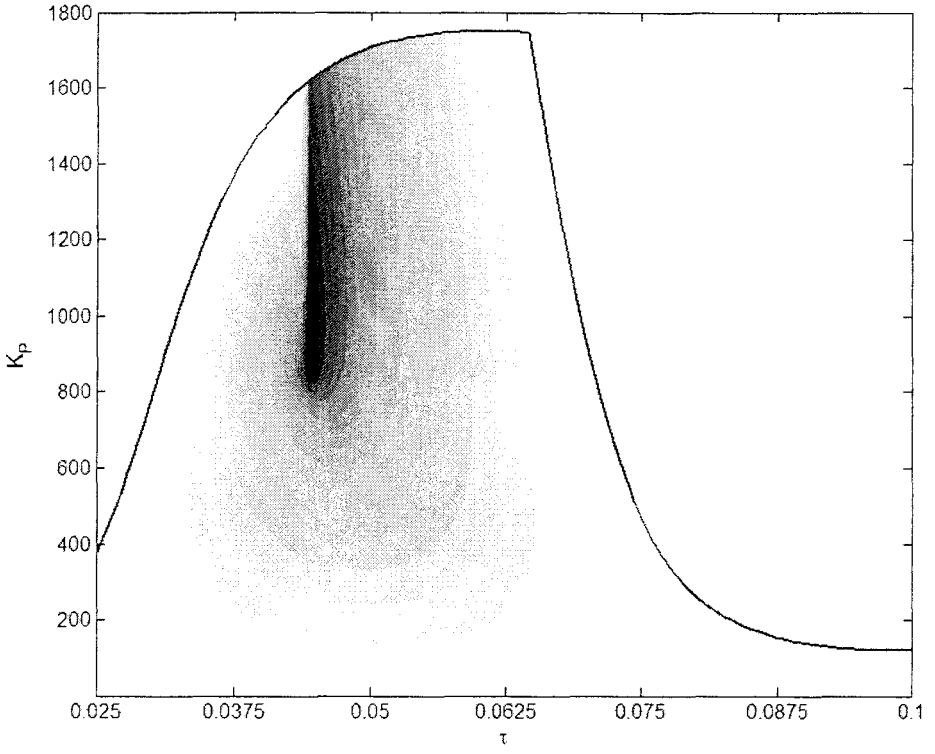

Figure 4.14 : Gain delay stability chart for the NPF, with damping contours, (Set one) Darker shade corresponds to higher active damping

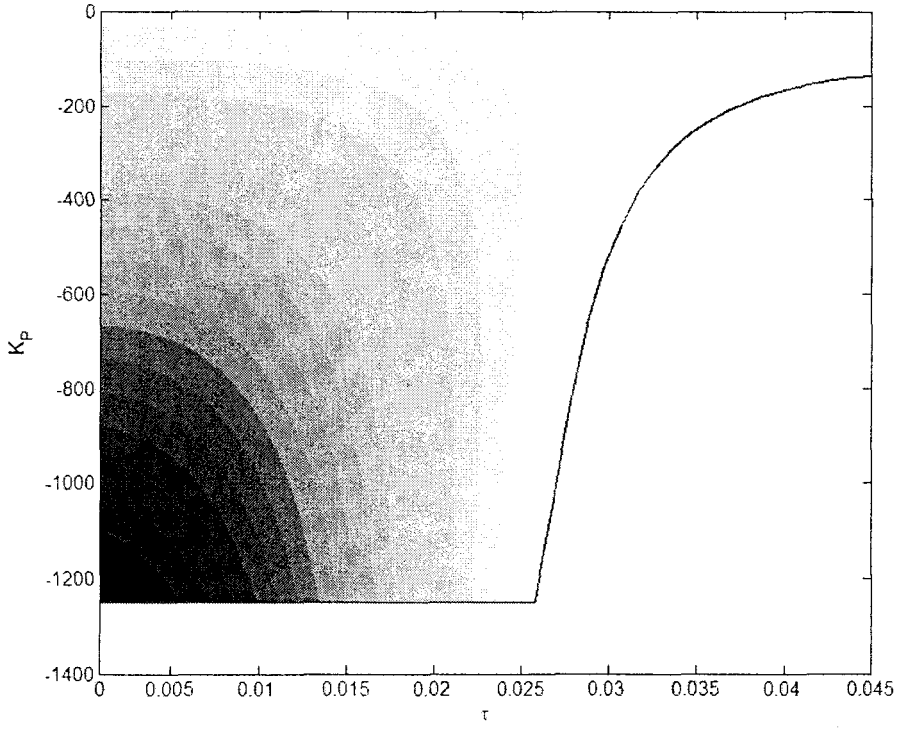

Figure 4.15: Gain-delay stability chart for the PPF, with damping contours, (Set one) Darker shade corresponds to higher active damping

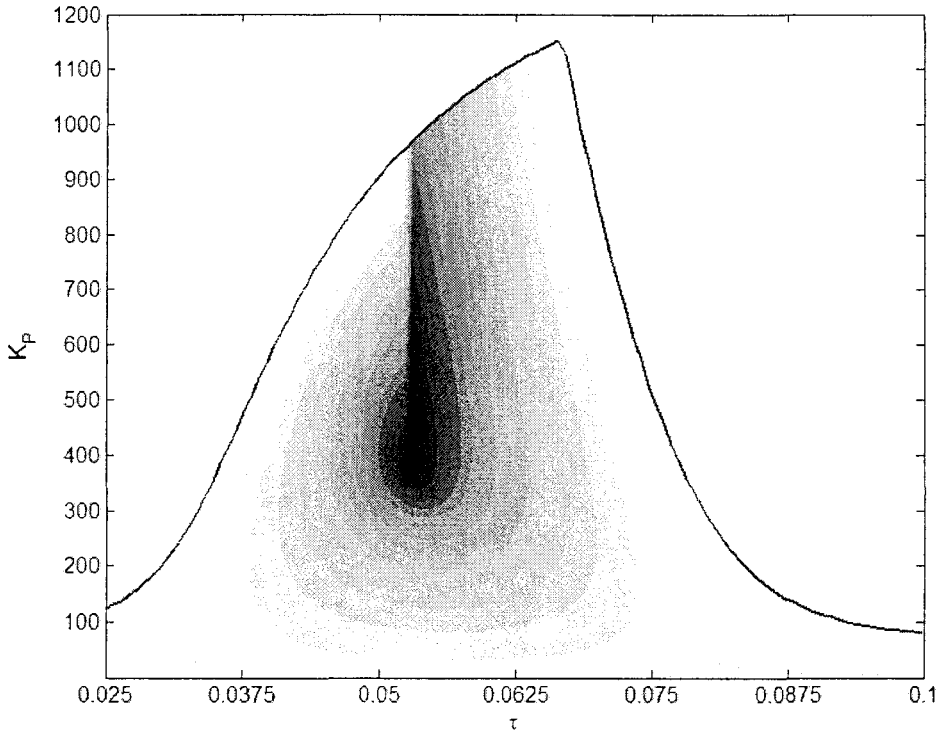

Figure 4.16: Gain-delay stability chart for the NPF, with damping contours, (Set two) Darker shade corresponds to higher active damping.

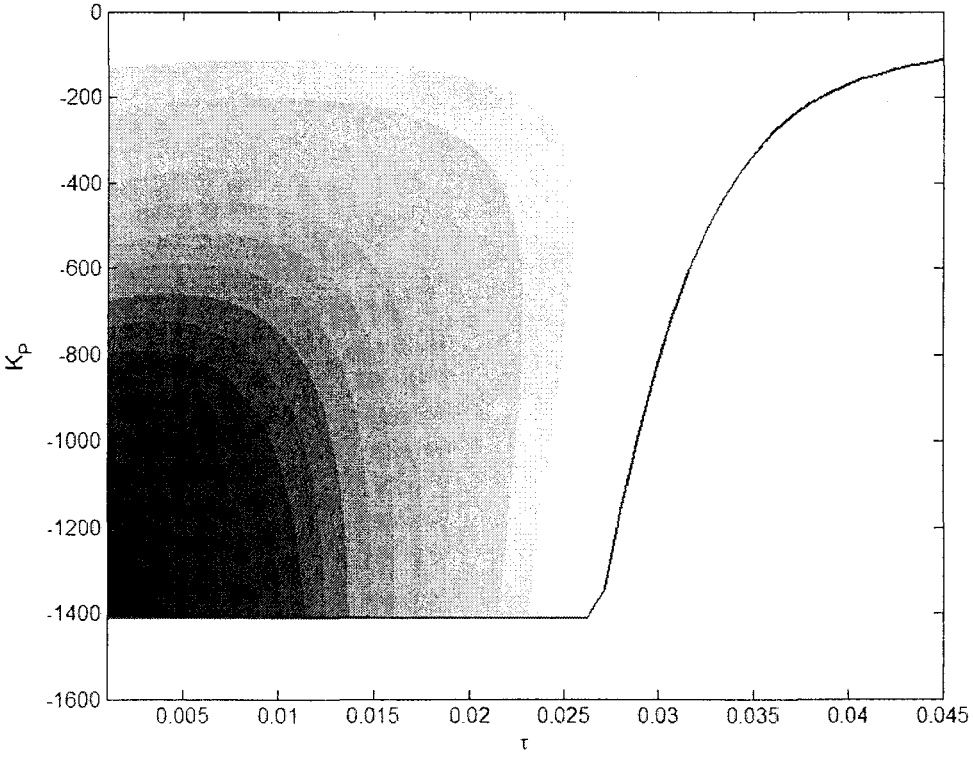

Figure 4.17: Gain-delay stability chart for the PPF, with damping contours, (Set two) Darker shade corresponds to higher active damping

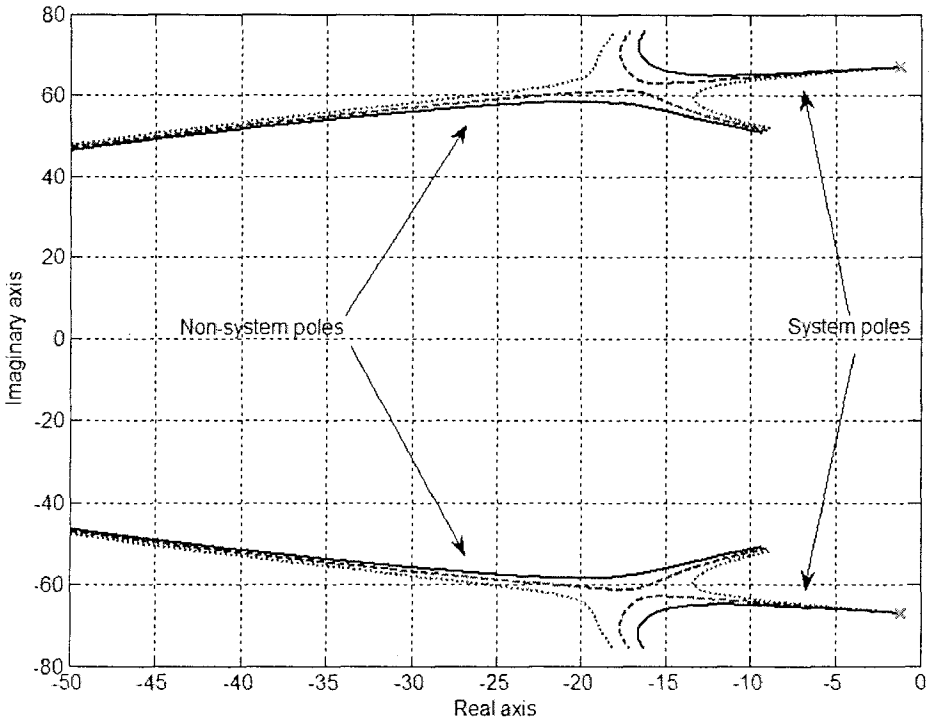

Figure 4.18: Interaction of system poles with non-system poles, (Set two) $\tau = 0.0535$ (solid), $\tau = 0.053$ (dashed), $\tau = 0.0525$ (dotted)

4.4. Controller Design for Active Isolation

In this section the optimal delayed feedback controller design is investigated. The objective is to find optimum delay time and feedback gain so as to improve the performance of active isolation systems. To date, most existing studies dealing with time delay control mainly focus on active vibration suppression [32, 40-43], as opposed to vibration isolation. In this work it is shown that in the realm of active vibration isolation, the optimum delayed controllers have some unique characteristics. Both the APF and RPF are studied. For each case, both the NPF and the PPF are considered. The performance of a vibration isolator is commonly measured by the displacement transmissibility (TR). The TR for a delayed feedback with the APF is given by

$$TR(\omega) = \left|\frac{X(\omega)}{Y(\omega)}\right| = \left|\frac{cLs^2 + (cR + kL + 2\gamma k_v)s + kR}{mLs^3 + (mR + cL)s^2 + (cR + kL + 2\gamma k_v)s + kR + 2\gamma K_p e^{-\tau s}}\right|_{s=j\omega} \tag{4.15}$$

whereas the TR for a delayed feedback with the RPF is given by

$$TR(\omega)=\left|\frac{X(\omega)}{Y(\omega)}\right|=\left|\frac{cLs^2+(cR+kL+2\gamma k_v)s+kR+2\gamma K_p e^{-\tau s}}{mLs^3+(mR+cL)s^2+(cR+kL+2\gamma k_v)s+kR+2\gamma K_p e^{-\tau s}}\right|_{s=j\omega} \tag{4.16}$$

where $X(\omega)$ is the amplitude of the steady-state response of the mass and $Y(\omega)$ is the amplitude of the harmornic base excitation.

Typically, active isolation control intends to achieve two objectives: to minimize the TRs over a given frequency range and to minimize the largest TR. These two objectives can be combined as a single objective function defined by

$$f = w_1 \|TR(\omega)\|_2 + w_2 \|TR(\omega)\|_\infty \text{ in the frequency range } 0 \le \omega \le \omega_u$$

where $\|\bullet\|_2$ denotes the second norm, $\|\bullet\|_\infty$ denotes the infinity norm and ω_u is a prescribed upper bound for the frequency of interest, w_1 and w_2 are weights used to impose different emphasis on each of the parts of the objective function. A constraint optimization can be formulated as follows:

$$\text{Minimize} f(K_p, \tau) \text{ over the frequency range } 0 \le \omega \le \omega_u$$

subject to the following constraints, in a similar fashon to those in chapter 3

1. the poles of the closed-loop system must be on the LHP and away from the imaginary axis by at least a specified stability margin σ, and
2. $K_{pl} \le K_p \le K_{pu}$, $\tau_l \le \tau \le \tau_u$

where K_{pl}, τ_l and K_{pu}, τ_u are the lower bounds and the upper bounds of the parameters, respectively. The frequency upper bound was prescibed to be $\omega_u = 200$ rad/s. The stability margin was set to be $\sigma = -5$. The weights were chosen to be $w_1 = 0.1$ and $w_2 = 10$ after many trials. This combination achieved a reasonable comprimize between minimizing the 2nd norm and the infinity norm. The sequential simplex algorithm was used in the numerical solution. An initial feasible simplex was randomly generated within the given parameter bounds. To ensure the convergence of the numerical optimization, solutions for each of the controller cases were repeated a number of times.

Table 4.1. Optimal results for the NPF controllers (Set one)

Controller	τ^* (second)	K_p^* (v/m)	σ	$\|TR\|_2$	$\|TR\|_\infty$
APF	0.0519	992.27	-9.9327	26.7771	3.8596
RPF	0.0489	1157.21	-6.9088	23.7971	3.3304

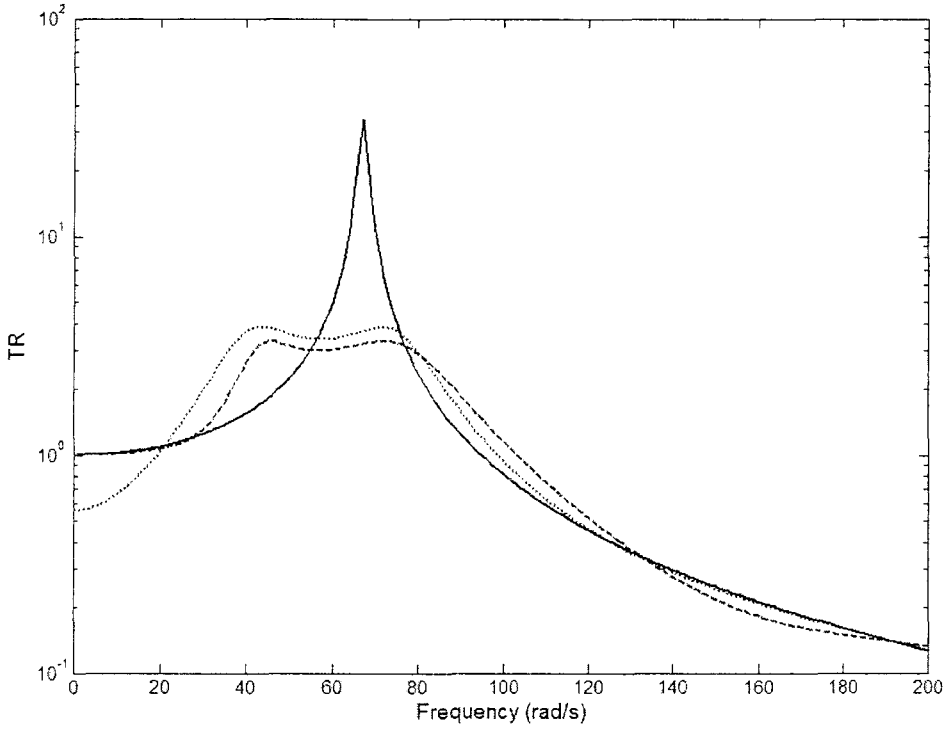

Figure 4.19. TRs (Set one): the open-loop system (solid line); the optimum APF (dotted line); the optimum RPF (dashed line).

4.4.1. Negative Position Feedback (NPF)

For the NPF, the parameter bounds were set to be $K_{pl} = 0$, $K_{pu} = 5000$, $\tau_l = 0$, and $\tau_u = 0.2$, respectively. Table 4.1 lists the optimum parameters that were obtained repeatedly by a number of the solutions for Set one, while those of Set two are listed in Table 4.2. Figures 4.19 and 4.20 compare the TR of the open-loop and the TRs of the closed-loop system with the optimum controllers for Set one and Set two respectively. Observing the results, one can firstly note that the gain-delay combinations lie in the first lobe on the positive K_p side as seen in

Figures 4.6 and 4.7. That is, the delay is between the bounds $0.03 < \tau < 0.07$ and the gain is below the upper limits for stability. Secondly, a slight degradation in the transmissibility when compared to the passive system is seen in a small region below the open-loop resonance frequency for both the APF and RPF and for both Sets. Thirdly, attenuation at the resonance frequency is attained by both the APF results and the RPF results without degradation of the high-frequency performance of the passive isolator. Fourthly, the RPF outperforms the APF in the mid to high frequency regions while the APF performs more favourably in the low frequency range. Notably, a purposefully injected time delay can significantly improve the isolation characteristics of the NPF with very similar results attained for both Sets. Figures 4.21 and 4.22 compare the TRs of the open-loop system and the TRs of the closed-loop system with the gain and delay chosen at the point of maximum active damping, i.e., the darkest shaded point on Figure 4.14 for Set one and Figure 4.16 for Set two. In this case the time delay and gain are $\tau = 0.044$ second and $K_P = 891$ v/m for Set one and $\tau = 0.053$ second and $K_P = 364$ v/m for Set two, respectively. Evidently, the transmissibility ratios obtained using the optimum parameters are superior to those using the points of highest active damping. This can be partly attributed to the larger proportional gain which imposes more active energy onto the system.

Table 4.2. Optimal results for the NPF controllers (Set two)

Controller	τ^* (second)	K_p^* (v/m)	σ	$\|TR\|_2$	$\|TR\|_\infty$
APF	0.0585	522.35	-10.0232	26.5465	3.933
RPF	0.0557	604.16	-7.1453	24.6674	3.565

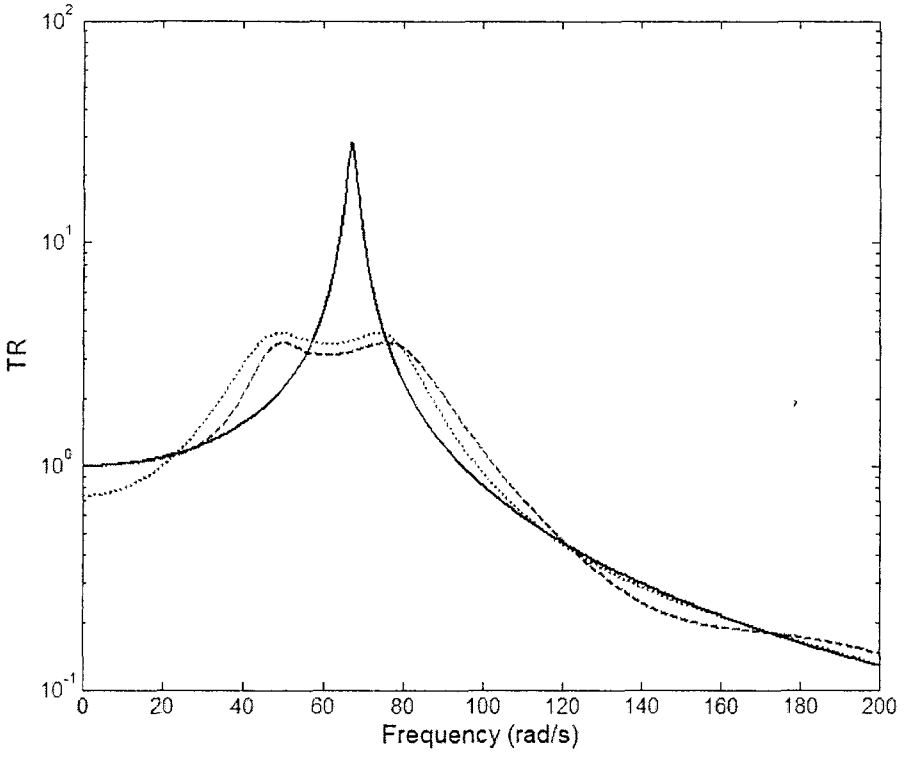

Figure 4.20. TRs (Set two): the open-loop system (solid line); the optimum APF (dotted line); the optimum RPF (dashed line).

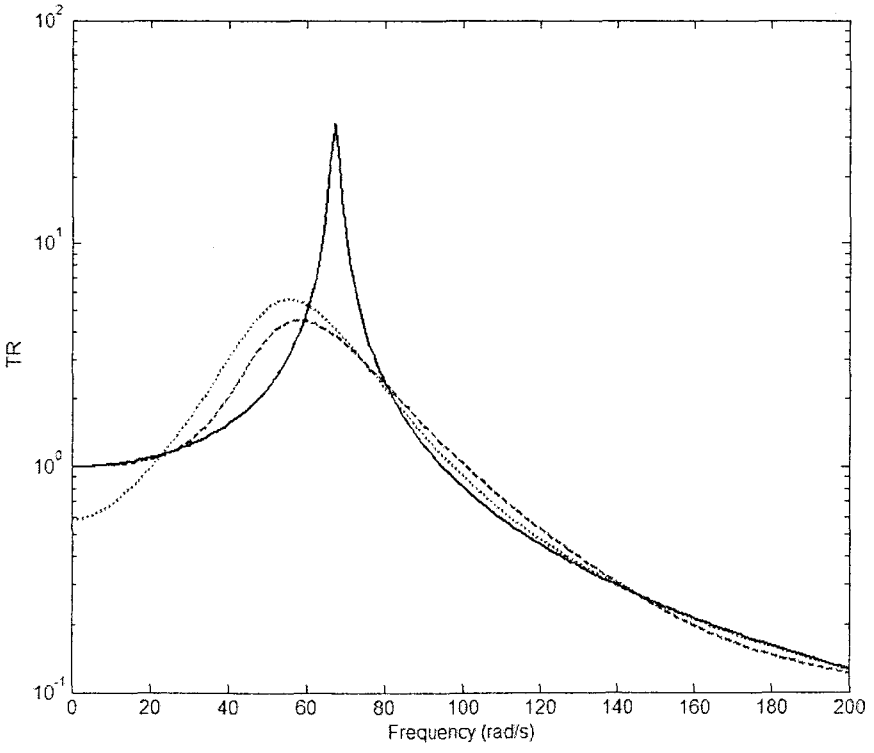

Figure 4.21. TRs (Set one): the open-loop system (solid line); the APF with the highest active damping (dotted line); the RPF with the highest active damping (dashed line).

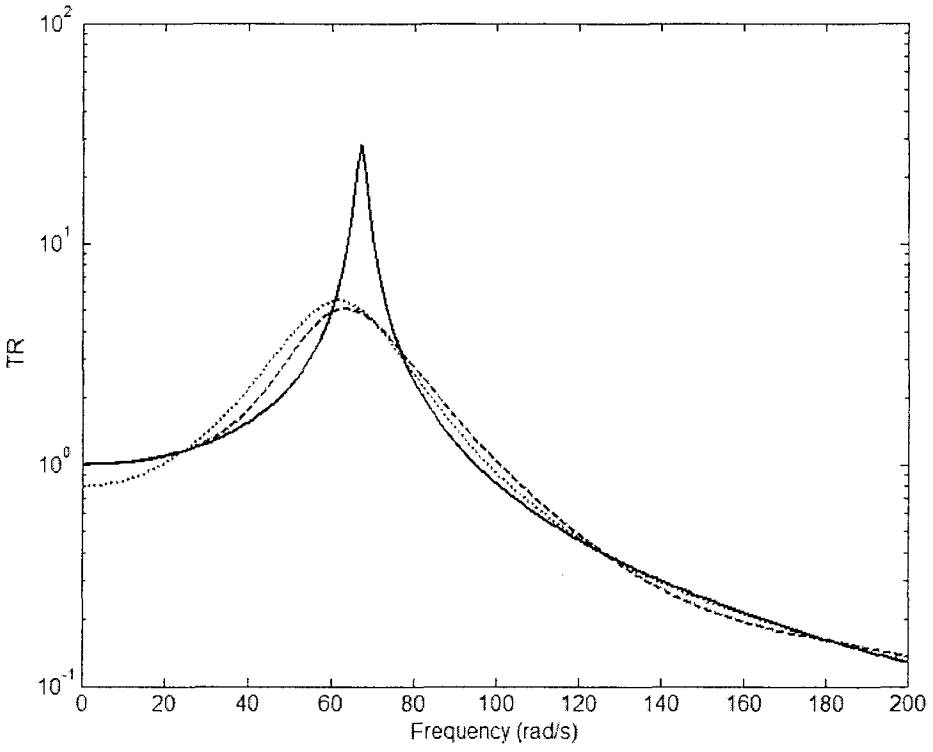

Figure 4.22. TRs (Set two): the open-loop system (solid line); the APF with the highest active damping (dotted line); the RPF with the highest active damping (dashed line).

4.4.2. Positive Position Feedback (PPF)

For the PPF, the parameter bounds were set to be $K_{pl} = -5000$, $K_{pu} = 0$, $\tau_l = 0$, and $\tau_u = 0.1$, respectively. Table 4.3 and 4.4 lists the optimum parameters that were obtained repeatedly by a number of the solutions for Set one and Set two respectively. Figure 4.24 compares the TRs for Set two. There are a few important observations. In general, one can see that the results for the RPF case is superior to that of the APF. The APF is detrimental to the vibration isolation system in the low frequency range, while satisfactory results are attained in the mid to high frequency ranges. However, for the RPF case the optimal time delay converged to zero, or near zero. This demands further investigation. For this purpose, two more cases are presented. In the first case, the lower bound for the gain is increased to $K_{pl} = -800$. Now the optimum delay is converged to a non-zero value with the larger stability margin as given in Table 4.4. This indicates that when the permissible gain magnitude is not high enough, a time delay is required in order to achieve better performance. In the second case, the PPF is applied to the fundamental system defined by equation (4.6). As indicated in Table 4.4, for the APF, the

optimum delay converged to a larger value while for the RPF, it converged to a value that is much smaller than the time constant of the actuator. This suggests that the inherent time delay due to the actuator dynamics of Set two is sufficient and any intentionally added delay will not further minimize the objective function. This finding agrees with the result shown in Section 4.2. This feature makes it possible to realize a delayed positive proportional feedback by properly choosing an actuator time constant. For example, the larger time constant inherent to Set one would not be a good choice compared to Set two when using PPF. The results for the optimization procedure can be seen in Figure 4.23 and are tabulated in Table 4.3. Evidently, the larger inherent lag in Set one makes it impossible for the system with PPF to perform as well as with Set two. This further supports the notion that an inherent lag within the system can be utilized to yield optimal isolation when using a relative PPF; however there are limits to the magnitude of the lag.

Table 4.3. Optimal results for the PPF controllers; Set one ($T_a = 0.0464$)

Controller	τ^* (sec)	K_p^* (v/m)	σ	$\|TR\|_2$	$\|TR\|_\infty$
APF	0.0040	-930.8762	-5.1302	23.2319	3.9363
RPF	0	-950.554	-5.1223	20.0060	3.7884

Table 4.4. Optimal results for the PPF controllers; Set two ($T_a = 0.0174$)

Controller	τ^* (sec)	K_p^* (v/m)	σ	$\|TR\|_2$	$\|TR\|_\infty$
APF	0.0120	-837.11	-17.5092	19.752	2.474
RPF	0.0	-1208.58	-8.7043	12.441	1.531
RPF	0.0035	-800.00	-25.6928	16.442	2.418
Fundamental system with APF	0.02450	-689.34	-42.9649	18.597	1.957
Fundamental system with RPF	0.00290	-1393.57	-7.261	5.304	1.158

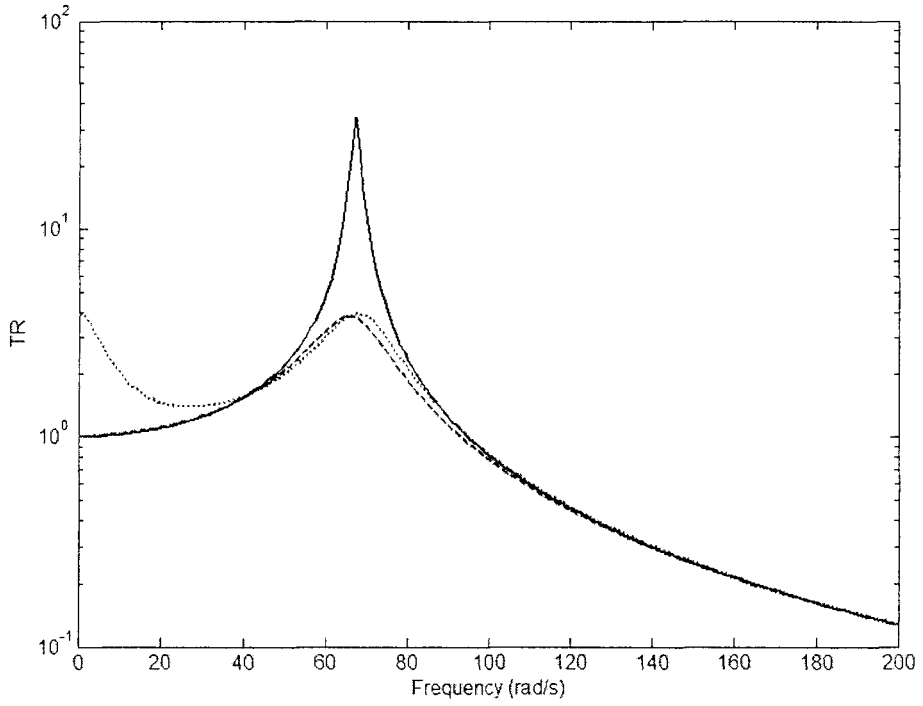

Figure 4.23.TRs: the open-loop system (solid line); the optimal APF (dotted line); the optimal RPF (dashed line);

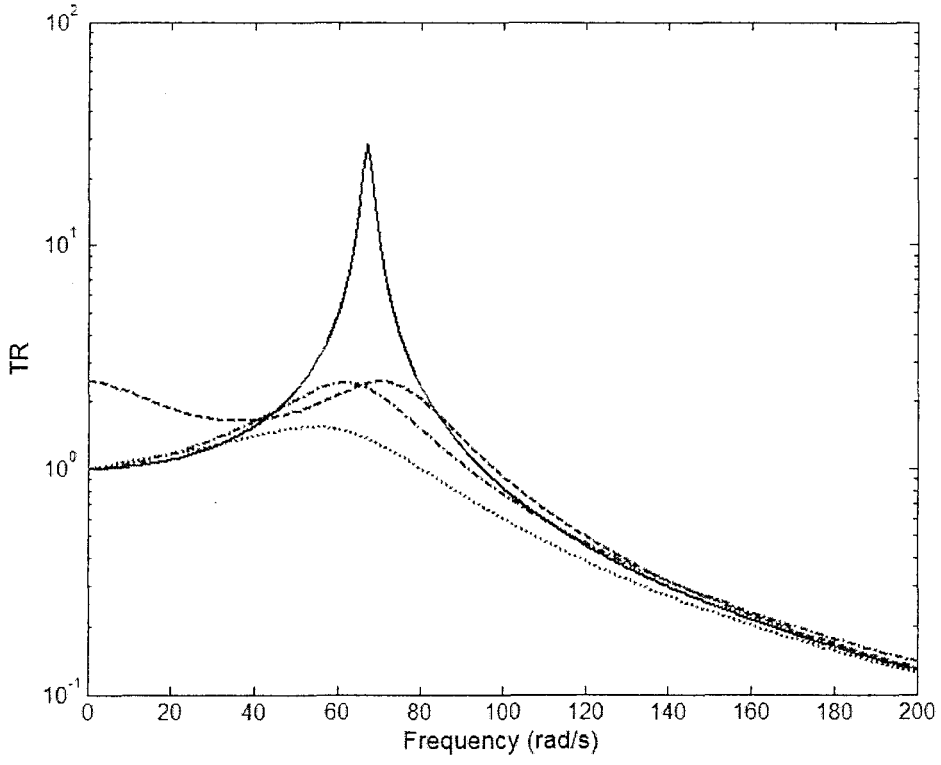

Figure 4.24. TRs: the open-loop system (solid line); the optimal APF (dashed line); the optimal RPF (dotted line); the optimal RPF obtained with $K_{pl} = -800$ (dash-dotted line).

4.5. Experiment and Results

In this section the controllers discussed previously are applied in real time to the proposed active vibration isolator. Only Set two was used to validate the results attained in previous sections. Numerous experiments were conducted which also served as a real time performance measure. In what follows, only the results using three controllers that were based on the RPF are reported. The three controllers are referred to as controller 1, 2, and 3 respectively and their parameters are repeated in Table 4.5.

Figure 4.25 shows a photograph of the experimental setup. A personal computer equipped with a data acquisition (DAQ) board (dSpace 1104) was used to collect signals and to generate exciting signals and control inputs. Simulink was used in conjunction with dSpace Control Desk software in order to implement the control. A laser position sensor (Wenglor, CP24MHT80) was fastened to the base to measure the relative displacement of the mass, while a shaker (Brüel & Kjær, 4809) was used to excite the base. The built in anti aliasing filter of the laser position sensor was utilized in experiment. The cut-off frequency was at least 10 times larger than the natural frequency of the system. Accordingly, any phase difference caused by filtering the position signal was assumed to be negligible. A sampling frequency of 1000 Hz was used. In order to test the isolator performance over the entire frequency range of interest, the base was subjected to a sinusoidal excitation with the frequency increasing linearly with time. For all of the cases, the linearly varying frequency was initiated at 20 rad/s, ending at 120 rad/s over a duration of 50 seconds.

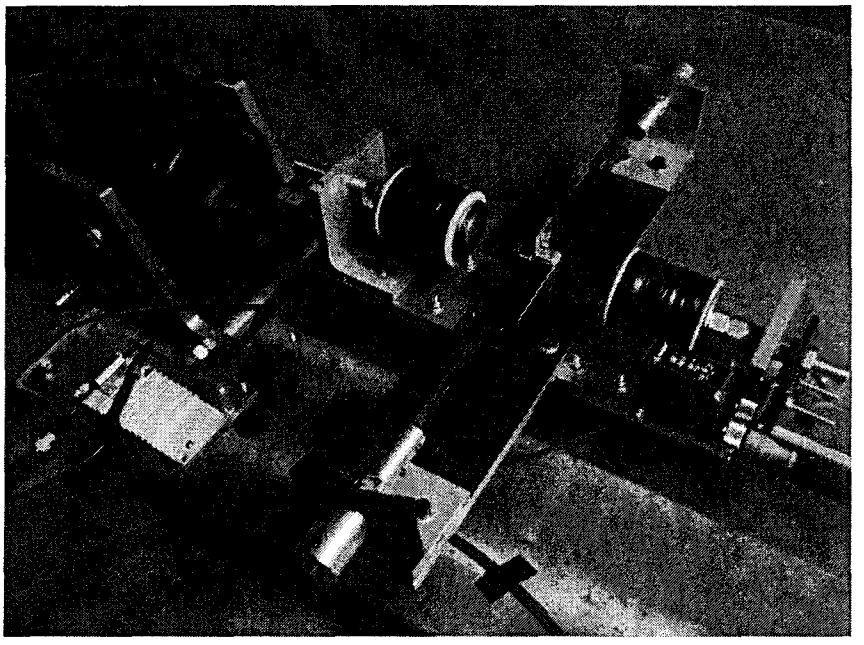

Figure 4.25. Photograph of the experimental setup of the proposed active isolator

Table 4.5. Controllers used in experiment

Controller Type	Number	τ (sec)	K_p (v/m)
NPF	1	0.0557	604.16
PPF	2	0.0035	-800.00
PPF	3	0	-1208.58

Figure 4.26 shows the experimental results using controller 1. It is observed that in the lower frequency range the controller had a negligible effect on the response of the system despite the control effort applied. Moving to the mid frequency range which corresponded to the section in between 15 and 30 seconds it is seen that the response of the controlled system is suppressed effectively, notwithstanding a significant drop in control effort in the 25 to 30 second region. In this region the open-loop system response kept growing until resonance was passed. In the higher frequency range it can be seen that both the controlled and the uncontrolled responses followed a very similar trend. Figures 4.27 and 4.28 show the results with the delayed positive position feedback, the results for the PPF responded better for the entire frequency band. Controller 3 performed better than controller 2, although it required a larger control effort and thus more energy input onto the system.

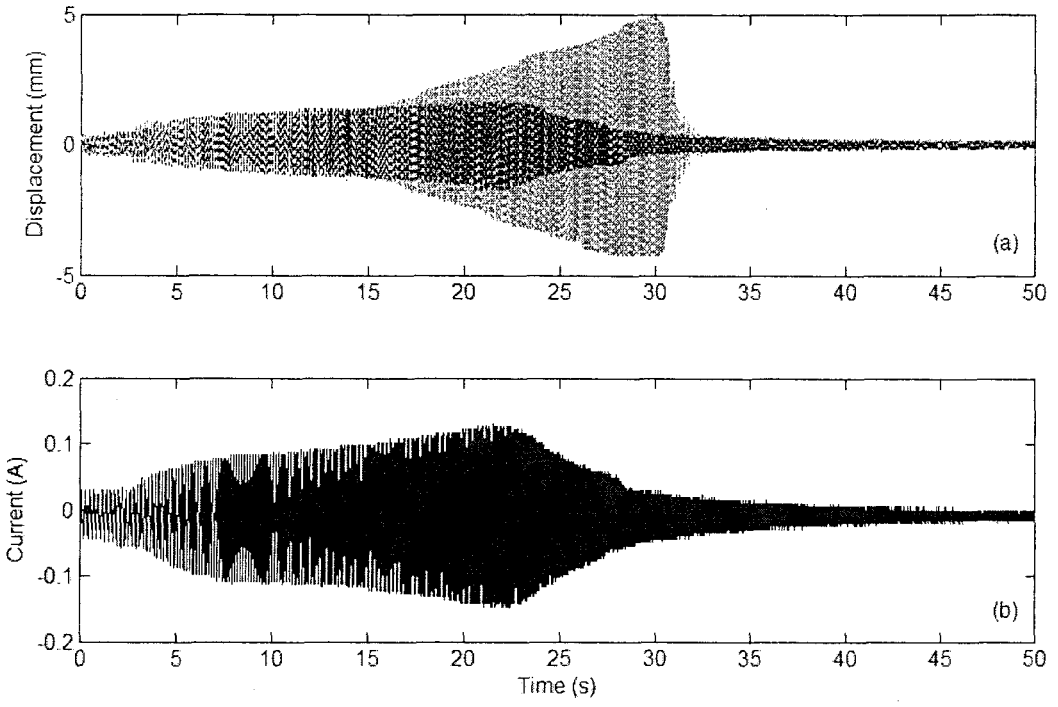

Figure 4.26. Experimental results with Controller 1: (a) relative displacement of the mass without control (dashed line); with control (solid line); (b) current of the actuator.

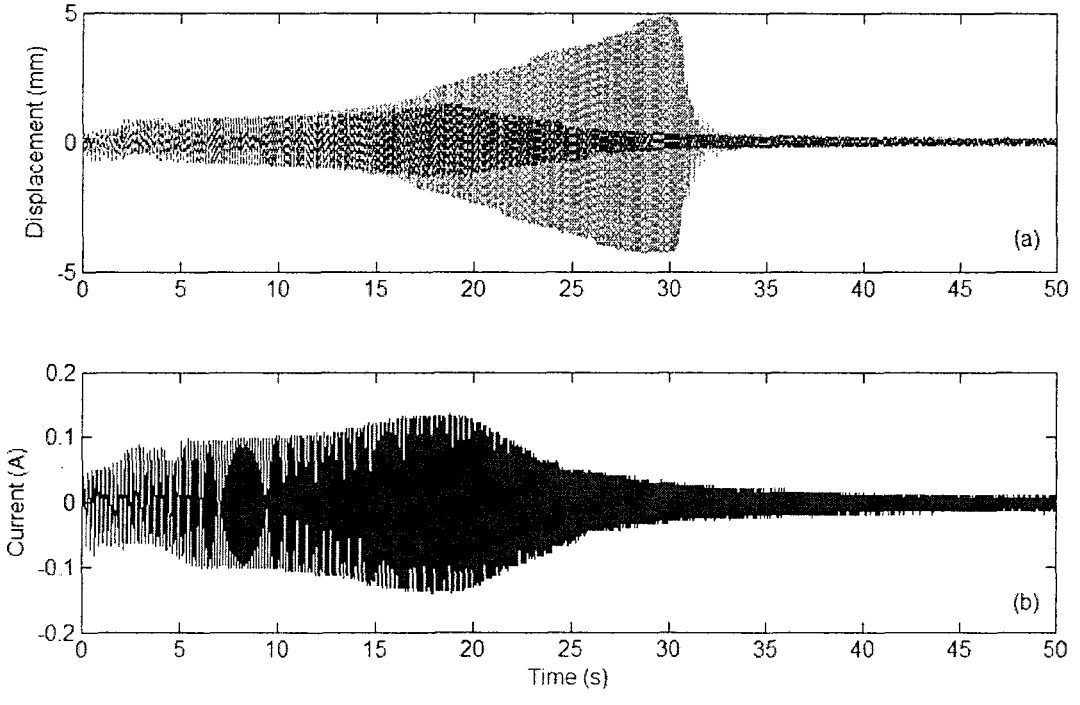

Figure 4.27. Experimental results with Controller 2: (a) relative displacement of the mass without control (dashed line); with control (solid line); (b) current of the actuator.

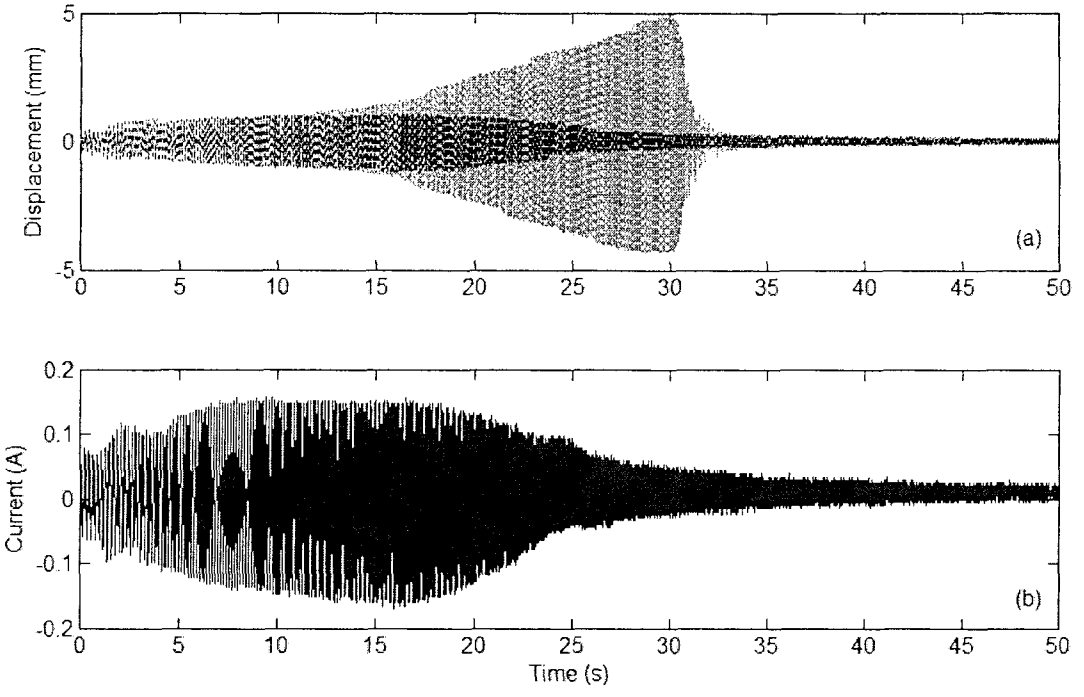

Figure 4.28. Experimental results with Controller 3: (a) relative displacement of the mass without control (dashed line); with control (solid line); (b) current of the actuator.

In order to better measure the performance of the systems, the integral of the squared response (ISR) [48] was computed. Figure 4.29 compares the ISR values for the four cases considered above. While all the three controllers significantly reduce the ISR values, at the end of 50 seconds controller 3 gave the smallest ISR value. It is noted that controller 2 only lags in the ISR value to controller 3 by about a factor of 1.2. To take into account the control effort required, the integral of the squared control current (ISCC) is computed. Figure 4.30 compares the ISCC values for the three controllers. Firstly, it is evident that controller 3 had the largest ISCC value at the end of 50 seconds, thus validating the use of more energy than the other 2 controllers. Controller 2 gave the smallest ISCC value at the end of 50 seconds, indicating the least energy consumption. The ISCC value of controller 1 is greater than that of controller 2 by a factor of 0.63. When both the ISR and ISCC values are considered, control 2 outperforms controllers 1 and 3 as it effectively isolate the base motion with the minimum energy consumption.

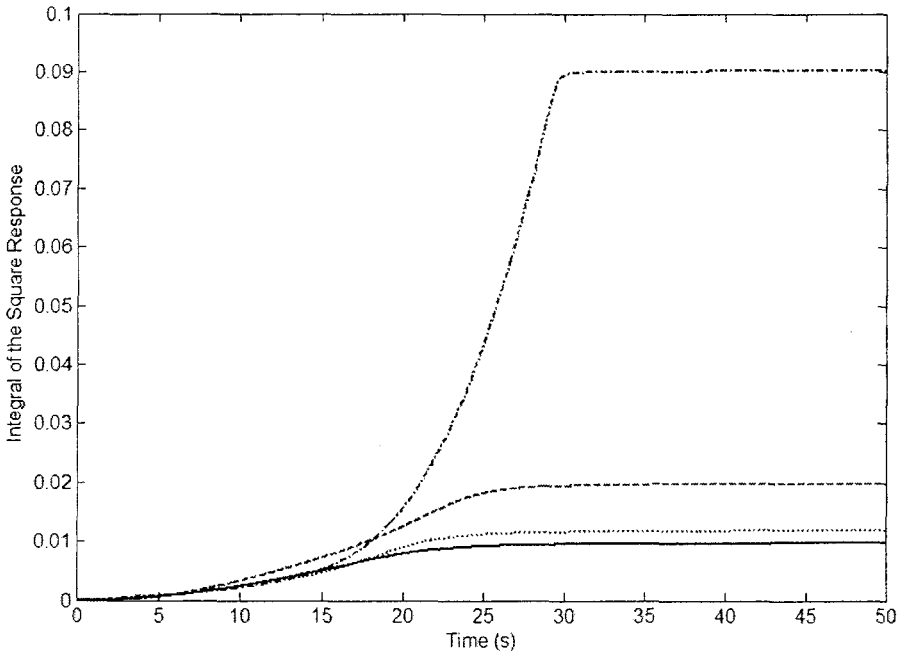

Figure 4.29. ISR values: Open-loop (dash-dotted line);controller 1 (dashed line); controller 2 (dotted line); controller 3 (solid line).

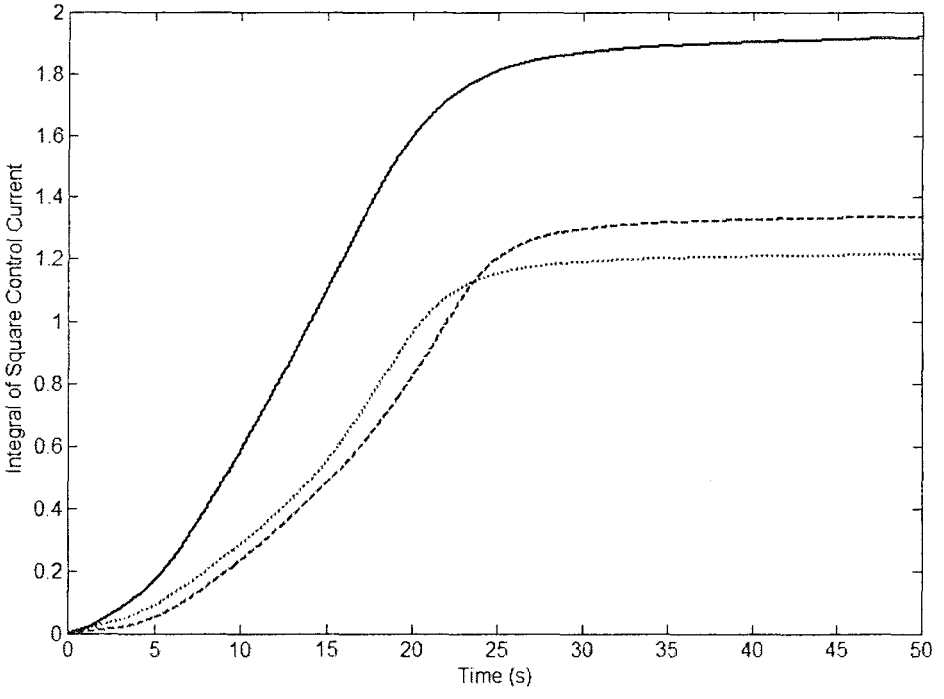

Figure 4.30. ISCC values: controller 1 (dashed line); controller 2 (dotted line); controller 3 (solid line).

4.6. Conclusion

Time delayed control of the proposed active vibration isolator has been investigated in this chapter, with a focus on finding effective controllers using only position feedback signals taking direct advantage of inherent time delays, as well as investigating purposefully injected time delays. The following conclusions are found applicable to both Sets. First a direct position feedback was considered. Three main findings have been obtained: (1) A negative direct feedback is unacceptable as it has a very narrow stability margin due to the inherent time delay caused by the actuator dynamics. (2) A positive direct feedback offers an improved transmissibility ratio when a relative position feedback is used and an unsatisfactory transmissibility ratio when an absolute position feedback is used. (3) An inherent time delay with an appropriate magnitude compared to the natural period of the system is advantageous for a positive relative position feedback. Second, a stability analysis of a time delayed position feedback has been conducted with two main conclusions. (1) A delayed feedback can improve the stability of the closed-loop system for both the negative and positive position feedbacks. (2) For the negative position feedback the active damping level introduced by the delayed feedback is maximized when the delay time is around half of the natural period of the system, depending on the magnitude of the inherent lag. For the positive position feedback, the active damping is maximized when the gain magnitude is largest and the time delay is zero. Third, an optimum controller design procedure has been presented. The main observations are as follows. (1) For a negative position feedback, both the optimum delayed absolute position feedback and relative position feedback controllers offer a similar performance. (2) For the positive position feedback, the best controller is the one with the relative position feedback and zero time delay. This finding reinforces the conclusion from the study of the direct positive relative position feedback: the inherent time delay of the actuator makes an intentionally added time delay unnecessary. Finally an experiment has been implemented to validate the analytical and numerical studies. It has been found that among the three controllers tested, controller 2 offers the best combination of effective base isolation and reasonable control effort.

Is should be noted that although the study has been based on a particular active vibration isolator, the findings are applicable for similar systems. From a practical standpoint, active isolation controllers such as the ones presented herein constitute minor modifications to existing

controllers. Thus, utilization of such methodologies for active isolation systems can be very economical.

CHAPTER 5 –ADAPTIVE BACKSTEPPING CONTROL

The main purpose of this chapter is to investigate the adaptive control of the base isolation system in real time considering some of its parameters uncertain. Section 5.1 introduces the section and provides a review of related research. In section 5.2 the formulation of the control problem is presented and an adaptive controller based on the backstepping technique is proposed. Subsequently, in section 5.3 the implementation in real-time is discussed and the proposed controller is compared with that of a directly related controller. Finally, the conclusions of this chapter are given in section 5.4.

5.1. Introduction

Active isolation has received much attention because of its feedback control feature [54], in which a signal or signals sent back to a predetermined controller can provide superior performance over conventional passive vibration isolators. This is generally performed through the use of traditional control laws. The majority of these active control laws require detailed prior knowledge of the system parameters which results in a control law with parameters that are specific to the system at hand. Example studies not particular to an application can be found in [55-57]. On the other hand, most models of real physical systems usually contain different types of uncertainties [58]. These uncertainties are typically due to un-modelled dynamics, bad knowledge of parameter values, and time varying parameters. If a traditional constant parameter control law is used on a real system that posse's uncertainties and/or time varying parameters, significant performance degradation can occur.

In addition to not requiring prior knowledge of the system parameters, adaptive control functions well in systems with nonlinearities and time-varying parameters [59]. Some notable studies are [54, 60-62]. In [58] a unique adaptive control scheme for a class of 2^{nd} order systems was presented. A key feature in this study was that the closed loop transient and asymptotic performances could be tuned explicitly with the design parameters. However, this naturally came with a trade off between good performance and reasonable control effort. Recently, in a study reported in [63] some extensive challenges in adaptive control were identified. One key issue noted when using adaptive control was that it is always better to use an accurate model than not to do so – and if there is a time delay present and it is neglected, a control algorithm is more likely to fall over. In this chapter, this issue is being further investigated and it is shown that if the adaptive controller does not fall over, performance degradation is likely to occur.

Differing from the previous chapters in this thesis, the studied active isolator being investigated is now considered uncertain and an adaptive control scheme is proposed. Also the current study differs from previously studied works in a few main areas. The main contribution for the controller proposed by [58] was that transient and asymptotic performances depended explicitly on the design parameters. Other backstepping methods do not contain this feature. The proposed control scheme unlike the one in [58] will take into account the actuator physics. This complicates the control law and resulted in a controller not realized before. The scheme also avoided the unwanted overparameterization issue. Secondly, this study examines the function of the control schemes through experiments. This validates possible uses in practical applications.

In this chapter, the formulation of the control scheme is presented. Nonlinearities in the mechanical structure are now considered in the adaptive control law. Second, the implementation of the controller is described. Third, several results are presented, validating the controllers effectiveness. Fourth, the control scheme proposed by [58] is implemented by neglecting the actuator physics and the results for this controller are compared with the proposed controller. Increases in performance and parameter estimate accuracy increase is noted when using the proposed control scheme. This is attributed mainly to the inclusion of the actuator physics in controller design. Finally, conclusions are drawn for the section.

5.2. Nonlinear adaptive control formulation

The system described by (2.1) and (2.6) can be written in the form:

$$\begin{aligned} m\ddot{z} + c\dot{z} + f_s(z,t) &= -m\ddot{y} + \gamma i_a \\ L^*\dot{i}_a + R^* i_a + k_v \dot{z} &= e_c \end{aligned} \tag{5.1}$$

where $f_s(z,t) = f_b + f_{pc}$ presents the nonlinear restoring force, $R^* = R/2$, and $L^* = L/2$. From a previous study [21], the nonlinear restoring force can be approximated by an nth order polynomial with only odd terms, i.e.,

$$f_s(z,t) = \delta_1^* \frac{z}{d} + \delta_3^* \left(\frac{z}{d}\right)^3 + \delta_5^* \left(\frac{z}{d}\right)^5 + \cdots + \delta_n^* \left(\frac{z}{d}\right)^n + R_e(z,t) \tag{5.2}$$

where n is an odd number and $R_e(z,t)$ is a residual function. In the above polynomial, d is a known constant with the dimension of displacement. The coefficients δ_i^* are assumed to be unknown. The residual term $R_e(z,t)$ is unknown, but bounded. The damping coefficient c is assumed to be unknown as well. The control objective is to reduce vibration of the isolated mass subject to base disturbances in presence of system parameter uncertainty. For this purpose, an adaptive backstepping technique is employed. Although the following development is mainly inspired by the procedure reported in [58], there are some distinct differences.

Introducing the state variables $x_1 = z$, $x_2 = \dot{z}$, $x_3 = i$, and using equation (5.2), the system becomes as follows in state space form:

$$\begin{aligned} \dot{x}_1 &= x_2 \\ \dot{x}_2 &= \Phi(x_1, x_2)^T \Theta + R_e^*(x_1,t) - \ddot{y} + \gamma^* x_3 \\ \dot{x}_3 &= \frac{1}{L^*}\left(e_c - R^* x_3 - k_v x_2\right) \end{aligned} \tag{5.3}$$

where $\Phi(x_1,x_2) = -\left(\frac{x_2}{v}, \frac{x_1}{d}, \left(\frac{x_1}{d}\right)^3, ..., \left(\frac{x_1}{d}\right)^n\right)^T$ and $\Theta = \left(cv/m, \delta_1, \delta_3, ..., \delta_n\right)^T$ with $\delta_i = \delta_i^*/m$, $\gamma^* = \gamma/m$, $R_e^*(x_1,t) = R_e(x_1,t)/m$ and v is known a constant with the dimensions of velocity.

The following fundamental assumptions apply to complete the description:

Assumption 1:

The constant vector Θ is unknown but lies within a known sphere. That is $\|\Theta\| \leq M$ for a known positive constant *M*.

Assumption 2:

The function $R_R(x_1,t)$ is unknown but assumed to be locally Lipschitz and such that $|R_R(x_1,t)| \leq \bar{R}$ for all $x_1 \in \mathbb{R}$ and $t \geq 0$, where $\bar{R}$ is a positive constant.

Assumption 3:

The excitation acceleration signal $\ddot{y}(t)$ is unknown but bounded in the form $|\ddot{y}(t)| \leq E \ \ \forall \ t \geq 0$, where E is a known positive constant.

Assumption 4:

The initial parameter estimate vector $\hat{\Theta}_0$ is known to lie within the same sphere as in that of *assumption 1*. That is, $\|\hat{\Theta}_0\| \leq M$.

Adaptive control law:

$$e_c = \left(R^* - L^*C\right)x_3 + k_v x_2 - c_3 L^* z_3 - \gamma^* L^* z_2 - \frac{L^*}{\gamma^*}\left(\dot{z}_1 + \frac{d\left(\Phi^T\hat{\Theta}\right)}{dt} + \frac{d(S_2)}{dt} + c_1 c_2 x_2\right) - \frac{L^*C}{\gamma^*}\left(\Phi^T\hat{\Theta} + S_3\right) \tag{5.4}$$

Parameter estimate law:

$$\dot{\hat{\Theta}} = \Gamma\tau_2 - \Gamma\sigma_\Theta\left(\left\|\hat{\Theta}\right\|\right)\left(\hat{\Theta} - \hat{\Theta}_0\right) \tag{5.5}$$

where $\hat{\Theta}_0 = \hat{\Theta}(0)$, $\tau_2 = \tau_1 + \frac{z_3 C}{\gamma^*}\Phi$, $\tau_1 = \Phi z_2$.

In the above expressions the auxiliary variables z_1, z_2 and z_3 are defined in equations (5.6) to (5.8). The constant $C = c_1 + c_2$, the symbols $S_2 = sg_2(z_2)cf_2(|rz_2|)r$ and $S_3 = sg_3(z_3)cf_3(|rz_3|)r$ where $sg(y)$ and $cf(y)$ along with $\sigma_\Theta(y)$ are defined in Appendix C. Additionally, $r = \bar{R} + E$ is the bound on the uncertainty model and Γ is the diagonal adaption gain matrix. Compared with the control law proposed in [54], the present one employs one extra state x_3 in order to deal with the dynamics of the actuator. Compared with parameter update law proposed in [58], the present one uses the difference $\hat{\Theta} - \hat{\Theta}_0$ instead of $\hat{\Theta}$ to avoid that the possibility of the estimated parameter vector converging to zero [65].

Theorem 1

The closed loop system defined by (5.3), (5.4) and (5.5) is globally uniformly ultimately bounded $\forall\ t \geq 0$, under the assumptions 1-4. Furthermore, the control signal (5.4) and update law (5.5) are bounded.

Remark 1:

Noise entering the parameter estimate law will give rise to an ever increasing output [65,66]. This inevitably causes the switching-σ law to eventually be switch on. This robustness is achieved at the expense of destroying the ideal property of the adaption law [65]. However, this robustness is a necessity in real-time applications in order to avoid parameter drift which can lead to instability.

Remark 2:

From the parameter estimate law, it can be seen that when the switching-σ function is not zero and the states of the system approach zero, as $t \to \infty$ if the update law is to eventually cease updating then $\hat{\Theta} \to \hat{\Theta}_0$. This property is important in judging how the adaptive controller could perform if long periods of operation are encountered. Thus, essentially the performance observed directly when the controller is switched on is possible even after the adaption has taken place.

Proof of Theorem 1:

Introducing the tracking errors:

$$z_1 = x_1 - x_r \tag{5.6}$$

$$z_2 = x_2 - \alpha_1 \tag{5.7}$$

$$z_3 = x_3 - \alpha_2 \tag{5.8}$$

where α_1 and α_2 are the virtual control variables. Let the first Lyapunov candidate function be of the form

$$V_1 = \frac{1}{2} z_1^2 \tag{5.9}$$

Note that in this particular situation $x_r = 0$. The time derivative of V_1 is given by

$$\dot{V}_1 = z_1 \dot{z}_1 = z_1(\dot{x}_1) = z_1(z_2 + \alpha_1) \tag{5.10}$$

Choosing the first virtual control variable as

$$\alpha_1 = -c_1 z_1 \tag{5.11}$$

where c_1 is a positive constant. Substituting (5.11) in equation (5.10) yields

$$\dot{V}_1 = z_1 z_2 - c_1 z_1^2 \tag{5.12}$$

Let the second control Lyapunov function be selected as

$$V_2 = V_1 + \frac{1}{2} z_2^2 + \frac{1}{2} \tilde{\Theta}^T \Gamma^{-1} \tilde{\Theta} \tag{5.13}$$

where $\tilde{\Theta} = \Theta - \hat{\Theta}$. Taking the time derivative of equation (5.13) gives

$$\dot{V}_2 = \dot{V}_1 + z_2\dot{z}_2 + \tilde{\Theta}^T\Gamma^{-1}\dot{\tilde{\Theta}} \tag{5.14}$$

Taking the time derivative of equation (5.7) simply yields

$$\dot{z}_2 = \dot{x}_2 - \dot{\alpha}_1 \tag{5.15}$$

From equations (5.3), (5.8) and (5.11), equation (5.15) becomes

$$\dot{z}_2 = \Phi^T\Theta + R_e^* - \ddot{y} + \gamma^*(z_3 + \alpha_2) + c_1x_2 \tag{5.16}$$

Subsequently, the time derivative of V_2 after substitution of (5.16) into (5.14) becomes

$$\dot{V}_2 = \dot{V}_1 + z_2\left(\Phi^T\Theta + R_e^* - \ddot{y} + \gamma^*(z_3 + \alpha_2) + c_1x_2\right) + \tilde{\Theta}^T\Gamma^{-1}\dot{\tilde{\Theta}} \tag{5.17}$$

Letting the second virtual control variable be

$$\alpha_2 = \left(\frac{1}{\gamma^*}\right)\left(-z_1 - \Phi^T\hat{\Theta} - c_1x_2 - c_2z_2 - sg_2(z_2)cf_2(|rz_2|)r\right) \tag{5.18}$$

Combining equations (5.17) and (5.18), after some manipulation, $\dot{V}_2$ becomes

$$\dot{V}_2 = \dot{V}_1 + \tilde{\Theta}^T(\tau_1 - \Gamma^{-1}\dot{\hat{\Theta}}) - z_1z_2 - c_2z_2^2 + z_2\left(R_e^* - \ddot{y} - sg_2(z_2)cf_2(|rz_2|)r\right) + \gamma^*z_2z_3 \tag{5.19}$$

where the tuning function $\tau_1 = \Phi z_2$.

Moving to the next step, the time derivative of (5.18) is given by

$$\dot{\alpha}_2 = \frac{1}{\gamma^*}\left(-\dot{z}_1 - \frac{d(\Phi^T\hat{\Theta})}{dt} - \dot{x}_2c_1 - c_2\dot{z}_2 - \frac{d\left(sg_2(z_2)cf_2(|rz_2|)r\right)}{dt}\right) \tag{5.20}$$

With knowledge of (5.15) and (5.11), (5.20) is now

$$\dot{\alpha}_2 = \frac{1}{\gamma^*}\left(-\dot{z}_1 - \frac{d(\Phi^T\hat{\Theta})}{dt} - (c_1 + c_2)\dot{x}_2 - c_1c_2x_2 - \frac{d\left(sg_2(z_2)cf_2(|rz_2|)r\right)}{dt}\right) \tag{5.21}$$

The third tracking error for z_3 from (5.3) and (5.21) is

$$\dot{z}_3 = \dot{x}_3 - \dot{\alpha}_2$$

$$\dot{z}_3 = \left(e_c - R^* x_3 - k_v x_2\right)\frac{1}{L^*} - \frac{1}{\gamma^*}\left(-\dot{z}_1 - \frac{d(\Phi^T\hat{\Theta})}{dt} - (c_1 + c_2)\dot{x}_2 - c_1 c_2 x_2 \right. \tag{5.22}$$
$$\left. - \frac{d\left(sg_2(z_2)cf_2(|rz_2|)r\right)}{dt}\right)$$

Substituting $\dot{x}_2$ from (5.3) into (5.22) yields

$$\dot{z}_3 = \left(e_c - R^* x_3 - k_v x_2\right)\frac{1}{L^*} - \frac{1}{\gamma^*}\left(-\dot{z}_1 - \frac{d(\Phi^T\hat{\Theta})}{dt} - (c_1 + c_2)(\Phi^T\Theta + R_e^* - \ddot{y} + \gamma^* x_3) - c_1 c_2 x_2 \right.$$
$$\left. - \frac{d\left(sg_2(z_2)cf_2(|rz_2|)r\right)}{dt}\right) \tag{5.23}$$

Consequently, the next task is to prove the third control Lyapunov function is bounded. A candidate function for this purpose is chosen to be

$$V_3 = V_2 + \frac{1}{2}z_3^2 \tag{5.24}$$

Since this Lyapunov function contains all of the tracking errors and parameter estimate errors it can be viewed as the total Lyapunov function for the entire system denoted as $V = V_3$. Its time derivative is given by

$$\dot{V} = \dot{V}_2 + z_3\dot{z}_3 \tag{5.25}$$

Combining equations (5.19), (5.23) and (5.25) yields

$$\dot{V} = z_1 z_2 - c_1 z_1^2 + \tilde{\Theta}^T(\tau_1 - \Gamma^{-1}\dot{\hat{\Theta}}) - z_1 z_2 - c_2 z_2^2 - z_2\left(R_e^* - \ddot{y} - sg_2(z_2)cf_2(|rz_2|)r\right) + \gamma^* z_2 z_3$$
$$+ z_3\left\{\left(e_c - R^* x_3 - k_v x_2\right)\frac{1}{L^*} - \frac{1}{\gamma^*}\left(-\dot{z}_1 - \frac{d(\Phi^T\hat{\Theta})}{dt} - (\Phi^T\Theta + R_e^* - \ddot{y} + \gamma^* x_3)(c_1 + c_2) - c_1 c_2 x_2\right.\right.$$
$$\left.\left. - \frac{d\left(sg_2(z_2)cf_2(|rz_2|)r\right)}{dt}\right)\right\} \tag{5.26}$$

Letting the control voltage e_c in (5.26) applied to the electromagnets be given by (5.4) yields

$$\dot{V} = -c_1 z_1^2 + \tilde{\Theta}^T\left(\tau_2 - \Gamma^{-1}\dot{\hat{\Theta}}\right) - c_2 z_2^2 - c_3 z_3^2 + z_2\left(R_e^* - \ddot{y} - sg_2(z_2)cf_2(|rz_2|)r\right)$$
$$+ z_3\left(\frac{(c_1 + c_2)}{\gamma^*}\right)\left(R_e^* - \ddot{y} - sg_3(z_3)cf_3(|rz_3|)r\right) \tag{5.27}$$

Choosing the update law defined in equation (5.5) results in

$$\dot{V} = -c_1 z_1^2 - c_2 z_2^2 - c_3 z_3^2 + z_2\left(R_e^* - \ddot{y} - sg_2(z_2)cf_2(|rz_2|)r\right)$$
$$+ z_3\left(\frac{(c_1 + c_2)}{\gamma^*}\right)\left(R_e^* - \ddot{y} - sg_3(z_3)cf_3(|rz_3|)r\right) + \sigma_\Theta\left(\left\|\hat{\Theta}\right\|\right)\tilde{\Theta}^T\left(\hat{\Theta} - \hat{\Theta}_0\right) \tag{5.28}$$

Some further manipulation given in Appendix C shows that equation (5.28) can be reduced as

$$\dot{V} \le -c_0 V + d_0 \tag{5.29}$$

where c_0 and d_0 are positive constants defined in Appendix C. From equation (5.29), one has

$$V \le V(0)e^{-c_0 t} + \frac{d_0}{c_0}\left(1 - e^{-c_0 t}\right) \le V(0)e^{-c_0 t} + \frac{d_0}{c_0} \tag{5.30}$$

From the above analysis $V(t)$ is shown to be uniformly bounded $\forall t \ge 0$, which also implies that $z_1, z_2, z_3, \tilde{\Theta}$ are bounded. Thus, the system states and parameter estimate vector are also bounded $\forall t \ge 0$

5.3. Experiment and Results

In order to demonstrate the effectiveness of the proposed control strategy in real time, an experimental study was conducted. First, some results for the proposed controller are presented. Next, it is compared with the controller developed in [58]. Several observations are drawn.

5.3.1. Implementation

The experiments consisted of subjecting the isolation system to various disturbances, in the form of pulses and different forms of sinusoidal excitations. As in the previous chapters, a personal computer equipped with a data acquisition (DAQ) board (dSpace 1104) was used to collect signals and to generate control inputs. Simulink was used in conjunction with dSpace Control Desk software in order to implement the control. A sampling frequency of 1000 Hz was used in the real time implementation. Figure 5.1 shows a Simulink real time model used to implement the control scheme. A laser position sensor (Wenglor, CP24MHT80) was used to measure the relative displacement of the mass through ADC_C5 (analog-to-digital conversion). This was obtained by fastening the sensor directly to the base. The sensor utilizes a built in anti aliasing filter. The displacement signal was subtracted from a set point which was the equilibrium position of the mass. The current feedback was obtained by measuring the voltage over a 1ohm resistor connected in series with the actuator. This signal was then fed back through ADC_C6. These two real time signals were then fed into the algorithm as illustrated in Figure 5.1, which then resulted in a control voltage being sent to the power amplifier (Quanser, UPM-2405) through DAC_C5. The output of the power amplifier was connected directly to the actuator.

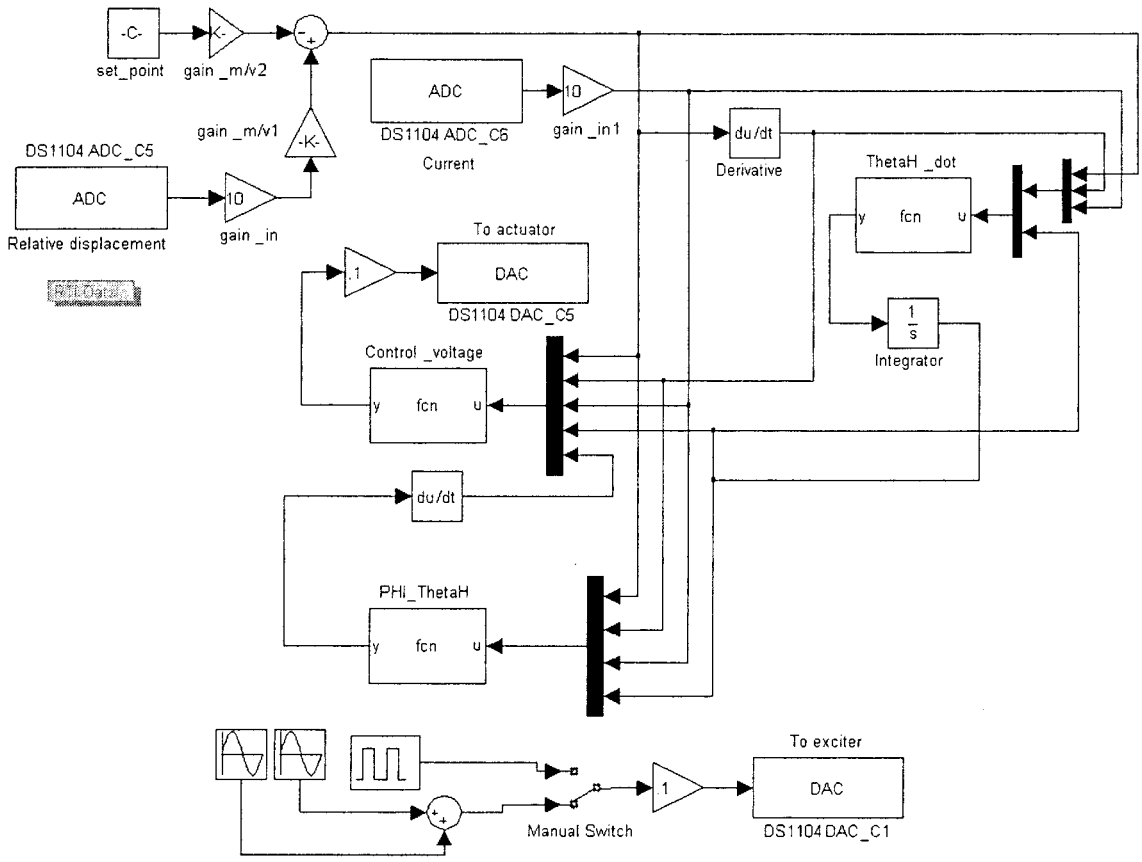

Figure 5.1. Simulink real time model for the proposed adaptive control algorithm

5.3.2. Proposed Controller Results

In this section the controller parameters and a few experimental results for the proposed control scheme are presented. It is important to note that in this section the magnitude of excitation of the base that was used was 1.5 times larger that of all other sections. The reason for this was to attempt to force the main structure further from the equilibrium position thus ensuring that the system enters the higher nonlinear regime. Also, for the same reason, the control current magnitudes are not rightfully comparable to the proceeding sections.

The actuator parametric values used in the controllers were those obtained from the preliminary characterization in Chapter 2. In experiment only Set two was used. The values of the constants v and d were chosen to be the maximum possible output foreseeable of the systems mass. These were chosen to be 0.5 and 0.008 respectively. Since the constant vector Θ is unknown, the value of M was chosen based on experiments. It is known that the value of M affects the upper bound on the adaption of the estimated parameters, thus M could be tuned in

real time by trial and error to achieve good tracking error without allowing the parameters to drift too far leading to instability. The value for M was determined to be 86 in this section. Similarly, the bound on uncertainty $r = \bar{R} + E$, could be tuned in experiment. It was determined to be a value of 5 for all experiments. As well, the adaption gain matrix, Γ , was chosen to be a diagonal matrix with values of 450 to allow for quick adaption of the parameter estimates. The remaining controller parameters were similarly tuned by trial and error in experiment until a good tracking performance was achieved. The parameters were $c_1 = 0.1$, $c_2 = 1$, $c_3 = 80$, $\varepsilon_{11} = 0.1$, $\varepsilon_{21} = 1.25$, $\varepsilon_{12} = 1.6$, $\varepsilon_{22} = 1$. The nonlinearity in the restoring force was taken to the 5^{th} order. Consequently, the vector

$$\Phi(x_1, x_2) = -\left(\frac{x_2}{v}, \frac{x_1}{d}, \left(\frac{x_1}{d}\right)^3, \left(\frac{x_1}{d}\right)^5\right)^T \tag{5.29}$$

was chosen as the ideal candidate. Finally, the initial parameter estimate vector was chosen to be $\hat{\Theta}_0 = [0.5, 10, 25, 50]^T$ with its 2^{nd} norm lying below M.

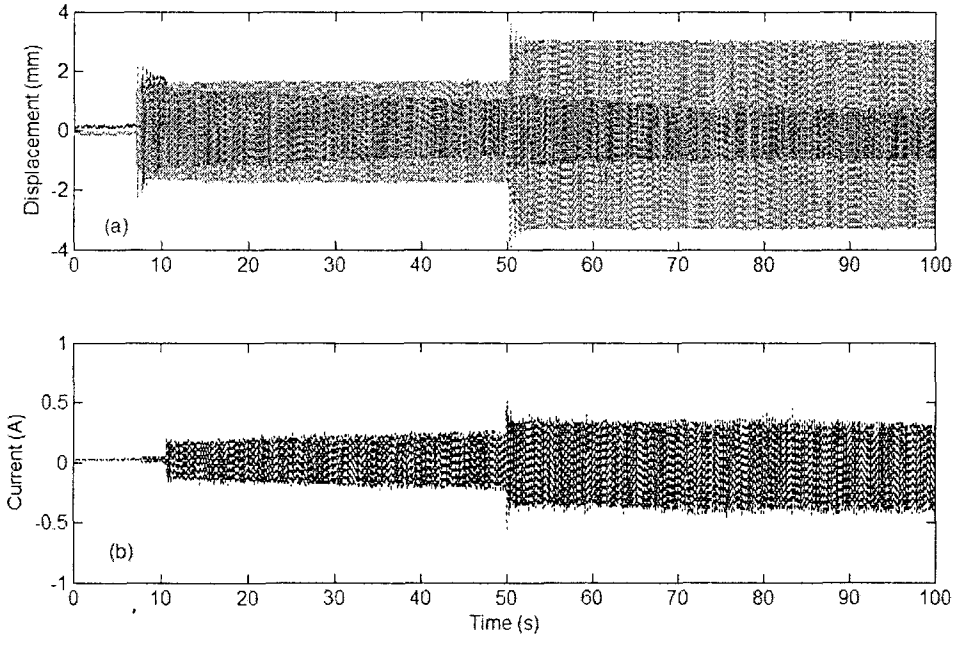

Figure 5.2. Experimental results, frequency step change (55 to 70rad/s): (a) response of the mass without control (dashed line), with control (solid line), (b) current of the actuator

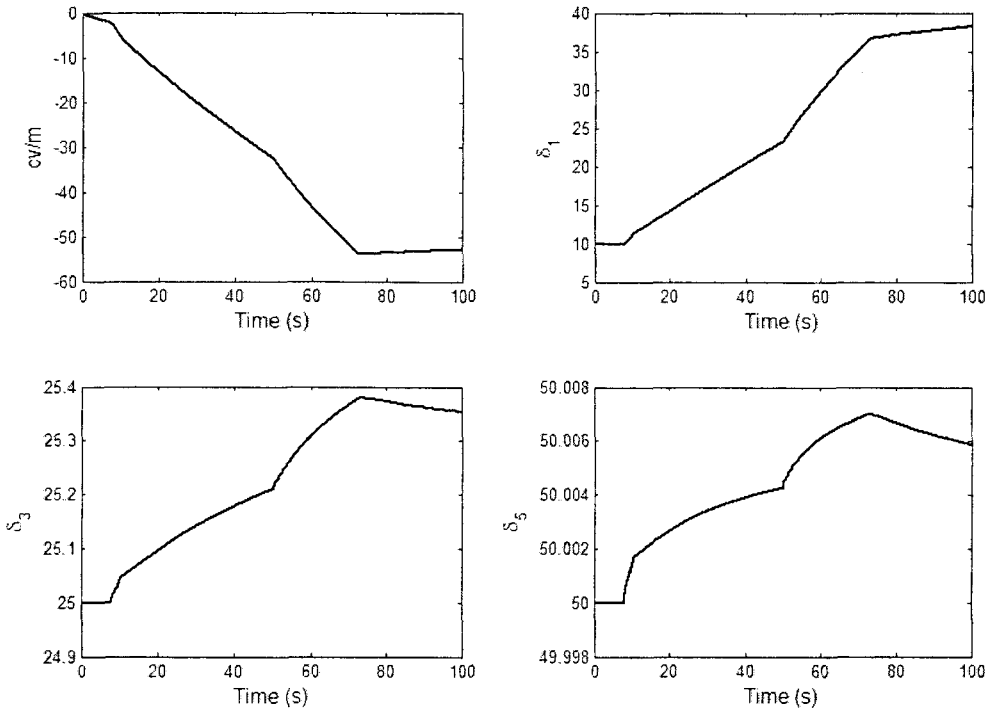

Figure 5.3. Experimental results, frequency step change: the estimated parameters

Figures 5.2 and 5.4 show some typical results for the control scheme. The parameter estimates are shown in Figures 5.3 and 5.5 for the same scenarios. The first experimental case subjected the system to a step change in frequency as can be observed in Figure 5.2. Initially the system was excited at a sinusoidal frequency of 55rad/s, and then at 50seconds it was suddenly changed to 70rad/s. The controller was turned on just after 10 seconds. It can be seen that the control achieved good response when compared with the open loop response. Also, the response progressively became better as the system adapted. Figure 5.3 shows the parameter estimates for this case. It should be noted that the switching-σ function in the adaption law eventually activated at about the 70 seconds mark. This indicates that $\|\hat{\Theta}\|$ reached M at that instant.

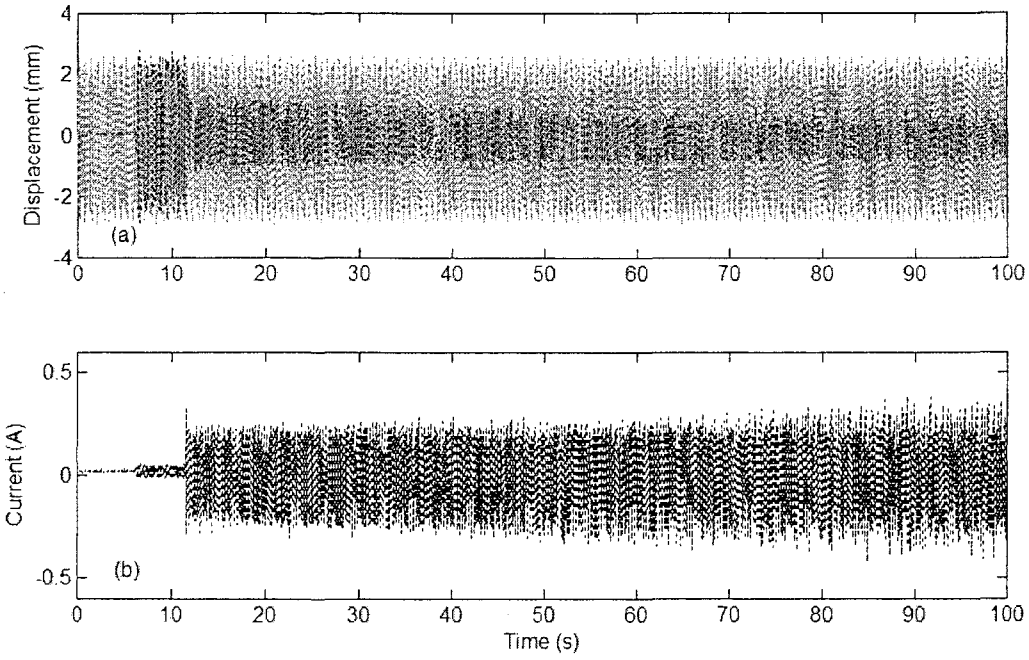

Figure 5.4. Experimental results, sum of 2 sinus frequencies (25+65): (a) response of the mass without control (dashed line), with control (solid line), (b) current of the actuator

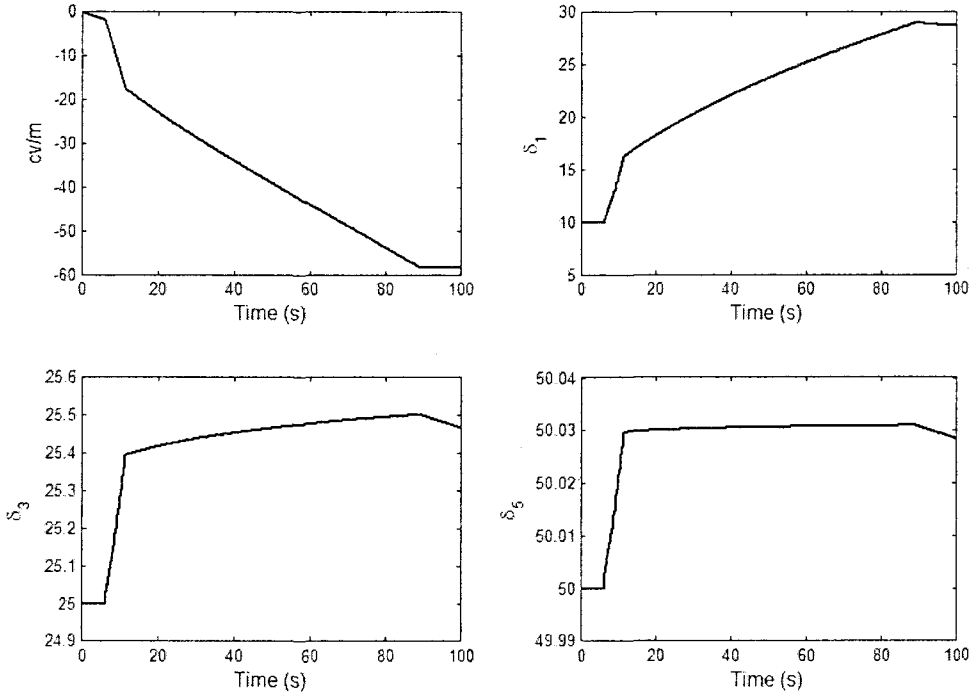

Figure 5.5. Experimental results, sum of 2 sinus frequencies (25rad/s+65rad/s): the estimated parameters

The response of the second cases is illustrated in Figure 5.4. This case involved exciting the system with a sum of 2 sinusoidal signals, one with a frequency of 25 rad/s and the other with a frequency of 65 rad/s. The control effort was again switched on just after 10 seconds. The system also responded very well to this case, again adapting as time progressed. The parameter estimates seen in Figure 5.5 follow a similar trend to the first case, this time the switching-σ function turned on at about 90 seconds. This is apparent due to the small sudden change in direction the estimates undergo. The final case in this section consisted of subjecting the base to a series of pulse excitations. This can be seen in Figure 5.6. Comparing the open loop responses to those of the closed loop, a reduction in both peak amplitude and settling time can be observed when the control is activated. The corresponding parameter estimates can be seen in Figure 5.7.

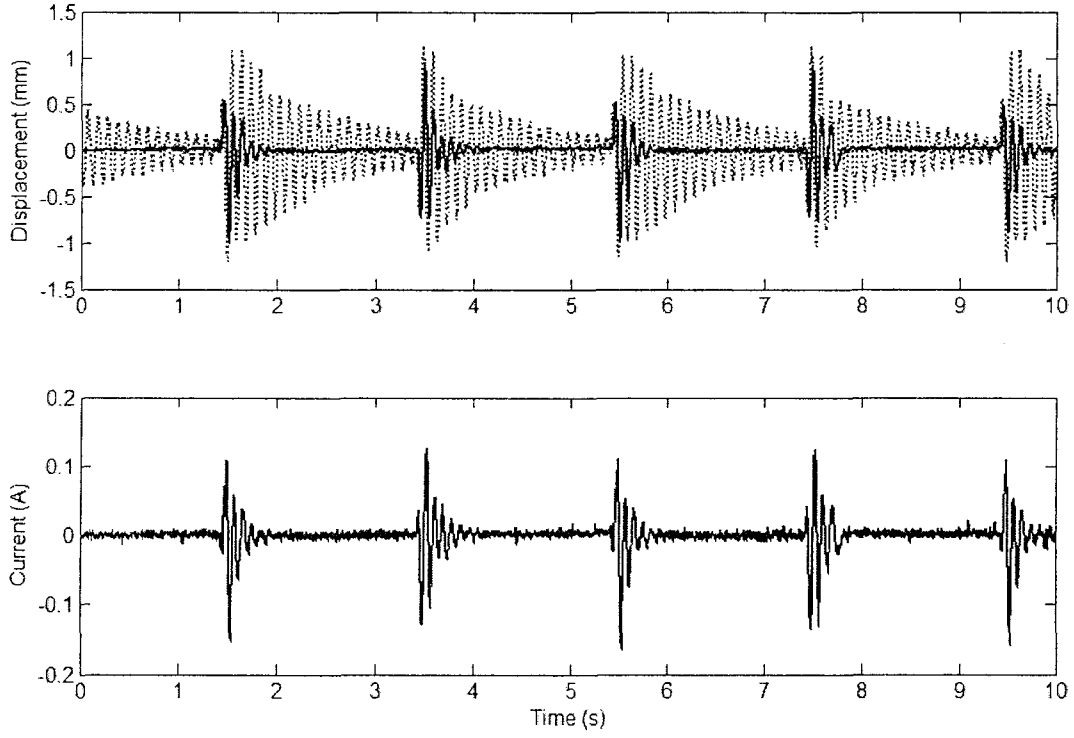

Figure 5.6. Experimental results, impulses given to the base: (a) relative displacement of the mass without control (dashed line), with adaptive control (line), (b) current in the actuator

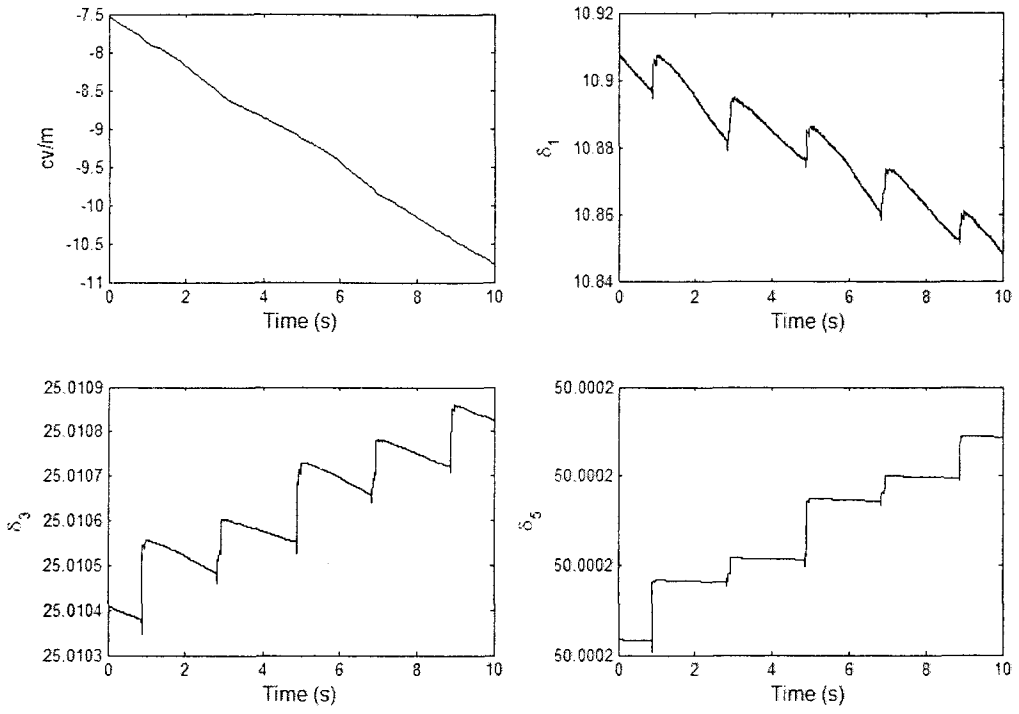

Figure 5.7. Experimental results, impulses given to the base; the parameter estimates

5.3.3. Controller Comparison Results

In this section the control scheme developed in [58] is implemented on the isolation system used in this thesis and compared with the proposed controller in real time experiments. It is noted that in this section the magnitude of the base excitation was kept at the same value as all other chapters in the thesis, different from that in section 5.3.2. From this point onward the control scheme developed by [58] is referred to as controller A and the proposed controller is referred to as controller B.

The implementation methodologies utilized in this section are the same as in section 5.3.1. A Simulink diagram for the implementation of the control scheme for controller A can be seen in Figure 5.8. Furthermore a brief outline of the control scheme for controller A is given in Appendix D. For both controllers the numerical values for the parameters v, d and Γ were the same values as those used in section 5.3.2. Also, equation (5.29) remained the same and was used for both controllers tested. The initial parameter estimate vector was also was taken as the same value for both controllers. Also, for the proposed controller the only parameter that varied from the previous section was M. As a result, two different and lesser values of M were used in this section.

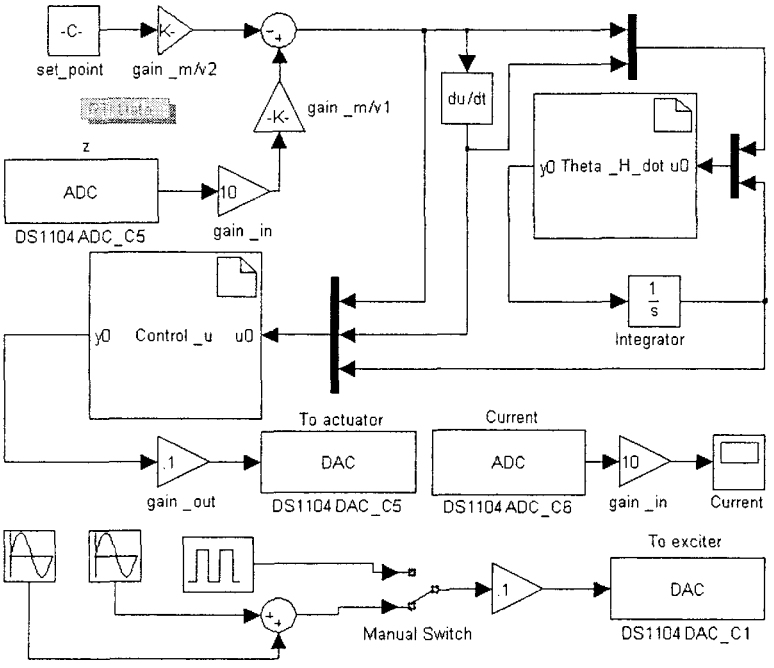

Figure 5.8. Simulink real time model for implementation (Controller A)

For controller A, M was experimentally tuned by trial and error for good performance while avoiding parameter drift, yielding a value of *68*. For controller B, initially a value of *68* was used for M followed by a few experiments with M increased to *78*. The remaining parameters for controller A were $r = 20.5$, $c_1 = 0.005$, $c_2 = 0.02$, $\varepsilon_1 = 86$, $\varepsilon_2 = 91$, determined in a manner similar to that used for M.

The results of the first experiment of this section can be observed in Figure 5.9 with parameter estimates in Figure 5.10. This consisted of subjecting controller A to a sinusoidal base excitation at 65rad/s. For comparison, controller B was subjected to precisely the same excitation and can be seen in Figure 5.11, with its parameter estimates shown in Figure 5.12. In general, controller B outperforms, although both controllers reduce the tracking error as time progressed. Interestingly, the parameter estimates, $\delta_1, \delta_3, \delta_5$, followed opposite directions when compared between the controllers.

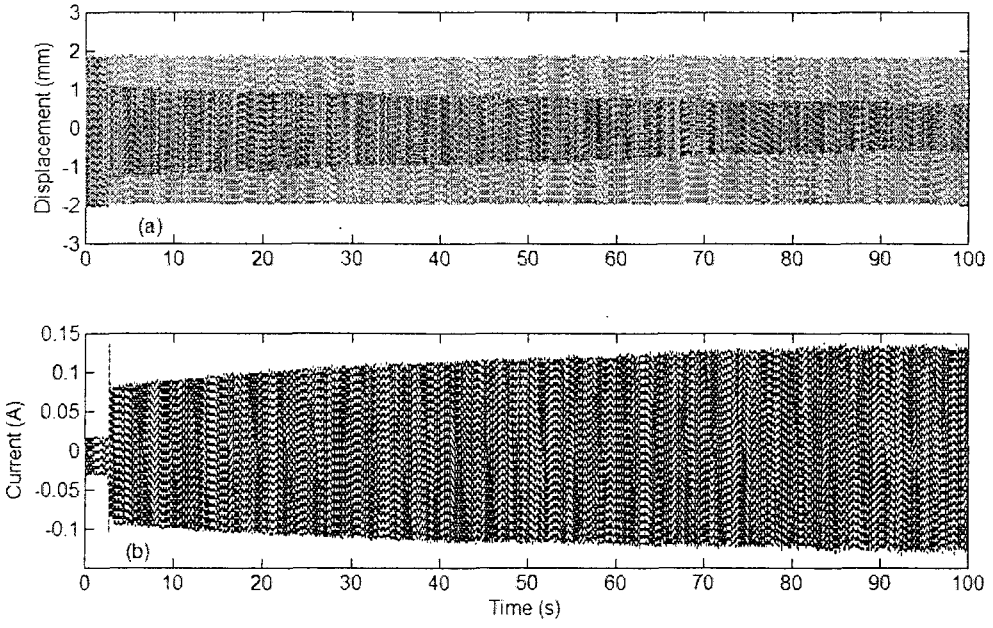

Figure 5.9. Controller A excited at 65 rad/s: (a) response of the mass without control (dashed line), with control (solid line), (b) current of the actuator

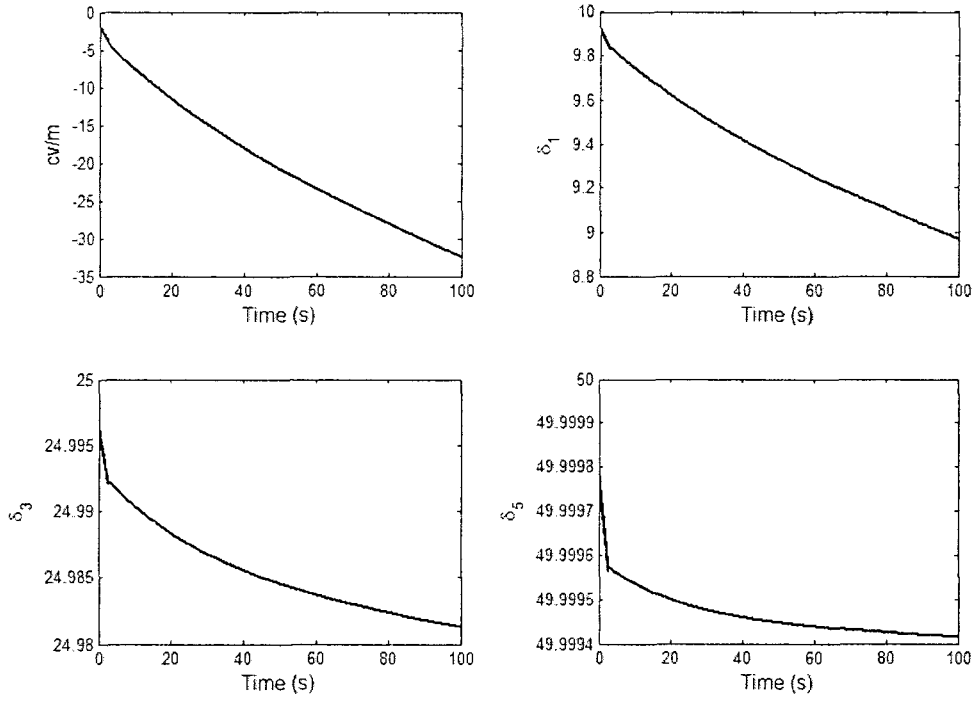

Figure 5.10. Controller A excited at 65 rad/s: the estimated parameters

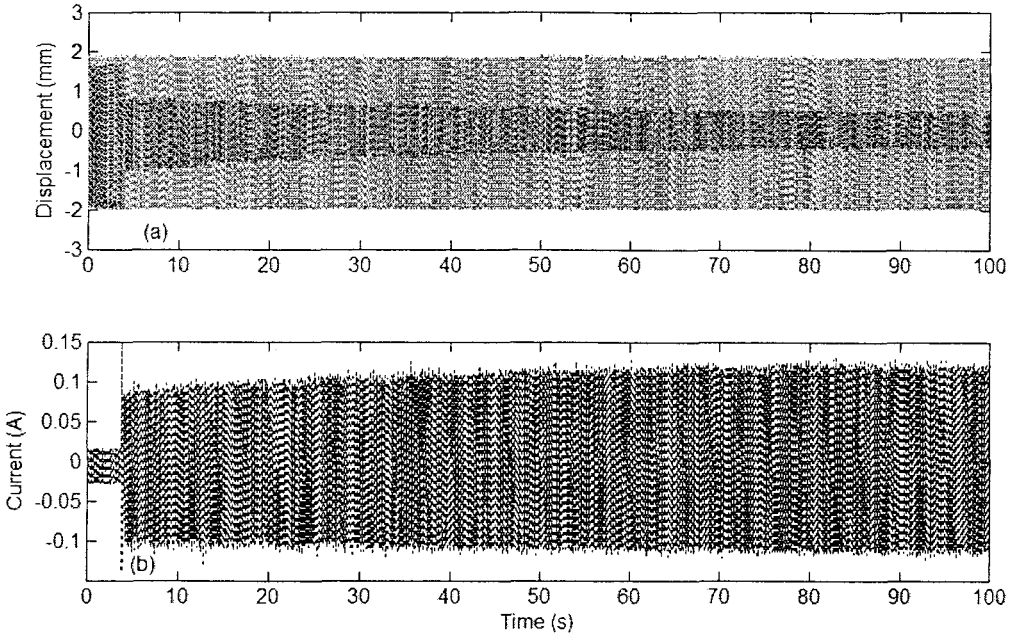

Figure 5.11. Proposed controller excited at 65 rad/s: (a) response of the mass without control (dashed line), with control (solid line), (b) current of the actuator

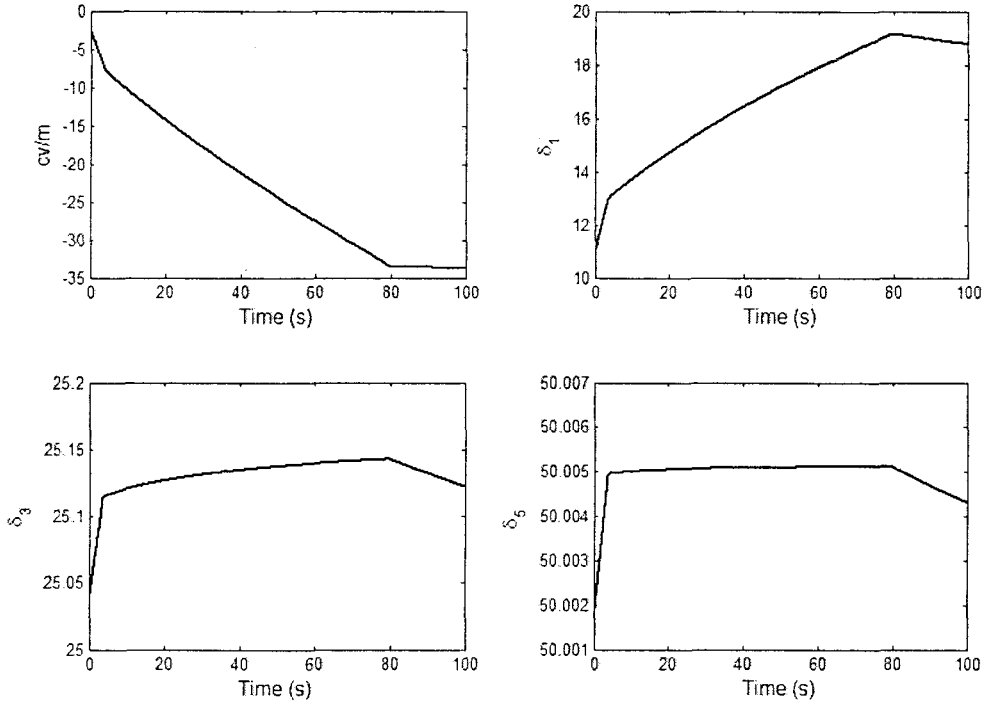

Figure 5.12. Proposed controller excited at 65 rad/s: the estimated parameters

The second experiment was conducted in ways similar to the first, with the exception that the controllers were now allowed to adapt for a period of time of 100 seconds before the results

were collected. In addition, for controller B, M was increased to *78*. The results can be observed in Figures 5.13 and 5.14 for controllers A and B respectively. In order to properly compare the control performances, the root mean square (RMS) value of the relative displacement signal and control current are used as performance measures. These are tabulated in Table 5.1. The RMS values calculated are based only on the last 3 seconds of the experimental tests. As observed from Table 5.1, controller B exhibited both a slightly lower control current RMS value and a lower displacement RMS value than that of controller A, amounting to more than a 70% performance increase.

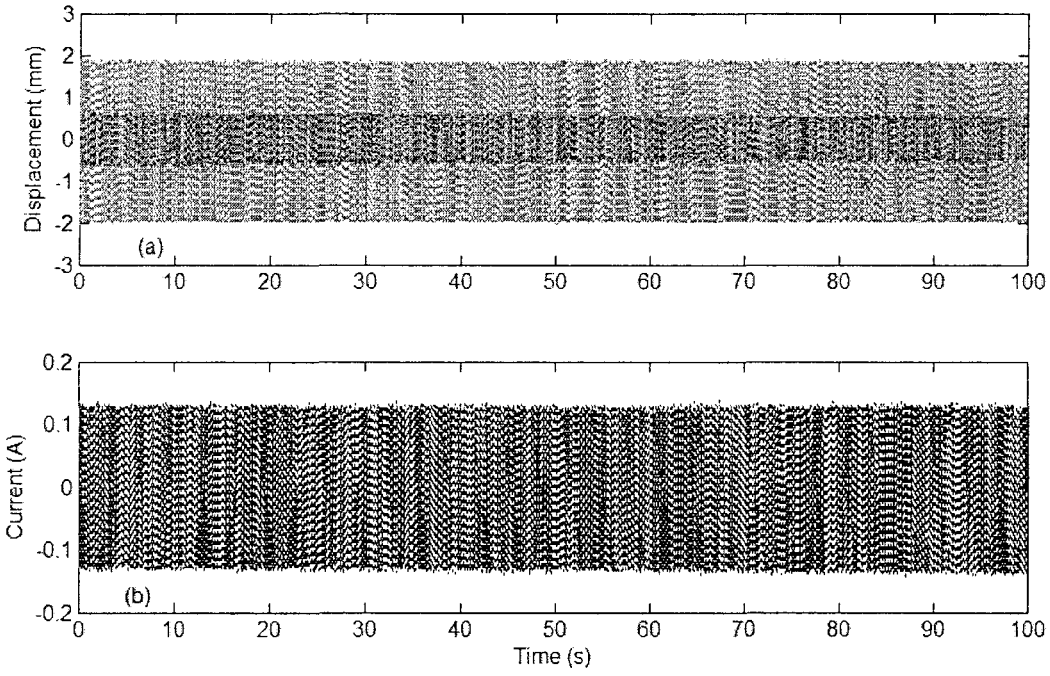

Figure 5.13. Controller A excited at 65 rad/s: (a) response of the mass without control (dashed line), with control (solid line), (b) current of the actuator

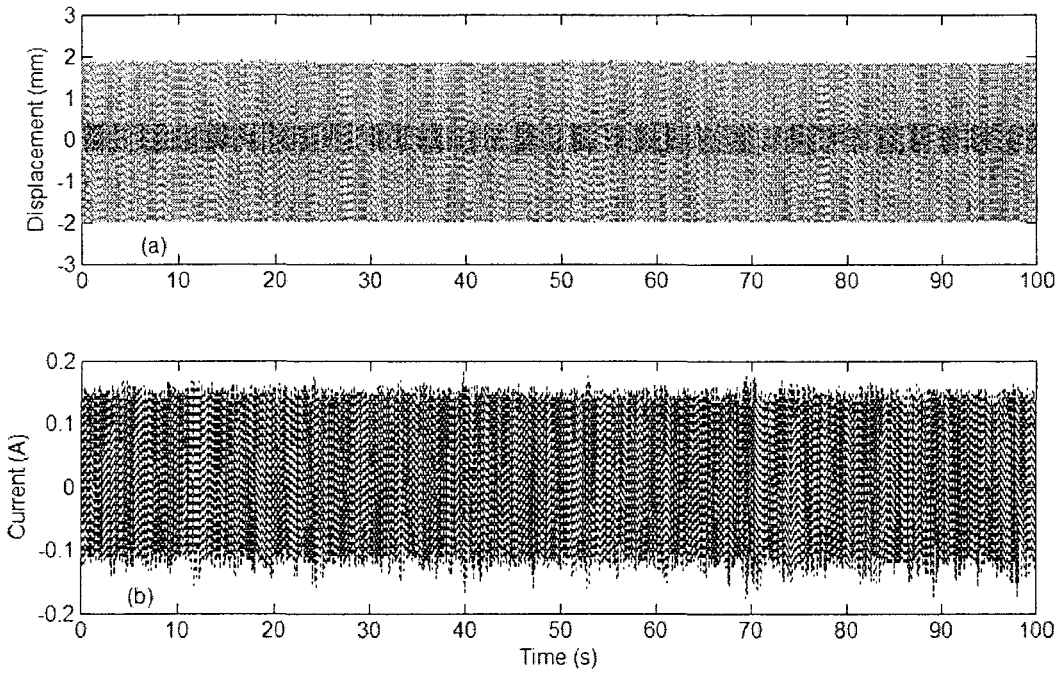

Figure 5.14. Controller B excited at 65 rad/s: (a) response of the mass without control (dashed line), with control (solid line), (b) current of the actuator

Table 5.1. The root mean square (RMS) values of the control responses with 65 rad/s base excitation; (a) the RMS values with the controller A, (b) the RMS values with controller B

	RMS open	RMS (a)	RMS (b)
z (mm)	1.3302	0.3637	0.2136
Current (A)	n/a	0.0906	0.0856

A magnified plot of the response of both controllers A and B with corresponding control current can be seen in Figure 5.15, showing the last 5 seconds of the second experiment described above.

The last experimental case consisted of subjecting the system to a base excitation of a sum of two sinusoidal frequencies. The results can be observed in Figures 5.16 and 5.18, with corresponding parameter estimates in Figures 5.17 and 5.19 for controllers A and B respectively. The two frequencies were 35 rad/s and 70 rad/s. This time the controllers were initially on then they were switched off at a time of 70 seconds as can be observed in Figures 5.16 and 5.18. In these experiments the values of M for each controller remains unchanged from the second

experiment. Comparing the responses in Figures 5.16 and 5.18, it is seen that the closed loop responses for both controllers for the first few seconds started out with a comparable magnitude. However, as the systems adapted controller B reduced the response more so without increasing its control effort over that of controller A.

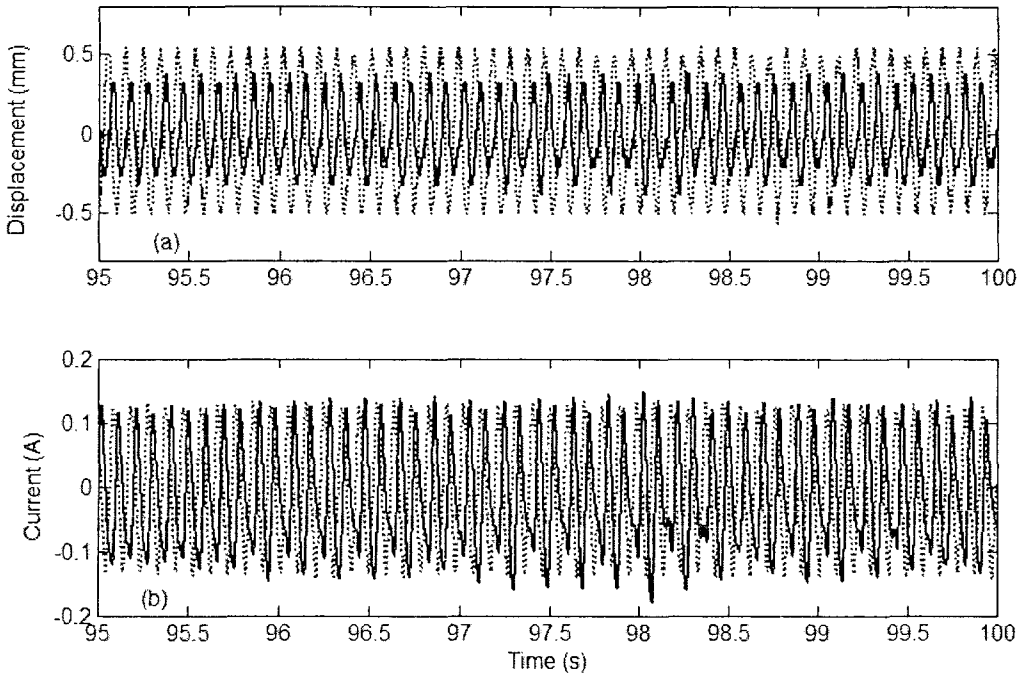

Figure 5.15. Magnified comparison of results, excited at 65 rad/s; Controller A (dotted), Controller B (solid): (a) response of the mass with control, (b) current of the actuator.

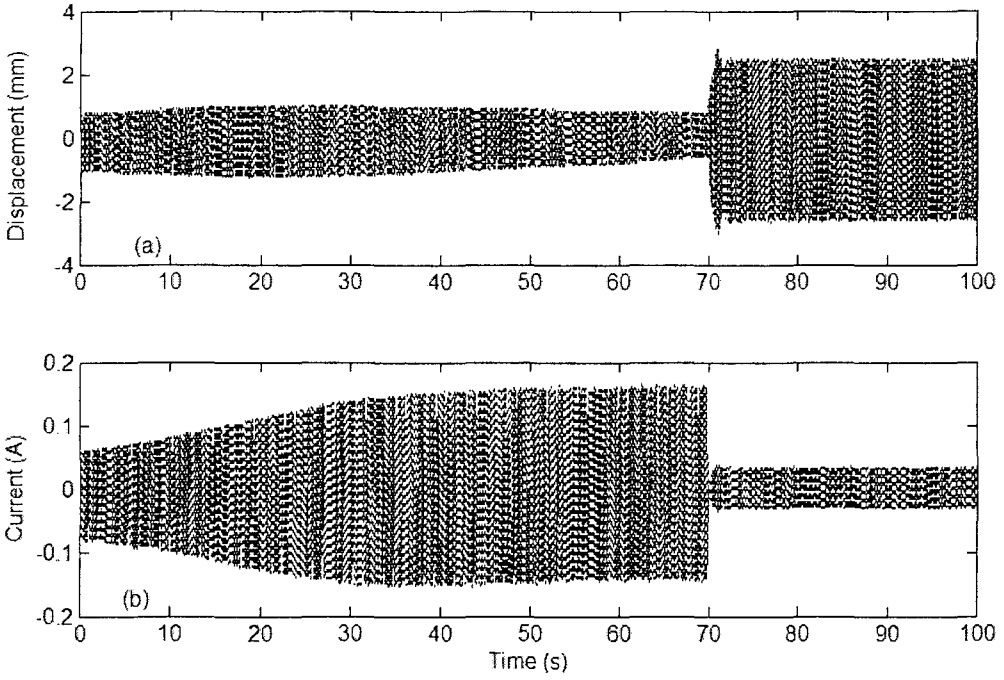

Figure 5.16. Controller A excited with a sum of 35+70 rad/s: (a) response of the mass with control, (b) current of the actuator

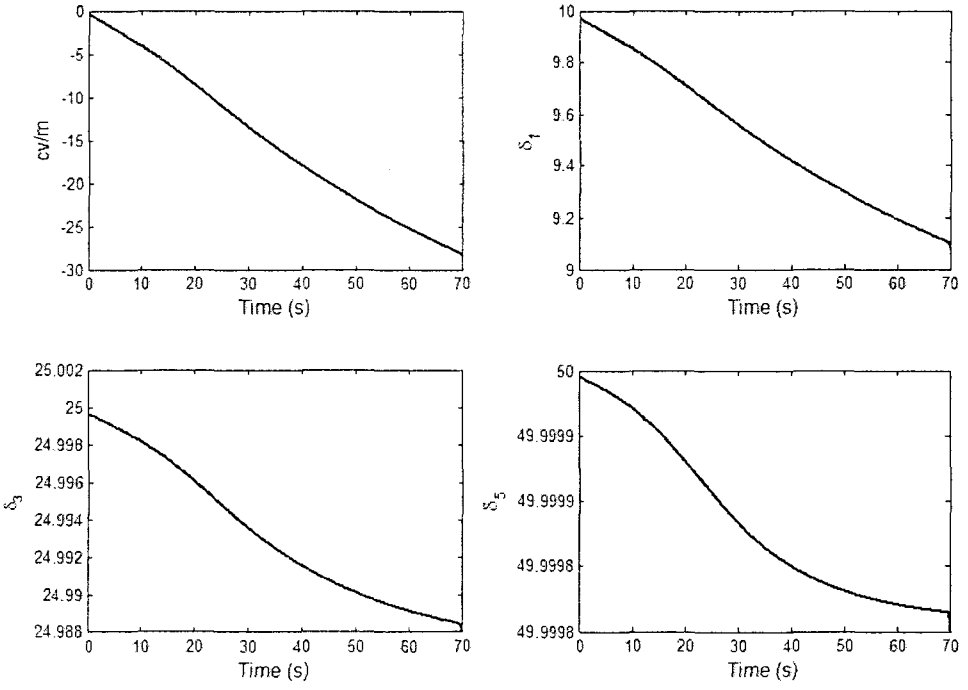

Figure 5.17. Controller A excited with a sum of 35+70 rad/s: the estimated parameters

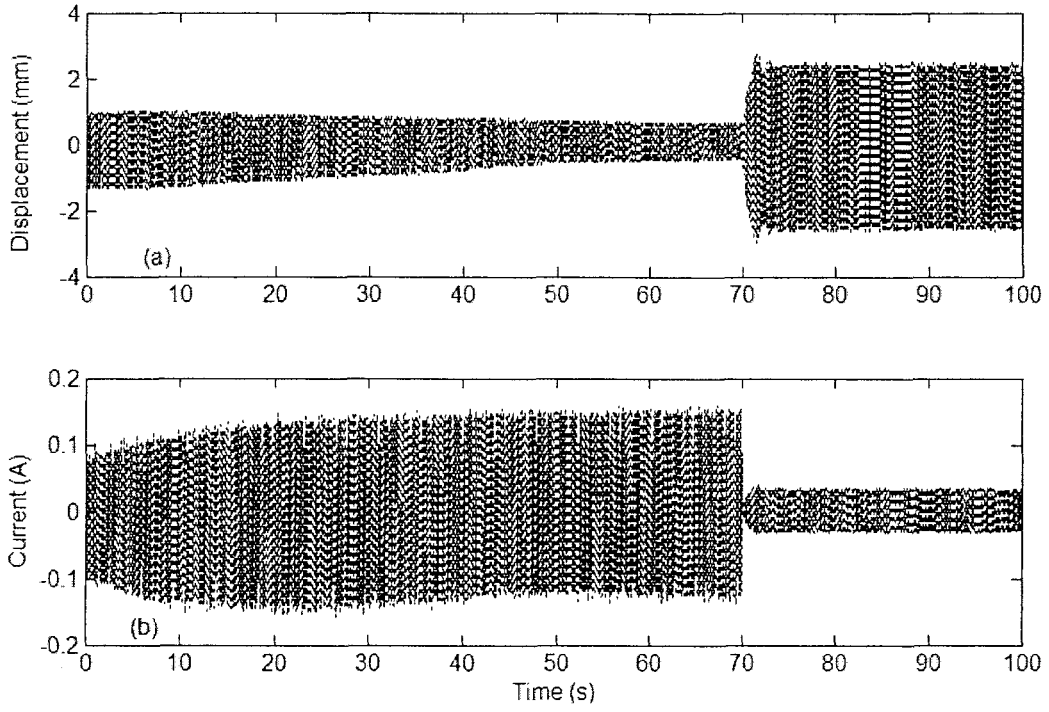

Figure 5.18. Controller B excited with a sum of 35+70 rad/s: (a) response of the mass with control, (b) current of the actuator

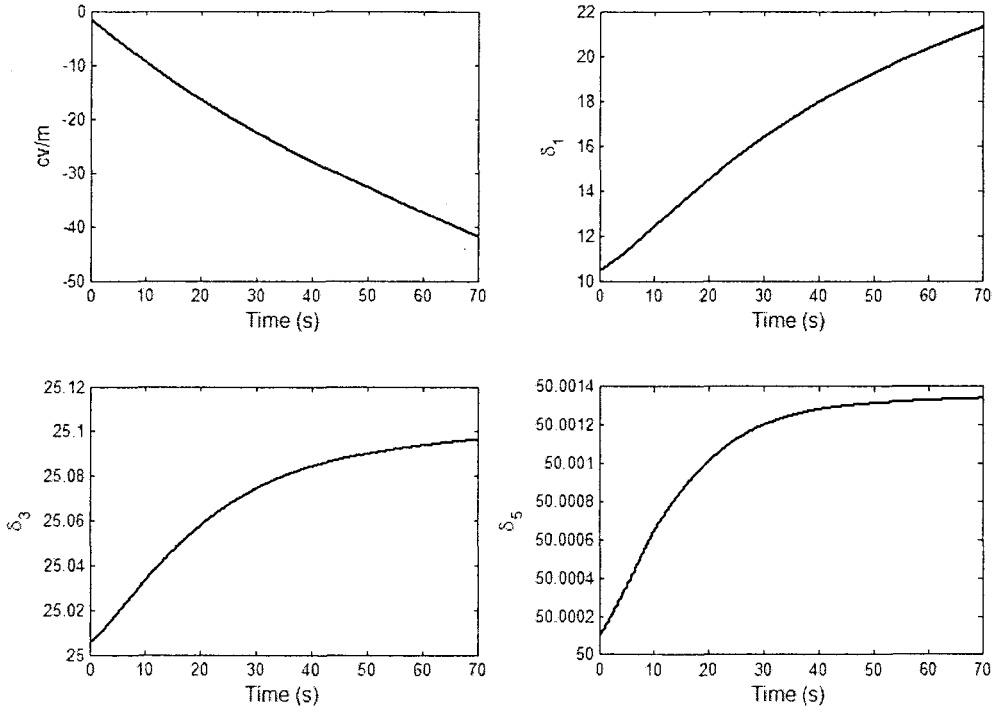

Figure 5.19. Controller B excited with a sum of 35+70 rad/s: the estimated parameters.

The resulting RMS values of the response and of the control current are tabulated in Table 5.2. The RMS values were computed for the data between 65 to 68 seconds. A performance increase of about 35% is seen in this case in favour of controller B. Notably, this increase in performance does not come at the expense of control effort. Observing the trend of the parameter estimates in Figures 5.17 and 5.19, again it can be noted that the direction of the estimates, $\delta_1, \delta_3, \delta_5$, differ greatly between the controllers. The real values for these parameters are known to be larger than what they are initially estimated to be. Thus, one would expect them to progressively increase as the system adapts. This increase occurs with controller B however, it is not observed in controller A. Consequently, it is speculated that controller B obtains a better adaption process when implemented on the studied system.

Table 5.2. The root mean square (RMS) values of the control responses with 35rad/s+70rad/s base excitation; (a) the RMS values with Controller A, (b) the RMS values with Controller B

	RMS open	RMS (a)	RMS (b)
z (mm)	1.7106	0.4619	0.3439
current (A)	n/a	0.0973	0.0833

5.4. Conclusions

In this chapter, an adaptive control scheme based on the backstepping technique is proposed for a nonlinear base isolation system. First, the adaptive scheme is formulated. Second, the real-time implementation of the control algorithm is addressed. The control parameters were tuned by experiment. Thirdly, some results for different testing scenarios are given, validating the function of the algorithm. Fourth, the control scheme developed in [58] is implemented with the proposed system while neglecting the effect of the actuator physics. The same testing scenarios are then compared between the two controllers. Two main findings are obtained. (1) The proposed adaptive scheme results in a better response performance than that of the controller proposed by [58] when implemented on the studied active isolator. This performance does not come at a cost of control effort. (2) the parameter estimates progress in different manners between the controllers studied. The proposed controller gives better estimates of the parameters, however, the estimates do not converge to the actual values for either of the controllers in closed

loop. These two findings reinforce the notion that neglected physics when using backstepping can cause performance degradation and even make parameter estimation inaccurate. Nonetheless, the drawback of the proposed scheme is that it requires significant computational power.

CHAPTER 6 - CONCLUSIONS AND FUTURE WORKS

This chapter summarizes the research work conducted for this thesis. It also briefly outlines future works.

6.1. Summary

In this thesis, active control characteristics and methodologies have been investigated. First, a complete system characterization was conducted to fully understand the system character in a dynamical situation. This also served as a model validation and a means to discover any nonlinearities that may not be accurately quantifiable by other methods. Second, a phase compensation technique was investigated. This was due to the inherent instability of the closed loop system when using a direct negative proportional feedback. A design methodology proposed minimizing the 2^{nd} norm of the transmissibility. Experiments were conducted validating the controller to perform in real time with an automatic on/off switching technique that takes advantage of the active and passive regimes. Third, a delayed feedback control technique was investigated. The analytical crossing gains of the system subjected to a NPF and a PPF were derived and presented. The performance of the system and how this relates to inherent time lags within the control loop were determined. Subsequently, the stability of the system that relates to delays within the control loop was investigated. Both analytical and numerical investigations were sought. Changes to the closed loop active damping and natural frequency, and their relation to the combinations of gain and injected delay were also examined. Numerical optimization was conducted in order to determine the best gain-delay combinations for both NPF and PPF. Experiments were conducted with performance measure for three different controllers. Finally, a real-time study considering the proposed isolator as uncertain and/or possessing time-varying parameters was conducted. The adaptive control formulation was presented. A control law based on the adaptive backstepping technique was presented. The control scheme was implemented onto the proposed active isolation system validating its functionality and compared with a relevant controller. For both controllers, the design parameters were tuned online for good tracking error. Several experiments were conducted and the proposed controller was shown to provide better performance and parameter estimate convergence. The performance increase was thought to be directly related to the inclusion of the actuator physics in the control law.

Although the three main methods proposed in this thesis are separate ways to achieve a similar end goal, the purpose and usefulness of each may vary depending on application

specifics. More specifically, the following briefly outlines some attributes to consider in choosing and comparing between the three methods proposed in this thesis. For the phase compensation technique outlined in chapter 3, three main features are evident. (1) The controller may be realized using low computational power. (2) It performs very well in the low to mid-frequency region. (3) It requires prior knowledge about the system parameters to function properly. In regards to the time delayed position feedback control technique outlined in chapter 4 the following features are apparent. (1) It is possible to realize the controller by choosing a time constant of the actuators making computational power unnecessary. Thus, if the isolation application has no available computer for use, this method would be ideal. (2) This method provides good isolation characteristics over the entire frequency region while using minimal control effort. (3) This method requires prior knowledge of the system parameters. Lastly, with regard to the adaptive backstepping method proposed in chapter 5, three main features exist. (1) The method requires significant computational effort. (2) It requires sensing of all system states. (3) It functions in the face of uncertainties and time varying parameters.

6.2. Main Contributions

The contributions of the thesis are as follows.

(1) Dynamic mathematical models of the proposed active isolation system are developed.

(2) Optimal phase compensation technique with automatic utilization of active and passive regions was realized. The experimental results show that with the proposed control scheme, the isolator is able to effectively suppress base excitations.

(3) Different from previous studies, effects of the inherent time delay caused by the actuator are determined. The analytical crossing gains for NPF and PPF are derived for the system. A new finding is that for base isolation, some degree of an inherent time delay present in hardware is beneficial when a direct positive position feedback is used. Based on these findings, ways in which a delayed feedback control can be utilized have been presented and implemented.

(4) An adaptive nonlinear controller for base isolation is proposed. A performance increase and parameter estimate accuracy increase is noted when comparing the proposed control

scheme to one notable scheme that neglects the actuator physics. The differences between the proposed control scheme and other related schemes are outlined in chapter 5.

(5) A 2DOF model of a unique vibration isolation system that posses a HSDLS property is designed and constructed for future work in the area of semi-active and active vibration isolation.

To conclude, it can be stated that the objectives set out for this thesis have been fulfilled. It is noted that the findings reported above are applicable to similar systems.

6.3. Future Work

The research conducted in this thesis has provided much insight and some interesting findings for a few regimes of active vibration isolation. The proof of concepts herein lay a foundation for further research in the area of vibration isolation. A few areas thought to be worth noting for future study are as follows

(1) Limitations of the linearization of the full nonlinear dynamic model of the system should be investigated. Naturally, as is the case with any approximations in engineering there exist regimes in which the models will fall over. This deserves further investigation with the proposed active isolator.

(2) In chapter 3, the implementation of the phase compensation technique also involved an automatic on/off switching algorithm. It was noted that the dramatic on/off action of the controller sometimes caused a transient to dominate the frequency spectrum. In order to alleviate the effects of the transient, it is thought that it is possible to provide a more gradual transition between the on mode and the off mode. This notion certainly deserves investigation.

(3) In chapter 4 where the delayed feedback control notion has been investigated, one of the findings was that a sufficient inherent time lag is beneficial to the closed-loop control response when using a relative PPF signal. There is one possibility that is to investigate the optimal time constant of the actuator that yields the best isolation characteristics.

(4) In chapter 5 the improvement in performance was obtained with an increase in complexity of the adaptive controller. Investigation into an adaptive controller that can yield good tracking error and at the same time be realized with minimal complexity is well worth investigating. Other methods such as neural adaptive, or genetic algorithms can be considered.

(5) Also related to chapter 5, the effect of the order in the nonlinearity assumed for the parameter estimates can be investigated. Whether any increase in performance can be achieved with a higher order approximation can be investigated.

(6) The 2DOF model of a HSLDS vibration isolator that was designed and constructed by the author of this thesis will be considered for future research in the areas of semi-active and active vibration isolation. A CAD model of the setup can be seen in Figure 6.1, with corresponding photograph of the constructed system in Figure 6.2. The purpose of this

system is to extent the research into the 2 degree of freedom (2DOF) regime. The reason for extending the degree of freedom from one to two is that a 2DOF model is thought to better suite to the majority of realistic systems.

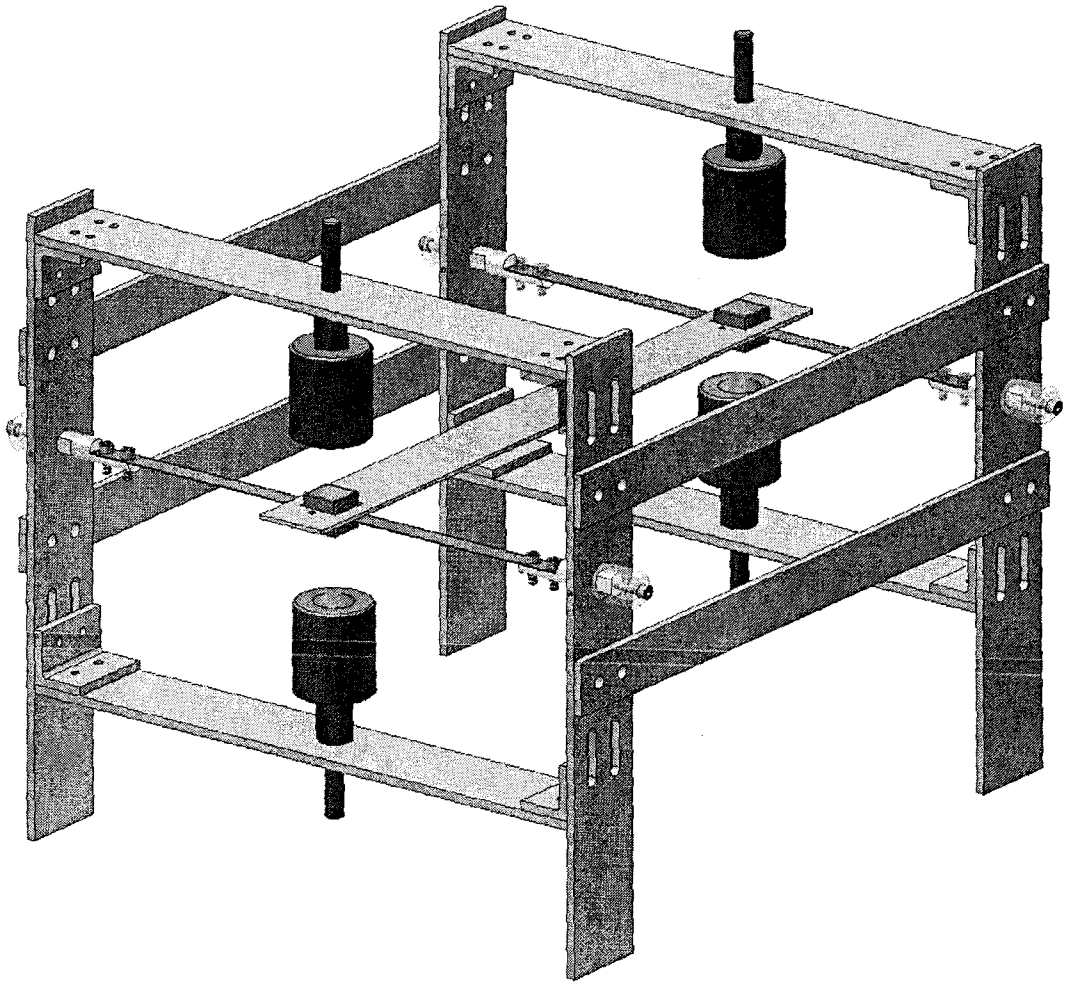

Figure 6.1. CAD model of the 2DOF vibration isolation system

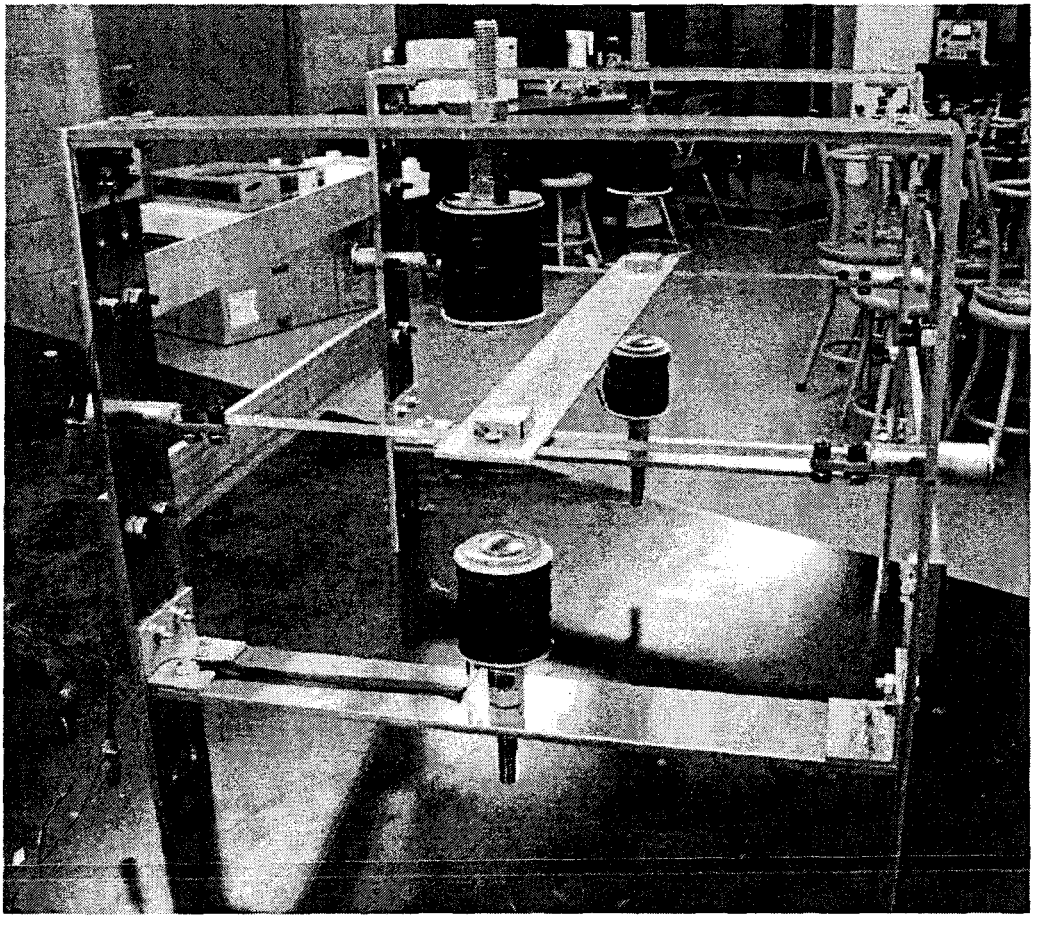

Figure 6.2. Photograph of the 2DOF vibration isolator

REFERENCES

[1] Inman, D. J., *Engineering Vibration*, 3rd Edition Prentice-Hall, Inc., Upper Saddle River, New Jersey, 2008.

[2] Preumont A, Seto K. *Active Control of Structures*. John Wiley & Sons, Ltd.: Cornwall, 2008.

[3] Ungar, EE, Equality of Force and Motion Transmissibilities, *Journal of Acoustical Societies of America*, 1991; 90:596-597.

[4] Ibrahim R, Recent advances in nonlinear passive vibration isolators, *Journal of Sound and Vibration*, 2008; 314:371–452.

[5] Carrella A. Passive vibration isolators with high-static-low-dynamic-stiffness, Ph.D. Thesis, University of Southampton, 2008.

[6] Carrella A, Brennan MJ, Waters TP, Static analysis of a passive vibration isolator with quasi-zero-stiffness characteristic, *Journal of Sound and Vibration*, 2007; 301:678-689.

[7] Kovacica I, Brennan MJ, Waters TP, A study of a nonlinear vibration isolator with a quasi-zero stiffness characteristic, *Journal of Sound and Vibration*, 2008; 315:700-711.

[8] Liu Y, Waters TP, Brennan MJ, A comparison of semi-active damping control strategies for vibration isolation of harmonic disturbances, *Journal of Sound and Vibration*, 2005; 280:21-39.

[9] Liu Y, Waters TP, Brennan MJ, Semi-active vibration isolation system with variable stiffness and damping control, *Journal of Sound and Vibration*, 2008; 313:16–28.

[10] Nitta Y, y, Nishitani A, Spencer B, Semiactive control strategy for smart base isolation utilizing absolute acceleration information, *Structural Control and Health Monitoring*, 2006; 13:649–659.

[11] Zhou X, Anil K, Jann N, Semi-active and passive control of the phase I linear base-isolated benchmark building model, *Structural Control and Health Monitoring*, 2006; 13:626–648.

[12] Shook D, Roschke P, Ozbulut O, Superelastic semi-active damping of a base-isolated structure, *Structural Control and Health Monitoring*, 2008; 15:746–768.

[13] Benassi L, Elliott SJ, Gardonio P, Active vibration isolation using an inertial actuator with local force feedback control, *Journal of Sound and Vibration* 2004; 276:157-179.

[14] Huang X, Elliott SJ, Brennan MJ, Active isolation of a flexible structure from base vibration, *Journal of Sound and Vibration* 2003; 263:357-376.

[15] Yan B, Brennan MJ, Elliott SJ, Ferguson NS, Active vibration isolation of a system with a distributed parameter isolator using absolute velocity feedback control, *Journal of Sound and Vibration*, 2010; 329:1601-1614

[16] Abakumov AM, Miatov GN, Control algorithms for active vibration isolation systems subject to random disturbances, *Journal of Sound and Vibration*, 2006; 289:889–907.

[17] Olsson C, Active automotive engine vibration isolation using feedback control, *Journal of Sound and Vibration*, 2006; 294:162–176.

[18] Nagarajaiah S, Narasimhan S, Smart base isolated benchmark building Part II: Phase I Sample controllers for linear isolation system, *Structural Control and Health Monitoring*, 2006; 13:589-604.

[19] Nagarajaiah S, Narasimhan S, Johnson E, Structural control benchmark problem: phase II nonlinear smart base isolated building subjected to near fault ground motions, *Structural Control and Health Monitoring*, 2008; 15:653-656.

[20] Narasimhan S, Nagarajaiah S, Johnson E, Smart base isolated benchmark building part IV: phase II sample controllers for nonlinear isolation systems, *Structural Control and Health Monitoring*, 2008; 15:657-672.

[21] Zhou N, Liu K, A tunable high-static–low-dynamic stiffness vibration isolator, *Journal of Sound and Vibration*, 2010; 329:1254-1273.

[22] I. Stefanini, M. Markovic, Y. Perriard, 3D Inductance and Impedance Determination Taking Skin Effect Into Account, *2005 IEEE International Conference on Electric Machines and Drives*, 74 – 79

[23] T. Zedler, A. Nikanorov, B. Nacke, Investigation of relative magnetic permeability as input data for numerical simulation of induction surface hardening, *International Scientific Colloquium on Modelling for Electromagnetic Processing*, 2008; 119-126

[24] N. Zhou, A Tunable High-Static–Low-Dynamic-Stiffness Isolator and Fuzzy-Neural Network Based Active Control Isolator, M.Sc. Thesis, Lakehead University, 2009.

[25] D. Zhang, X. Mei, X. Hao, A. Tian., Modeling Dynamic Magnetic Force and Robust Control, *IEEE International Conference on Systems and Control*, 2007; 349-354.

[26] Coppola G., Liu K., Control of a unique active vibration isolator with a phase compensation technique and automatic on/off switching, *Journal of Sound and Vibration*, In press (doi:10.1016/j.jsv.2010.06.025).

[27] Coppola G, Liu K, Control of a Unique Active Vibration Isolator, Proceedings of The Canadian Society for Mechanical Engineering Forum, Victoria, British Columbia, Canada June 2010.

[28] Chena C, Ricles JM, Analysis of actuator delay compensation methods for real-time testing, *Engineering Structures*, 2009; 31: 2643-2655

[29] Clark RL, Franmton KD, Phase compensation for feedback control of enclosed sound fields, *Journal of Sound and Vibration*, 1996; 195:701-718

[30] Ahmadizadeh M, Mosqueda G, Reinhorn AM, Compensation of actuator delay and dynamics for real-time hybrid structural simulation, *Earthquake Engineering and Structural Dynamics*, 2008; 37:21-42.

[31] Houiuchi T, Inoue M, Konno T, Namita Y, Real-time hybrid experimental system with actuator delay compensation and its application to a piping system with energy absorber, *Earthquake Engineering and Structural Dynamics*, 1999; 28:1121-1141.

[32] Ren MZ, Seto K, Doi F, Feedback structure-borne sound control of a flexible plate with an electromagnetic actuator: the phase lag problem. *Journal of Sound and Vibration*, 1997; 205:57-80.

[33] Wong TH, Design of a magnetic levitation control system – an undergraduate project. *IEEE Transactions on Education,* 1986; 29:196-200.

[34] D'Azzo JJ., Houpis CH, *Linear Control System analysis and design.* Second edition, McGraw-Hill, New York, 1981.

[35] Ogata K, *Modern Control Engineering.* Fourth edition, Prentice Hall, 1996.

[36] Yan B, Active Vibration Isolation with a Distributed Parameter Isolator, Ph.D. Thesis, University of Southampton, 2007.

[37] Zhu WH, Tryggvason B, Piedboeuf JC, On active acceleration control of vibration isolation systems, *Control Engineering Practice* 2006; 14:863–873.

[38] Agarwal AK, Fujino Y, Bhartia B. Instability due to time delay and its compensation in active control of structures. *Earthquake Engineering and Structural Dynamics* 1993; 22:211–224.

[39] Agarwal AK, Yang JN. Compensation for time delay for control of civil engineering structures. *Earthquake Engineering and Structural Dynamics* 2000; 29:37–62.

[40] Masoud ZN, Nayfeh AH, Al-Mousa A, Delayed position-feedback controller for the reduction of payload pendulations of rotary cranes, *Journal of Vibration and Control* 2003; 9:257-277.

[41] Jnifene A, Active vibration control of flexible structures using delayed position feedback, *Systems & Control Letters* 2007; 56:215-222.

[42] Daqaq MF, Alhazza KA, Arafat HN, Non-linear vibrations of cantilever beams with feedback delays, *International Journal of Non-Linear Mechanics* 2008; 43:962-978.

[43] Hamdi M, Belhaq M, Self-excited vibration control for axially fast excited beam by a time delay state feedback, *Chaos, Solitons & Fractals* 2009; 41:521-532.

[44] Udwadia FE, von Bremen HF, Kumar R, Hosseini M, Time delayed control of structural systems, *Earthquake Engineering and Structural Dynamics* 2003; 32:495-535.

[45] Udwadia FE, von Bremen HF, Phohomsiri P, Time-delayed control design for active control of structures: principles and applications, *Structural Control and Health Monitoring* 2007; 14:27–61.

[46] Chen L, Cai G, Ji P, Experimental study of delayed feedback control for a flexible plate, *Journal of Sound and Vibration* 2009; 322:629-651.

[47] Phohomsiri P, Udwadia FE, von Bremen HF, Time-delayed positive velocity feedback control design for active control of structures, *Journal of Engineering Mechanics* 2006; 132:690-703.

[48] Udwadia FE, Phohomsiri P, Active control of structures using time delayed positive feedback proportional control designs, *Structural Control and Health Monitoring* 2006; 13:536-552.

[49] Olgac N, Holm-Hansen B, A Novel active vibration absorption technique: delayed resonator, *Journal of Sound and Vibration* 1994; 176:93-104.

[50] Elmali H, Renzulli M, Olgac N, Experimental comparison of delayed resonator and PD controlled vibration absorbers using electromagnetic actuators, *Transactions of the ASME,* 2000; 122:514–520.

[51] Liu J, Liu K, Application of an active electromagnetic vibration absorber in vibration suppression, *Structural Control and Health Monitoring* 2010; 17:278-300.

[52] Coppola G, Liu K, Time Delayed Position Feedback Control for a Unique Active Vibration Isolator, Submitted to *Structural Control and Health Monitoring* June 1, 2010.

[53] Hong T, Hughes PC, Effect of time delay on the stability of flexible Structures with rate feedback control , *Journal of Vibration and Control* 2001; 7:33-49.

[54] Shaw J, Active vibration isolation by adaptive control, *Proceeding of the 1999 IEEE International Conference on Control Applications.*

[55] Mohamed Z, Martins JM, Tokhi MO, Sá da Costa J, Botto MA, Vibration control of a very flexible manipulator system, *Control Engineering Practice*, 2005; 13:267-277.

[56] De Luca A, Siciliano B, Zollo L, PD control with on-line gravity compensation for robots with elastic joints: Theory and experiments, *Automatica*, 2005; 14:1809-1819.

[57] Sugisaka M, Hazry D, Development of a proportional control method for a mobile robot, *Applied Mathematics and Computation*, 2007; 186:74-82.

[58] Mañosa V, Ikhouane F, Rodellar J, Control of uncertain non-linear systems via adaptive backstepping, *Journal of Sound and Vibration*, 2005; 280:657-680.

[59] Zuo L, Slotine JE, Nayfeh SA, Experimental Study of a Novel Adaptive Controller for Active Vibration Isolation, *Proceeding of the 2004 American Control Conference*

[60] Ikhouane F, Mañosa V, Rodellar J, Adaptive control of a hysteretic structural system, *Automatica*, 2005; 41:225-231.

[61] Zhou J, Wang Y, Real-time nonlinear adaptive backstepping speed control for a PM synchronous motor, *Control Engineering Practice*, 2005; 13:1259-1269.

[62] Chen KT, Chou CH, Chang SH, Liu YH, Intelligent active vibration control in an isolation platform, *Applied Acoustics,* 2008; 69:1063–1084.

[63] Anderson BDO, Dehghani A, Challenges of adaptive control- past, permanent and future, *Annual Reviews in Control*, 2008; 32:123-135.

[64] Zhou J, Wen C, *Adaptive Backstepping Control of Uncertain Systems*, 2008 Springer-Verlag, Berlin Heidelberg.

[65] Ioannou P. and J. Sun *'Robust Adaptive Control'* published by Prentice Hall, Inc in 1996

[66] Åström, K. J., Wittenmark, B., *Adaptive Control,* First Edition, Addison-Wesley Publishing Company, 1989.

APPENDIX A

Electromagnetic Force Model

Firstly, consider the interaction force between only one of the EMs and the PM. According to the study conducted in [21], this force consists of two parts:

$$F = F_{pc} + F_{pf} \tag{A1}$$

where F_{pc} denotes an attracting force between the core of the EM and the PM and F_{pf} the force due to the interaction between the PM and the flux generated by the energized EM. It was found that F_{pc} and F_{pf} can be expressed as

$$F_{pc} = e^{-a_3|i|}\frac{a_1}{(d+a_2)^4} \tag{A2}$$

and

$$F_{pf} = sign(i)(1-e^{-b_3|i|})\frac{b_1}{(d+b_2)^4} \tag{A3}$$

, respectively, where d denotes the distance between the PM and the EM, i is the current in the EM, $sign(i)=1$ if $i>0$, $sign(i)=-1$ if $i<0$, and a_1, a_2, b_1, b_2, and b_3 are constants that depend on the setup and can be determined experimentally. For the present apparatus shown in Fig. 1, if the PM is displaced by a distance z, the total force on the PM becomes

$$F = F_{pc}(d_1) - F_{pc}(d_2) + F_{pf}(d_1) + F_{pf}(d_2) \tag{A4}$$

where

$$d_1 = \frac{D-h}{2} - z,\ d_2 = \frac{D-h}{2} + z. \tag{A5}$$

Substituting Eqs. (A2) and (A3) in Eq. (A4) yields

$$F = e^{-a_3|i|}a_1\left[\frac{1}{(q_1-z)^4}-\frac{1}{(q_1+z)^4}\right]+sign(i)(1-e^{-b_3|i|})b_1\left[\frac{1}{(q_2-z)^4}+\frac{1}{(q_2+z)^4}\right]$$
$$= e^{-a_3|i|}\frac{8a_1q_1z(q_1^2+z^2)}{(q_1^2-z^2)^4}+sign(i)(1-e^{-b_3|i|})b_1\frac{2(q_2^4+6q_2^2z^2+z^4)}{(q_2^2-z^2)^4} \quad \text{(A6)}$$

where

$$q_1 = \frac{D-h}{2}+a_2,\ q_2 = \frac{D-h}{2}+b_2. \quad \text{(A7)}$$

The first term on the right-hand side of Eq. (A6) represents the difference in the attracting force. This term can be linearized as

$$e^{-a_3|i|}a_1\left[\frac{1}{(q_1-z)^4}-\frac{1}{(q_1+z)^4}\right]\approx(1-a_3|i|)a_1\left[\frac{1}{q_1^4}+\frac{4}{q_1^5}z-\frac{1}{q_1^4}+\frac{4}{q_1^5}z\right]=(1-a_3|i|)\frac{8a_1}{q_1^5}z. \quad \text{(A8)}$$

The second term on the right-hand side of Eq. (A6) represents the sum of the actuating force generated by the energized EMs. This term can be linearized as

$$sign(i)(1-e^{-b_3|i|})b_1\left[\frac{1}{(q_2-z)^4}+\frac{1}{(q_2+z)^4}\right]\approx sign(i)(1-1+b_3|i|)b_1\left[\frac{1}{q_2^4}+\frac{4}{q_2^5}z+\frac{1}{q_2^4}-\frac{4}{q_2^5}z\right]=\frac{b_1b_3}{q_2^4}2i \quad \text{(A9)}$$

It is further assumed that the influence of the coil current on the interacting force between the PM and the EM cores can be neglected or $(1-a_3|i|)\approx 1$. Thus the linearized interacting force is given by

$$F = \frac{8a_1}{q_1^5}z+\frac{b_1b_3}{q_2^4}2i. \quad \text{(A10)}$$

The first term on the right-hand side of the above equation depends on the displacement of the PM, which indicates that the interacting force between the PM and the EM cores acts as a negative spring. The second term on the right-hand side of the above equation indicates that the actuating force is proportional to the current and inversely proportional to D^4.

APPENDIX B

The crossing gain of the direct position feedback

By defining the following variables

$$a_0 = \frac{kR}{mL} + \frac{2\gamma K_p}{mL} \tag{B1}$$

$$a_1 = \frac{cR}{mL} + \frac{k}{m} + \frac{2\gamma k_v}{mL} \tag{B2}$$

$$a_2 = \frac{R}{L} + \frac{c}{m} \tag{B3}$$

equation (8) can be rewritten as

$$s^3 + a_2 s^2 + a_1 s + a_0 = 0 \tag{B4}$$

For a realistic system, the roots of equation (B4) consist of a pair of complex conjugates and a real number. Thus equation (B4) can be expressed as

$$(s - r_1)(s - r)(s - r^*) = 0 \tag{B5}$$

where r_1 is a real number and $r = -\sigma + j\omega_d$. Equation (B5) can further be written in the form

$$s^3 + (2\sigma - r_1)s^2 + (\omega_n^2 - 2r_1\sigma)s - r_1\omega_n^2 = 0 \tag{B6}$$

A comparison of equation (B6) with equation (B4) results in

$$\begin{aligned} a_2 &= 2\sigma - r_1 \\ a_1 &= \omega_n^2 - 2r_1\sigma \\ a_0 &= -r_1\omega_n^2 \end{aligned} \tag{B7}$$

Solving the above equations for σ yields

$$8\sigma^3 - 8\sigma^2 a_2 + 2(a_2^2 + a_1)\sigma + a_0 - a_1 a_2 = 0 \tag{B8}$$

It is well known that the condition of $\sigma = 0$ corresponds to the boundary between stability and instability. If

$$a_0 = a_1 a_2 \tag{B9}$$

Using equation (B9), the crossing gain for the NPF is given by

$$\hat{K}_p = \left(\left(\frac{Rc}{mL} + \frac{k}{m} + \frac{2\gamma k_v}{mL}\right)\left(\frac{R}{L} + \frac{c}{m}\right) - \frac{kR}{mL}\right)\frac{mL}{2\gamma} \tag{B10}$$

Solving equations (B7) for r_1 yields

$$r_1^3 + a_2 r_1^2 + a_1 r_1 + a_0 = 0 \tag{B11}$$

The condition for $r_1 = 0$ is given by

$$a_0 = 0 \tag{B12}$$

From it, the crossing gain for the PPF is given by

$$\hat{K}_p = -\frac{kR}{2\gamma} \tag{B13}$$

APPENDIX C

Proof that equation (5.28) is bounded for all time:

For convince, the final Lyapunov function and its time derivative arrived at in section 5.2 are shown below

$$V\left(z_1, z_2, z_3, \tilde{\Theta}\right) = \frac{1}{2}z_1^2 + \frac{1}{2}z_2^2 + \frac{1}{2}z_3^2 + \frac{1}{2}\tilde{\Theta}^T\Gamma^{-1}\tilde{\Theta} \tag{C1}$$

$$\dot{V} = -c_1 z_1^2 - c_2 z_2^2 - c_3 z_3^2 + z_2\left(R_e^* - \ddot{y} - sg_2(z_2)cf_2(|rz_2|)r\right) + z_3\left(\frac{(c_1+c_2)}{\gamma^*}\right)\left(R_R - \ddot{y} - sg_3(z_3)cf_3(|rz_3|)r\right) + \sigma_\Theta\left(\left\|\hat{\Theta}\right\|\right)\tilde{\Theta}^T\left(\hat{\Theta} - \hat{\Theta}_0\right) \quad \text{(C2)}$$

Notably, the below proof is largely inspired by [58].

Considering the term $\Delta_1 \triangleq z_2\left(R_R - \ddot{y} - sg_2(z_2)cf_2(|rz_2|)r\right)$ in equation (C2) one can observe that

if $|z_2| > \frac{\varepsilon_{21}}{1+r} + \frac{2\varepsilon_{11}}{r}$ then $sg_2(z_2) = sign(z_2)$ and $cf_2(|rz_2|) = 1$

Thus, $\Delta_1 = z_2\left(R_R - \ddot{y}\right) - |z_2|r$. And since $|R_R - \ddot{y}| \le r$ then $\Delta_1 \le 0$.

Now considering the other possibility, that is if $|z_2| < \frac{\varepsilon_{21}}{1+r} + \frac{2\varepsilon_{11}}{r}$, then

$sg_2(z_2) \le 1$ and $cf_2(|rz_2|) \le 1$.

Consequently, $|\Delta_1| = |z_2|\left(|R_R - \ddot{y}| + |sg_2(z_2)cf_2(|rz_2|)r|\right)$ and $|sg_2(z_2)cf_2(|rz_2|)r| \le r$, then,

$|\Delta_1| \le 2r|z_2|$.

Since $|z_2| < \frac{\varepsilon_{21}}{1+r} + \frac{2\varepsilon_{11}}{r}$, then $|\Delta_1| \le 2r|z_2| \le 2r\left(\frac{\varepsilon_{21}}{1+r} + \frac{2\varepsilon_{11}}{r}\right)$. And since $\frac{r}{r+1} < 1, \ \forall r > 0$

then $|\Delta_1| \le 2\varepsilon_{21} + 4\varepsilon_{11}$ in any case.

In a similar fashion the term $\Delta_2 \triangleq z_3\left(\frac{(c_1+c_2)}{\gamma^*}\right)\left(R_R - \ddot{y} - sg_3(z_3)cf_3(|rz_3|)r\right)$ can be proven

always less than or equal to $\frac{c_1+c_2}{\gamma^*}\left(2\varepsilon_{22} + 4\varepsilon_{12}\right)$.

Therefore, the function (C2) becomes

$$\dot{V} = -c_1 z_1^2 - c_2 z_2^2 - c_3 z_3^2 + \sigma_\Theta\left(\left\|\hat{\Theta}\right\|\right)\tilde{\Theta}^T\left(\hat{\Theta} - \hat{\Theta}_0\right) + 2\varepsilon_{21} + 4\varepsilon_{11} + \frac{c_1+c_2}{\gamma^*}\left(2\varepsilon_{22} + 4\varepsilon_{12}\right) \quad \text{(C3)}$$

Now considering the term $\Delta_3 \triangleq \sigma_\Theta\left(\left\|\hat{\Theta}\right\|\right)\tilde{\Theta}^T\left(\hat{\Theta} - \hat{\Theta}_0\right)$ appearing in equation (C3) for the case

when $\left\|\hat{\Theta}\right\| \ge 2M$ and utilizing Assumptions 1 and 4;

$$\sigma_\Theta\left(\left\|\hat{\Theta}\right\|\right)\tilde{\Theta}^T\left(\hat{\Theta}-\hat{\Theta}_0\right)=\bar{\sigma}\,\tilde{\Theta}^T\left(\Theta-\tilde{\Theta}\right)-\bar{\sigma}\,\tilde{\Theta}^T\hat{\Theta}_0$$

$$=\bar{\sigma}\left(\tilde{\Theta}^T\left(\Theta-\hat{\Theta}_0\right)-\left\|\tilde{\Theta}\right\|^2\right)\le\bar{\sigma}\left(2M\left\|\tilde{\Theta}\right\|-\left\|\tilde{\Theta}\right\|^2\right)$$

$$=\bar{\sigma}\left(2M\left\|\tilde{\Theta}\right\|-\frac{1}{4}\left\|\tilde{\Theta}\right\|^2-\frac{3}{4}\left\|\tilde{\Theta}\right\|^2\right)=\bar{\sigma}\left(-\left[\frac{1}{2}\left\|\tilde{\Theta}\right\|-2M\right]^2+4M^2-\frac{3}{4}\left\|\tilde{\Theta}\right\|^2\right)$$

$$\le 4\bar{\sigma}M^2-\frac{3}{4}\bar{\sigma}\left\|\tilde{\Theta}\right\|^2$$

Notice in the above that completing the squares of $2M\left\|\tilde{\Theta}\right\|-\frac{1}{4}\left\|\tilde{\Theta}\right\|^2$ results in

$$-\left[\frac{1}{2}\left\|\tilde{\Theta}\right\|-2M\right]^2+4M^2.$$

On the other hand, if $\left\|\hat{\Theta}\right\|\le 2M$ then $\left\|\tilde{\Theta}\right\|\le\left\|\Theta-\hat{\Theta}\right\|\le\|\Theta\|+\left\|\hat{\Theta}\right\|\le 3M$ So

$$\sigma_\Theta\left(\left\|\hat{\Theta}\right\|\right)\tilde{\Theta}^T\left(\hat{\Theta}-\hat{\Theta}_0\right)=\sigma_\Theta\left(\tilde{\Theta}^T\Theta-\left\|\tilde{\Theta}\right\|^2-\tilde{\Theta}^T\hat{\Theta}_0\right)=\sigma_\Theta\left(\tilde{\Theta}^T\left(\Theta-\hat{\Theta}_0\right)-\left\|\tilde{\Theta}\right\|^2\right)$$

$$\le\bar{\sigma}\left(2M\left\|\tilde{\Theta}\right\|-\left\|\tilde{\Theta}\right\|^2\right)=\bar{\sigma}\left(2M\left\|\tilde{\Theta}\right\|-\left\|\tilde{\Theta}\right\|^2-\frac{3}{4}\left\|\tilde{\Theta}\right\|^2+\frac{3}{4}\left\|\tilde{\Theta}\right\|^2\right)$$

$$\le\bar{\sigma}\left(2M\left\|\tilde{\Theta}\right\|-\frac{3}{4}\left\|\tilde{\Theta}\right\|^2+\frac{3}{4}\left\|\tilde{\Theta}\right\|^2\right)\le\bar{\sigma}\left(6M^2+\frac{27}{4}M^2\right)-\frac{3}{4}\bar{\sigma}\left\|\tilde{\Theta}\right\|^2$$

$$=\frac{51}{4}\bar{\sigma}M^2-\bar{\sigma}\frac{3}{4}\left\|\tilde{\Theta}\right\|^2$$

So, $\Delta_3\le\frac{51}{4}\bar{\sigma}M^2-\bar{\sigma}\frac{3}{4}\left\|\tilde{\Theta}\right\|^2$. Subsequently, from equation C3 the following is obtained:

$$\dot{V}\le-c_1z_1^2-c_2z_2^2-c_3z_3^2-\bar{\sigma}\frac{3}{4}\left\|\tilde{\Theta}\right\|^2+\frac{51}{4}\bar{\sigma}M^2+2\varepsilon_{21}+4\varepsilon_{11}+\frac{c_1+c_2}{\gamma^*}\left(2\varepsilon_{22}+4\varepsilon_{12}\right)$$

$$\le-\min\left(c_1,c_2,c_3,\bar{\sigma}\frac{3}{4}\right)\left(z_1^2+z_2^2+z_3^2+\left\|\tilde{\Theta}\right\|^2\right)+\frac{51}{4}\bar{\sigma}M^2+2\varepsilon_{21}+4\varepsilon_{11}+\frac{c_1+c_2}{\gamma^*}\left(2\varepsilon_{22}+4\varepsilon_{12}\right)$$

(C4)

Noticing from equation A1 that,

$$V\le\frac{1}{2}z_1^2+\frac{1}{2}z_2^2+\frac{1}{2}z_3^2+\frac{1}{2}\lambda_{\max}\left(\Gamma^{-1}\right)\left\|\tilde{\Theta}\right\|^2\le\frac{1}{2}\max\left(1,\lambda_{\max}\left(\Gamma^{-1}\right)\right)\left(z_1^2+z_2^2+z_3^2+\left\|\tilde{\Theta}\right\|^2\right)\quad\text{(C5)}$$

Hence, from equations C4 and C5

$$\dot{V} \le -c_0 V + d_0 \tag{C6}$$

where

$$c_0 = 2\frac{\min\left(c_1, c_2, c_3, \bar{\sigma}\frac{3}{4}\right)}{\max\left(1, \lambda_{\max}\left(\Gamma^{-1}\right)\right)},\ d_0 = \frac{51}{4}\bar{\sigma}M^2 + 2\varepsilon_{21} + 4\varepsilon_{11} + \frac{c_1 + c_2}{\gamma^*}\left(2\varepsilon_{22} + 4\varepsilon_{12}\right)$$

From equation C6

$$V \le V(0)e^{-c_0 t} + \frac{d_0}{c_0}\left(1 - e^{-c_0 t}\right) \le V(0)e^{-c_0 t} + \frac{d_0}{c_0}$$

From the above analysis $V(t)$ is shown to be uniformly bounded $\forall t \ge 0$, which also implies that $z_1, z_2, z_3, \tilde{\Theta}$ are bounded. Consequently, the system states and parameter estimate vector are also bounded $\forall t \ge 0$.

The functions utilized in the backstepping design:

$$sg_{i+1}(a) = \begin{cases} -1, & a < -\dfrac{1}{1+\mathrm{r}}\varepsilon_{2i} \\ \dfrac{1+r}{\varepsilon_{2i}}a & a \in \left[-\dfrac{1}{1+\mathrm{r}}\varepsilon_{2i}, \dfrac{1}{1+\mathrm{r}}\varepsilon_{2i}\right] \\ 1, & a > \dfrac{1}{1+\mathrm{r}}\varepsilon_{2i} \end{cases}$$

$$\sigma(a) = \begin{cases} 0, & a < 1 \\ a - 1, & a \in [1,2] \\ 1, & a > 2 \end{cases}$$

$$cf_{i+1}(a) = \sigma\left(\frac{a}{\varepsilon_{1i}}\right)$$

$$\sigma_\Theta(a) = \bar{\sigma}\sigma\left(\frac{a}{M}\right), \quad \bar{\sigma} = 1$$

APPENDIX D

Brief outline of the control scheme proposed by [58] applied to the vibration isolation system:

In the implementation of controller A the 3rd order system model given by equation 5.1 was reduced to a 2nd order system. This was accomplished by neglecting the dynamic terms in the actuator physics equation, namely, the inductance, L, and the back emf constant, k_v. Consequently, the base isolation system model is now of the form

$$m\ddot{z} + c\dot{z} + f_s(z,t) = \frac{2\gamma}{R}e_c - m\ddot{y} \tag{D1}$$

Defining the state variables $(x_1, x_2) = (z, \dot{z})$, equation D1 can be written in the form

$$\begin{aligned} \dot{x}_1 &= x_2 \\ \dot{x}_2 &= -\frac{c}{m}x_2 - \frac{f_s(z,t)}{m} - \ddot{y} + \frac{2\gamma}{mR}e_c \end{aligned} \tag{D2}$$

Utilizing equation 5.2 for the restoring force equation D2 can be written as

$$\begin{aligned} \dot{x}_1 &= x_2 \\ \dot{x}_2 &= \Phi(x_1, x_2, t)^T \Theta + R_e^*(x_1, t) + \ddot{y} + u(t) \end{aligned} \tag{D3}$$

where $\Phi(x_1, x_2, t)$, Θ and $R_e^*(x_1, t)$ are of the same form defined in section 5.2. Also, $u(t) = f_c(t)/m$, where $f_c(t) = \frac{2\gamma}{R}e_c$ is the control force with known values of γ and R.

The adaptive control scheme that is applicable to the above as proposed by [58] is given by

Adaptive control law:

$$u(t) = -\Phi(x_1, x_2, t)^T \hat{\Theta} - z_1 - c_2 z_2 - c_1 x_2 - sg(z_2)cf(|rz_2|)r + c_1\dot{y}_r + \ddot{y}_r \tag{D4}$$

Parameter estimate law:

$$\dot{\hat{\Theta}} = \Gamma \Phi(x_1, x_2, t) z_2 - \Gamma \sigma_{\Theta}\left(\left\|\hat{\Theta}\right\|\right)\hat{\Theta}$$
$$\hat{\Theta}(0) = \hat{\Theta}_0 \tag{D5}$$

The parameter definitions that complete the controller design scheme in the above expressions can be found in [58].